The Pennsylvania State University

The Graduate School

College of Earth and Mineral Sciences

SCALE INTERACTION AND MID-LATITUDE ATMOSPHERIC PREDICTABILITY:

IMPACTS OF MOIST CONVECTION AND GRAVITY WAVES

A Dissertation in

Meteorology and Atmospheric Sciences

by

Yongqiang Sun

Submitted in Partial Fulfillment

of the Requirements

for the Degree of

Doctor of Philosophy

December 2017

The dissertation of Yongqiang Sun was reviewed and approved* by the following:

Fuqing Zhang
Professor of Meteorology and Atmospheric Science
Dissertation Advisor
Chair of Committee

David J. Stensrud
Professor of Meteorology and Atmospheric Science
Head of the Department of Meteorology and Atmospheric Science

Sukyoung Lee
Professor of Meteorology and Atmospheric Science

Xiaofeng Liu
Assistant professor of Civil and Environment Engineering

Johannes Verlinde
Professor of Meteorology
Associate Head of the Department of Meteorology and Atmospheric Science

*Signatures are on file in the Graduate School

ABSTRACT

The small-scale processes (e.g., convective cells and gravity waves) that are often not fully resolved and represented by our forecast models, will affect processes at well-resolved scales and increase the uncertainties in our predictions. This thesis examines the scale interactions in predictability experiments using convection-permitting high-resolution ensembles of both global and regional scales, in order to study the intrinsic and practical predictability limit of in our numerical weather forecast.

The first part of this dissertation is aimed at testing Zhang, Snyder and Rotunno's three-stage error growth hypothesis focusing on the role of moist convection in the upscale error growth behavior. In the dry experiment free of moist convection, error growth is controlled primarily by baroclinic instability, hence forecast accuracy is inversely proportional to the amplitude of the baroclinically unstable initial condition error. Therefore, the accuracy of the prediction can be continuously improved without limit through reducing the initial error. On the contrary, in a moist environment with strong convective instability, rapid upscale growth arises from moist convection. As a result, the forecast error becomes increasingly less sensitive to the scale and amplitude of the initial perturbations. These diminishing returns from more accurate initial conditions may ultimately impose a finite-time barrier to the forecast accuracy. Moreover, the inclusion of strong moist convection changes the mesoscale (wavelength smaller than 500 km) kinetic energy spectrum slope from -3 to approximately $-5/3$ in our simulations, which is consistent with observations. Since the error spectrum will adjust toward the slope of the background flow, this change in slope of the background flow in our simulations due to moist convection further highlights the importance of moist convection to both the intrinsic and practical limits of atmospheric predictability, especially at meso- and convective scales.

Building upon the finding of the kinetic energy slope, in part two of this dissertation, it is further demonstrated that convective systems, triggered in a horizontally homogeneous environment, are able to generate a background mesoscale kinetic energy spectrum with a slope close to -5/3. To investigate the processes that are responsible for generating the -5/3 slope, spectral kinetic energy budget analysis is performed. The analyses show that the buoyancy production generated by moist convection, while mainly injecting energy in the upper troposphere at small scales, could also contribute to larger scales. The injected energy is then transported by energy fluxes (due to gravity waves and/or convection) both upward and downward. Nonlinear interactions, associated with the velocity advection term, finally helps build the approximate "-5/3" slope through upscale/downscale propagation of the energy at all levels.

The last part of the dissertation focuses on the influence of the upscale error growth to the operational forecast and the predictability gap between our operational forecast and the intrinsic prediction limit using the European Centre for Medium-Range Weather Forecasts (ECMWF) state-of-the-art ensemble. We find that from a global perspective, on average, the practical predictability limit of the mid-latitude weather by the current state-of- the-art global models from leading numerical weather prediction centers is about 10 days while the ultimate intrinsic limit is estimated to be less than 2 weeks. In other words, even with a perfect model, reducing the initial condition uncertainties to an order of magnitude smaller than the realistic current level of uncertainty will at most extend the deterministic forecast lead times by 3-4 days for mid-latitude day-to-day synoptic weather; much smaller room in improving the forecast lead times will be for smaller scale phenomena.

TABLE OF CONTENTS

LIST OF FIGURES

LIST OF TABLES

ACKNOWLEDGEMENTS

Good times pass by quickly and my five years here at Penn State was like flying to me. I owe my gratitude to a lot of people who have contributed to this dissertation and made it possible.

First and foremost, I am really fortunate to be able to work with my advisor Dr. Fuqing Zhang. Borrowing the concept from the "predictability world", working with Fuqing is like having perfect initial condition for a weather forecast, and Fuqing's passion for research and positive attitude provide the best model. Fuqing, your mentorship is paramount for me. Even now I could still remember our first meeting in your office that helped me quickly adapted after I came to US. Since then I get literally unlimited support from you whenever I need. Thank you!

Thank my committee members, Dr. David Stensrud, Dr. Sukyoung Lee, and Dr. Xiaofeng Liu. Dr. Lee is the "dynamics" person I go to and Dr. Stensrud knows predictability and all the model details. My meetings with Dr. Liu in China Dragon are cherishing memories. All of you show what a research scientist would be like. Your expertise and kindness are critical to me and this dissertation. I also want to thank my special mentor Dr. Richard Rotunno at NCAR. It has been a great pleasure to work with Dr. Rotunno. His generous idea and tremendous help made chapter 3 of this dissertation possible.

I owe my deep gratitude to people in my research group and the ADAPT center. I benefited greatly from discussions with Shuguang Wang, Junhong Wei, Dandan Tao, Yue Ying, Hans Chen, Masashi Minamide, Andrew, Lei Zhu, Scott Sieron, Robert, Jon Poterjoy, Chris Melhauser, Erin Munsell, Yudong Gao, Mingxin Li, Yunji Zhang, Yuanchun Zhang, Yonghui Weng and many others.

I am also very fortunate to be here in Department of Meteorology to finish my doctoral training. It was great pleasure to talk with all these excellent faculty members and graduate students. The administrative staff (especially Karen, Ginger, and Abby) really helped me throughout all these times.

I owe the most to my family: my wife Ke and my mom. You are the most important person in my life. Thank you for being there.

Chapter 1

Introduction

1.1 Space and time scales of atmospheric motions

The beauty of earth's atmosphere is that it possesses a large variety of different spatial and temporal scales. The horizontal length scales of the atmosphere can vary more than 10 orders of magnitude from the smallest Kolmogorov microscales (1 millimeter or smaller) to earth's circumference (~ 40000 km). The temporal scales of the atmosphere are often correlated with the spatial scales in the sense that phenomena having short time scales also tend to have small spatial scales, which is illustrated by the schematic shown in Fig. 1-1. As shown in Fig. 1-1, the horizontal scale of the atmosphere can be further divided into different categories based on dynamical distinctions between different scales.

On the large-scale end of the atmospheric spectrum, atmospheric motions with spatial scales larger than a few thousand kilometers are often referred to as the synoptic scale. The term "synoptic" originally comes from the synoptic chart used in middle 19th century, which could only resolve large-scale weather systems due to really coarse resolution of observational platform at that time. Typical examples of synoptic-scale processes are mid-latitudinal high and low pressure systems. These mid-latitude systems are mainly driven by baroclinic instability, which arises from the existence of a meridional temperature gradient and is most likely realized by disturbances with a wavelength of a few thousand kilometers. Due to the fact that synoptic-scale processes have a much larger horizontal scale than the vertical depth of the atmosphere (~10 km), these processes could be treated as quasi two-dimensional (Charney 1948).

The small-scale end of Fig. 1-1 is the micro-scale, where the horizontal scale is smaller than a few kilometers and the time scale is shorter than a few hours. Atmospheric motions at micro scales are fully turbulent and three-dimensional. Turbulent planetary boundary layer processes and strong small-scale convections like tornadoes happen at these scales. Micro-scales also contain viscous dissipation process that reduces the kinetic energy of the atmosphere.

The scale range between the synoptic scale and the microscale is the mesoscale, which includes phenomena like thunderstorms, hurricanes, gravity waves, etc. Compared to the convective- and baroclinic instabilities on the micro- and synoptic scales respectively, there is no dominant instability in the mesoscale, which means mesoscale flow could be affected by a variety of different processes depending on different local states of the atmosphere at different times.

1.2 Scale interaction processes

The challenge of understanding our atmosphere not only arise from the variety of dynamical scales and processes mentioned above. All of these processes with different scales furthermore interact with each other in a very non-linear way and exchange energy. Neglect and/or misrepresentation of some of the processes might lead to systematic biases of other processes we really care about. For each weather phenomenon of specific space and time scale, there are two possible routes for it to be affected by other systems with different scales. In the first route energy could come from larger scales, referred to as downscale energy propagation. In the second route energy might also propagate from smaller scale phenomenon, so called upscale energy propagation.

1.2.a Downscale energy propagation

The concept of downscale energy propagation can be illustrated by considering a simple flow system where an initial large-scale weak disturbance is imposed on a slowly varying mean flow (Vallis 2006). As the large-scale disturbance, composed with eddies and shear and such like, grows under the impact of the mean flow, there will be a secondary instability in the flow (e.g., shear instability) and a smaller eddy will develop. Initially, the smaller eddy may grow under linear instability such as the idealized Kelvin-Helmholtz instability. Once the smaller eddy reaches certain finite amplitude, the eddy itself may become unstable and foster an even smaller eddy, and so on. During this process, energy is transferred to smaller and smaller scales in a cascade-like process (Fig. 1-2). Finally, eddies are small enough so that they feel the effects of viscosity and are dissipated into heat.

Downscale energy propagation means that local small scale phenomena gets energy from larger scale and could be controlled the large-scale environment. Hence, we might be able to derive some information of the small-scale feathers if the large-scale environment is known. This provide advantages for us to make predictions of some local scale extreme events from coarse resolution global model under climate change scenario. This is also called downscaling process. As introduced on the National Center for Atmospheric Research (NCAR) website, "the two main approaches to downscaling climate information are dynamical and statistical. Dynamical downscaling requires running high-resolution climate models on a regional subdomain, using observational data or lower-resolution climate model output as boundary conditions. These models use physical principles to reproduce local climates, but are computationally intensive. Statistical downscaling is a two-step process consisting of i) the development of statistical relationships between local climate variables and large-scale predictors, and ii) the application of

such relationships to the output of global climate model experiments to simulate local climate characteristics in the future".

1.2.b Upscale energy propagation

While downscale energy propagation is important and sometimes dominant for local scale weather systems, upscale energy propagation also exists and plays a significant role. Assume we add a force to the atmosphere at small scales, eddies will first show up at this small scale. However, due to the nonlinear nature of the atmosphere, these small-scale eddies will interact with next larger scale and energize eddies at this larger scale. This larger scale eddies will then grow and interact with next larger scale. This is similar with that sketched in Fig. 1-2, except that the energy is inversely cascaded from small scale to large scale.

Examples for upscale energy propagation like self-organization of the convective cells is currently a hot topic of ongoing research. The upscale growth of the error energy also causes an intrinsic predictability to our atmosphere, which is our topic of the next section.

1.3 Intrinsic predictability arisen from upscale error growth

Current numerical weather forecast (NWP) is done by integrating the discretized primitive Navier–Stokes equation sets (numerical model) from the estimated initial conditions based on observations. Apart from the imperfect initial condition and the imperfect model that cause our prediction to fail, there exist an intrinsic predictability time in the chaotic atmosphere. The idea of intrinsic predictability, or the "butterfly effect", is first proposed by Lorenz (1969). It refers to the limit of prediction if the initial state is known nearly perfectly with a nearly perfect forecast model (Zhang et al. 2007). This intrinsic predictability arises from the inverse cascade

process explained above, since even the smallest amplitude small-scale error (butterfly flapping its wings) will propagate upscale and contaminate the whole system after a certain time, similar to the sketched upscale energy propagation process in Fig. 1-2.

Following the classical homogeneous turbulence approach, an estimate of the time needed for the small-scale error to contaminate the system can be derived as follows. Assume errors on a small scale will most contaminate the motion on the next larger scale in a time scale comparable to the eddy turnover time at that scale, defined by

$$T(k) \sim [v(k)k]^{-1} = [E(k)k^3]^{-1/2} \tag{1.1}$$

where k is the horizontal wavenumber, $v(k)$ is the velocity at this horizontal scale, and $E(k)$ is the background kinetic energy spectrum. In general, errors initially confined to a scale $2k$ will contaminate the scale k after time $T(k)$ in Eq. 1.1. Thus, the total time needed for errors to propagate from the small scale k_s to the large scale k_l is then estimated as

$$T \sim \int_{k_s}^{k_l} \frac{T(k)}{k} dk = \int_{k_s}^{k_l} \frac{[E(k)k^3]^{-1/2}}{k} dk \tag{1.2}$$

Assume the kinetic energy spectrum of the background flow satisfy the power law form $E \sim k^{-n}$, We have,

$$T \sim \begin{cases} ln\left(\frac{k_s}{k_l}\right), & n = 3 \\ \frac{2}{n-3}\left(k_s^{(n-3)/2} - k_l^{(n-3)/2}\right), & n \neq 3 \end{cases}$$

If we can reduce our initial error to smaller and smaller scales ($k_s \to \infty$), $T \to \infty$ for $n \geq 3$, which means the small-scale error will never contaminate the large scale. However, for $n < 3$, T remains finite no matter how we confine the initial error. This implies the existence of the intrinsic predictability.

The intimate relationship between the slope of the kinetic energy spectrum and upscale error propagation is verified by idealized study (Rotunno and Snyder 2008). In reality,

observational measurements indicate an energy spectrum varying as k^{-3}, or a -3 energy spectrum at synoptic scales with a transition to a $-5/3$ spectrum within the mesoscale (<500 km) (Nastrom and Gage 1985). Charney's theory of geostrophic turbulence (Charney 1971) is the generally accepted explanation of the synoptic-scale -3 spectrum. However, there is no general agreement on the mechanism(s) behind the mesoscale $-5/3$ spectrum. Given the strong implications of the -5/3 spectrum slope to the upscale error growth, possible factor(s) behind this spectrum is worth investigating.

Although the abovementioned concept of the intrinsic predictability has been proposed for decades and been widely accepted, it's not clear how these ideas apply in the real atmosphere. It is also questionable whether the homogeneous turbulence theory is valid to describe the physical processes behind the error growth behavior in the real atmosphere. In particular, several recent idealized and real-case numerical studies on atmospheric error growth indicate that moisture plays a critical role in the upscale process and errors grow much faster in the presence of convective instability and associated diabatic heating (e.g., Zhang et al. 2002, 2003; Tan et al. 2004). Using idealized high-resolution simulations, Zhang et al. (2007) first proposed the following three-stage model to illustrate the physical processes associated with the upscale error growth in moist baroclinic waves (Fig. 1-3). Initially, the errors grow from small-scale convective instability and then quickly [O (1 h)] saturate at the convective scales. In the second stage, the character of the errors changes from that of unbalanced convective-scale motions to one more closely related to balanced large-scale motions through geostrophic adjustment process. Balanced component of the errors is retained, while the unbalanced part is radiated away in the form of gravity waves. In the final stage, the large-scale (mostly balanced) components of the errors grow with the background baroclinic instability.

This three-stage conceptual model is demonstrated to be effective in explaining the atmospheric predictability of a real-case study by Selz and Craig (2015). In their high-resolution

simulation of a warm-season weather event over Europe, Selz and Craig (2015) showed that 60 h after perturbing their operational forecast model with negligible initial small-scale error, the large-scale 500-hPa geopotential height error induced by upscale error growth was about half the spread of the European Centre for Medium-Range Weather Forecasts (ECMWF) 6-h ensemble forecast.

1.4 motivation and thesis outline

We have introduced in this chapter the chaotic atmosphere, composed of phenomena of different scales interacting with each other. This strong nonlinear interaction, especially the upscale error propagation, leads to an intrinsic predictability time for the atmospheric. This idea is widely accepted, yet the physical processes in the atmosphere behind this upscale error growth are not well understood. While the three-stage model proposed by Zhang et al. (2007) is verified by some case studies, it is mostly conceptual and pays less attention on the practical (operational) side of the error growth processes. There also have been arguments on the application of this conceptual model. Recently, Durran and Gingrich (2014) argued that the initial relatively small large-scale error is more important than the upscale growth process of small-scale error proposed in Zhang et al. (2007). Hence, both the intrinsic and practical aspects of atmospheric predictability and the mechanisms behind that need to be investigated.

The arguably best way to address these issues is running realistic models that could resolves all these different scales, from convective instability at a few kilometers to baroclinic instability at thousands of kilometers and even larger. This is computationally intensive. Previous studies on error growth is limited to either regional model with convection-permitting resolution (e.g., Zhang et al. 2007; Selz and Craig 2015) or global simulations with coarse resolution not able to allow convection (Tribbia and Baumhefner 2004). With advances in computing capability,

the use of high-resolution convection-permitting models in near-hemispheric or even the global domain is becoming feasible in recent days (Mapes et al. 2008; Bretherton and Khairoutdinov 2015). This thesis plan to explore the technical advancement and use convection-permitting high-resolution ensembles of both global and reginal scales, in order to study the intrinsic and practical predictability limit of in our numerical weather forecast. Chapter 2 further verifies three-stage error growth hypothesis in Zhang et al (2007) under varying degrees of convective instabilities. Our results emphasize the role of moist convection in the upscale error growth behavior. Chapter 3 further investigates why moisture is important in the upscale growth of the error by examining how moist convection and the gravity waves help builds the shallower -5/3 spectrum. This chapter has mainly been conducted during the authors' visit at the National Center for Atmospheric Research (NCAR) which was supported by the Advanced Study Program (ASP). Chapter 4 of the dissertation focus on the influence of the upscale error growth to the operational forecast and the predictability gap between our operational forecast and the intrinsic prediction limit for mid-latitude weather systems. In the last chapter of the thesis, our summarized results and the implications are discussed. Future possible studies are also suggested based on our finding.

Chapter Figures
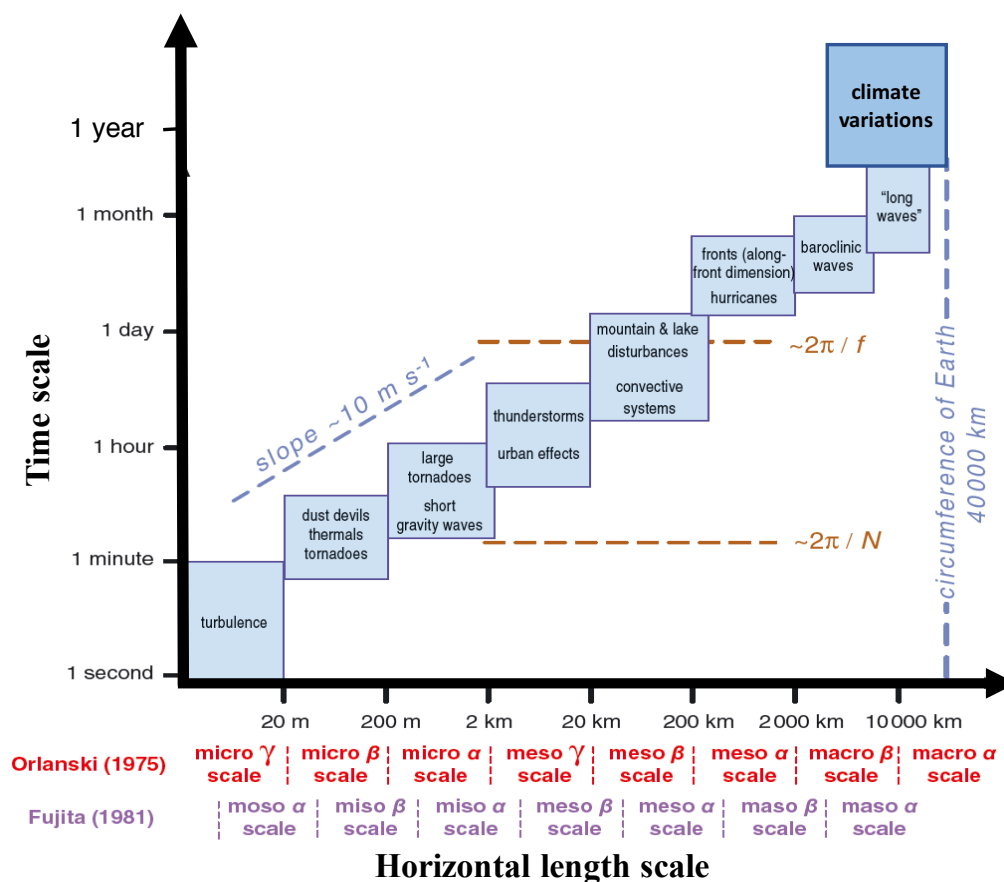
Figure **1-1**: Schematic of atmospheric processes classified according to their horizontal spatial- and temporal scales. Dashed lines indicate a constant characteristic velocity scale (10 m s^{-1}) and characteristic time scale imposed by the Coriolis parameter f and the Brunt-Väisälä frequency *N*: mid-latitudinal mesoscales motion ranges from the period of a pure buoyancy oscillation $2\pi/N$ (~ 10 mins) to inertial oscillations $2\pi/f$ (~ 17 h) [Adapted from Markowski and Richardson, 2010, p. 4].
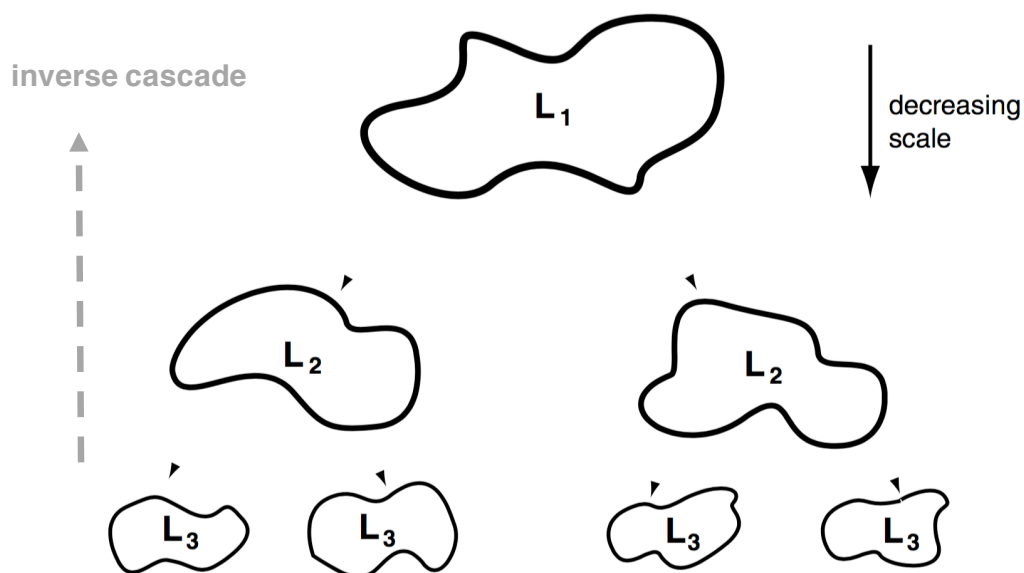
Figure **1-2**: Schematic of the energy cascade process. Energy is transferred to different scales during this process. The arrows indicate the directions of energy flow. In reality eddies are embedded within each other [adapted from Vallis, 2006, p.343].
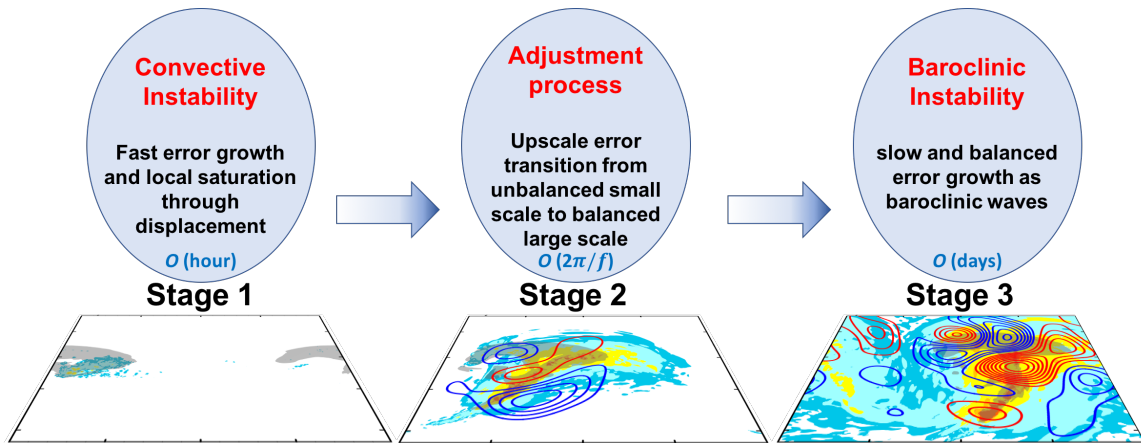
Figure **1-3**: Schematic of the three-stage conceptual error growth model proposed by Zhang et.al, (2007). The color shading in the lower panel is the difference total energy at 3h, 18h, 36h, respectively, while the grey shading shows the precipitation region in the moist baroclinic wave simulation. More details can be found in chapter 2.

Chapter 2

Intrinsic versus practical limits of atmospheric predictability

2.1 Introduction

Current-generation numerical weather prediction (NWP) models now are capable of routinely capturing the evolution of large-scale synoptic weather systems but remain challenged in forecasting meso- and convective-scale weather phenomena such as squall lines and tornadic thunderstorms. It is of great interest to assess the predictability of these mesoscale severe weather systems, what their predictability limits are and how to improve our forecasts, particularly with respect to the amount and spatial distribution of the associated precipitation (Zhang et al. 2007). There are two types of predictability problems (Lorenz 1996, Melhauser and Zhang 2012): (1) practical predictability refers to the limit on atmospheric prediction using current optimal analysis procedures to derive the initial state with the best available atmospheric forecast model (Lorenz 1982), and (2) intrinsic predictability refers to the limit of prediction if the initial state is known nearly perfectly with an nearly perfect forecast model (Lorenz 1969; Zhang et al. 2007; Rotunno and Snyder 2008).

Practical predictability is limited by realistic uncertainties in the forecast model and initial conditions. These uncertainties can include the adequacy of observations (e.g., accuracy, spatial and temporal coverage, and usability), data assimilation procedures, and deficiencies in the forecast models (e.g., Lorenz 1996, Melhauser and Zhang 2012). The intrinsic predictability emphasizes that there will be a finite intrinsic limit of predictability for the atmosphere (as in any chaotic dynamic systems) even if the initial condition and forecast model are nearly perfect (e.g., Lorenz 1969; Zhang et al. 2003, 2007). This intrinsic predictability is demonstrated by the rapid

"upscale growth" of the forecast error. For a flow with a slope shallower than -3, idealized model studies show that this flow has a faster eddy turnover time at smaller scales. Thus the growth rate of errors initially peaks at small scales and then, as the small-scale errors saturate, this peak shifts to larger scales with a smaller growth rate (Lorenz 1969; Rotunno and Snyder 2008). This type of "upscale growth" behavior is further demonstrated in Morss et al. (2009) with a quasi-geostrophic model. The error growth behavior could also vary largely at different times or in different regions of interest, which leads to a flow-dependent predictability skill (Morss et al. 2009; Bei and Zhang 2014). In addition, using the NCAR community climate model (version 3), Tribbia and Baumhefner (2004) confirms that upscale propagation of small-scale initial error is able to perturb the baroclinically unstable modes and results in the loss of predictability at global scales (refer also to Mapes et al. 2008).

Zhang et al. (2007) proposed a multi-stage conceptual model for atmospheric predictability through diagnosing error growth between "identical twin" convection-permitting simulations of idealized moist baroclinic waves: (1) the initial convective growth stage which begins with convective instability followed by rapid error saturation ($\sim O(1h)$), (2) the intermediate adjustment stage during which error projects to balanced field ($\sim O(2\pi/f)$), and (3) the large-scale growth stage where error grows with lager-scale baroclinic instability. This three-stage conceptual model is demonstrated to be effective in explaining the atmospheric predictability of a real-case study by Selz and Craig (2015a). In the high-resolution simulation of a warm-season weather event over Europe, Selz and Craig (2015a) showed that 60 h after perturbing their operational forecast model with negligible initial small-scale error, the large-scale 500-hpa geopotential height error induced by upscale error growth was about half the spread of the European Centre for Medium-Range Weather Forecasts (ECMWF) 6-h ensemble forecast. This result suggests that the upscale error growth plays a non-negligible role in limiting the operational forecast skill and need to be fully considered in numerical weather models. Rodwell et al. (2013) also related poor forecasts over

Europe to high convective activities over North America a couple of days ahead, indicating that large uncertainties introduced by convection will amplify in scale and amplitude during the propagation over the Atlantic. In addition to mid-latitude weather systems, the three-stage model is also found useful in explaining the predictability of tropical cyclones. In the study of four Indian Ocean cyclones, Taraphdar et al. (2014) found that the growth and saturation of error starts from small convective scales to intermediate mesoscale vortex or inertial gravity waves scales and ultimately influences the larger scale (TC system scale).

Recently, Durran and Gingrich (2014) argued that the initial large-scale error is more important than the upscale growth process of small-scale error proposed in Zhang et al. (2007). However, there are two concerns in the Durran and Gingrich (2014) study. First, their results are based on two winter storm cases during which convective instability is relatively weak. As atmospheric predictability is flow-dependent, the result may well be different under different baroclinic and convective instability as shown in Tan et al. (2004). Second, Durran and Gingrich (2014) did not explicitly examine the intrinsic predictability of the two weather events in their study since initial condition uncertainties in these two events, given by a particular initialization and data assimilation system of their model, are likely large in both in scale and amplitude (i.e., practical predictability of Lorenz 1982, 1996). The intrinsic predictability, on the other hand, refers to the limit of atmospheric predictability given infinitesimally small-scale, small-amplitude initial condition errors (Lorenz 1969; Zhang et al. 2007).

As an extension of Zhang et al. (2007), this study explores both the intrinsic and practical aspects of atmospheric predictability through convection-permitting simulations of idealized moist baroclinic jet-front systems with initial condition uncertainties at different scales and amplitudes. We will show that, for atmospheric predictability at the mesoscales, the role of moist convection and the upscale error growth starting from convective scales is critical for both the intrinsic and practical predictability. Section 2 introduces the model and method used in the

study. An overview of the simulated moist baroclinic systems is given in section 3. Section 4 explores the error evolution with initial perturbations of different scales. Their sensitivities to different amplitudes of initial perturbations are given in Section 5. The dynamics of the error growth are explored in more details in Section 6, with concluding remarks in Section 7.

2.2 Methodology

2.2.a Model configuration

The Advanced Research version of the Weather Research and Forecast model (WRF-ARW version 3.5.1, here after WRF; Skamarock et al. 2008) is employed in this study following the configurations of Wei and Zhang (2014). The flow is confined to a periodic channel on an f-plane ($f = 10^{-4}$), with a period of 4000 km in the zonal (x) direction and walls-separated 8000km in the meridional (y) direction. There are 100 vertical layers with a model top at 20 km, which means roughly 200 m grid spacing in the vertical (z) direction. The horizontal grid spacing is 10 km, which is on the very edge of convection-permitting resolutions and is likely to lead to some underestimation in the upscale error growth. With higher resolutions, the amplitude of the forecast error might change (Zhang et al. 2003, 2007). For example, Selz and Craig (2015b) found a factor of 3 amplitude differences in the 60-h DTE error between a 2.8-km and a 7-km "convection-permitting" simulation. Nevertheless, it is expected that a faster error growth with a higher resolution would follow similar physical processes (moist instability and convection) that may limit intrinsic predictability at the mesoscales and beyond.

The moist processes are parameterized using the Lin et al. (1983) microphysics scheme. Planetary boundary layer scheme of Hong and Pan (1996) is adopted here to handle the vertical diffusion in the simulation. The Monin-Obukhov similarity theory is used to parameterize the

surface layer flux of heat and moisture. We also apply the Rayleigh damping scheme described in Klemp et al. (2008) to the vertical velocity in the upper-most 5 km of the model domain to minimize artificial wave reflections from the model top. To simplify the interpretation of the results, no cumulus parameterization is used and no radiation is considered.

2.2.b Initial conditions for the baroclinic wave simulations

The initial jet profile is shown in Fig. 2-1. We use the same jet profile as that used in Zhang et al. (2007), which is derived through a simple 2D Potential Vorticity (PV) inversion (Davis and Emanuel 1991) method in the y-z plane. The prescribed PV distribution has constant value in both the troposphere [0.4 potential vorticity units (PVU, where 1 PVU = 10-6 K m2 s-1 kg-1)] and stratosphere (4.0 PVU). The value of 1.5 PVU is used to define the location of tropopause, indicated by the thick black line in Fig. 2-1. More details of the jet profile can be found in Zhang et al. (2007) and Zhang (2004). This jet profile is then expanded along the x direction homogeneously. It's worth noting that, when using this jet as the initial condition, it went through an adjustment process and caused an artificial oscillation in the simulation, likely due to the interpolation across strong gradients. To remove this unwanted oscillation, we first run this jet profile for 35 hours (around two times the inertial period) and then time-average all the variables, and run this time-averaged field again. This procedure is repeated several times until the amplitude of the oscillated horizontal wind is reduced to the order of 0.001 m/s.

The initial relative humidity profile is prescribed with slightly smaller values than that in Zhang et al. (2007) (see Appendix A). Figure 2-1 also shows the water vapor mixing ratio, which is very close to the observed values in the mid-latitudes. This moisture profile will be noted as MOIST from now on. To test the sensitivity of error growth to varying convective instabilities, two extra runs are also conducted, where the relative humidity is reduced to 50 percent of the

original value or the diabatic heating is turned off completely, referred as RH50 and DRY, respectively.

The fastest growing mode of the jet with small amplitude (0.1 K for θ) is used to initiate the baroclinic wave cycle. This mode is computed using a method similar to that employed in Plougonven and Snyder (2007): first, we introduce a Gaussian noise to the jet and integrate the model for three days; the perturbation field is then rescaled to that of a smaller amplitude which is added back to perturb the original jet again. This cycle is repeated 5 times for a total of 15-day simulation after which the normal mode of the perturbation fields is extracted to be the fastest growing mode.

2.2.c Initial perturbations (errors) of the "identical twin experiments"

Two types of perturbations are added to test the sensitivity of the short-range forecast error to initial error distribution. Type one error is Gaussian white noise used in Zhang et al. (2007). This random noise with zero mean and a standard deviation of 0.2 K was added to the potential temperature fields (hereafter denoted as NOISE perturbation). Type two error is simply the filtered fastest growing normal baroclinically unstable mode (amplitude 0.1 K for θ) in which only the long wavelength part (large scale, wavelength > 1000 km) is retained. Note all the prognostic variables are perturbed accordingly to minimize initial imbalance. We will use "LARGE" to represent this perturbation in the following sections.

Various experiments are conducted to test all kinds of sensitivities related to the initial perturbation distribution and amplitude. A full list of all the experiments is listed in Table 2-1.

2.3 Overview of the baroclinic wave simulations

Before presenting our results on how the errors grow, a brief overview of the simulated baroclinic wave system is given here. Under the initial jet profile described above, the development and life cycle of the baroclinic wave follow a cyclonic behavior similar to the "LC2" type defined in Thorncroft et al. (1993). Also note here, due to use of periodic boundary conditions in the zonal direction, the downstream development for both the baroclinic wave and error propagation could not be easily identified in the current study.

Figure 2-2 shows the simulated 500-hPa vertical vorticity of the baroclinic wave at day 5-8 under different moisture settings (that lead to different convective instability). A simple exponential amplification of the fastest growing baroclinic mode dominates the evolution before day 5 (96 hour). After day 8 (168 hour), barotropic processes become important and the decay of the baroclinic wave starts to prevail (Simmons and Hoskins 1978). Consistent with previous studies on the LC2-type life cycle of baroclinic waves, the forward-tilted and broadening troughs are very clear in all three experiments. During the period between day 5 and day 8, the large-scale vorticity structure is very similar in all the experiments, except that, in the moist runs, moist convection generates lots of local small-scale vorticity in the precipitation region. It is worth pointing that, moist convection not only adds small-scale structures to the vorticity field but also promotes faster and stronger development of the large-scale flow. For example, the baroclinic trough becomes deeper and more curved in the MOIST run than in the DRY run. This can be more quantitatively illustrated by the time series of eddy kinetic energy (EKE) plotted in Fig. 2-3a. The EKE is defined as (Waite and Snyder 2013):

$$\text{EKE} = \iiint \frac{1}{2}\rho(u'^2 + v'^2 + w'^2)dV \Big/ \iiint \rho dV \tag{2.1}$$

where $u', v',$ and w' are the perturbation fields after removing the zonal mean wind. Before day 5, the EKE of the DRY run and the MOIST run are very close. After the precipitation starts

to form, the EKE of the MOIST run begins to grow at a higher growth rate. At day 8, the EKE of the MOIST and the RH50 runs are 52% and 24% higher than that of the DRY run, respectively. To ensure this higher EKE is not solely due to increment of the small-scale wave activity, the large-scale filtered EKE (wavelength > 1000 km) is also shown. Again, the moist large-scale EKE is 51% higher than its counterpart in the dry run. Thus, it is very clear that EKE is dominated by its longer-wavelength baroclinic component. The meso- and small-scale components contribute less than 3% of the total EKE.

The precipitation rate of MOIST and RH50 is also shown in Fig. 2-3b. As we expected, precipitation in the MOIST run starts earlier and has larger value throughout the simulation than RH50, due to a stronger convective instability in MOIST.

2.4 Intrinsic predictability: forecast sensitivity to small-amplitude initial-condition errors

Considering the evolution of the baroclinic waves and the time when the precipitation starts, we choose to add the perturbations at 108 hour (12 hour after day 5) of the control baroclinic wave simulations described in the previous section. Two types of small-amplitude initial perturbations described in section 2 are added, the growth and evolution of which will be the focus of this section. As in Tan et al. (2004) and Zhang et al. (2007), the metric for examining the error is defined using the difference total energy (DTE):

$$DTE = \frac{1}{2}\sum[(\delta u)^2 + (\delta v)^2 + \kappa(\delta T)^2] \tag{2.2}$$

where δu, δv, and δT are the difference winds and temperature fields, $\kappa = C_p/T_r$, C_p is the specific heat capacity. T_r is the reference temperature of 270 K.

2.4.a Error growth from small-amplitude Gaussian white noises (NOISE)

Under the dry environment without convective instability, the initial perturbations grow solely through baroclinic instability. Since only a negligible part of the initial Gaussian white noise is projected onto the large-scale baroclinic mode, the overall growth in DTE from pure white noise is also weak in the DRY experiment. Instead, there is a noticeable decay of the initial error due to numerical model diffusion during the 36-h forecast period, as is shown in Fig. 2-4.

With the inclusion of moisture (and convective instability), however, the error growth behavior is drastically different (Fig. 2-4). Figure 2-5 shows filtered large-scale difference sea level pressure overlaid with the simulation precipitation in the unperturbed simulation. As is expected, the evolution of initial error generally follows the three-stage model proposed by Zhang et al. (2007). In the first few hours, the error mainly grows through convective instability and is confined to the precipitation region. At later times, the error starts to project to large-scale balanced field while the unbalanced components of the error energy propagate away from the area of moist convection in the form of gravity waves and/or density currents, a hint of which can be seen in Fig. 2-5 (e.g., 18h, on the edge of DTE field). The balanced components of the perturbations (error energy) eventually grow through large-scale baroclinic instability (see Zhang et al. 2007 for more details).

As for the vertical distribution of the error, Fig. 2-6 shows the contoured frequency by altitude diagram (CFAD, Yuter and Houze 1995) of the DTE in the MOIST_NOISE experiment. The largest DTE lies at 8-10 km, the same location where the strongest wind (jet stream) lies in the background flow. Note that within less than 1 h, some strong DTE already shows up at around 9 km, implying a rapid conversion (and growth) from the error potential energy (only potential temperature is perturbed) to the error kinetic energy.

2.4.b Error growth for small-amplitude perturbations at the scale of fastest growing mode (LARGE)

The same analysis (as for the NOISE perturbation described above) is conducted for the LARGE case (Fig.2-4, 2-7) that is perturbed with small-amplitude initial condition error at scales of the fastest baroclinic growing mode (wavelength > 1000 km). The evolution of DTE under dry environment follows an exponential growth with a growth rate similar to the growth of EKE in the control simulation. However, with the inclusion of moisture and convective instability, though initially the error growth at large scales shows some signature of the dry experiment (difference sea level pressure in Fig. 2-7), the total error growth is more similar to the MOIST_NOISE case consistent with the three-stage error growth conceptual model of Zhang et al. (2007) as also described above (Fig. 2-4, 2-7), which is in strong contrast to the DRY_LARGE experiment without moisture. Note the final large-scale forecast error at 36 h in MOIST_LARGE experiment is even smaller than that of the MOIST_NOISE case. This evidence further verifies that the upscale error growth from convective scale dominates over the baroclinic error growth in this experiment when the initial error amplitude is small, albeit large in scale.

It is worth noting that, the baroclinic growth of the error nearly stalls after 30 h in the DRY_LARGE experiment due to the decrease of the baroclinic instability of the background large-scale flow (not shown). However, in the MOIST_LARGE experiment, the forecast error rapidly increases (especially in the large scale) due to precipitation at that time (Fig. 2-7). The increase of domain integrated large scale DTE at later forecast time (after 30h) thus comes primarily through upscale propagation of error at smaller scales.

2.4.c Experiments with initial perturbations added at different times of the baroclinic life cycle

To further examine the robustness of the error growth characteristics discussed above, additional experiments are performed with initial perturbations added at different times of the baroclinic life cycle. In previous experiments, the initial perturbation is added at day 5 at 12 h (108 h) of the control simulations, we refer to these two experiments with different perturbations as N_H12 and L_H12, respectively. We have also run similar experiments six hours earlier/later at 06h / 18 h of day 5, which are noted here as N_H06, L_H06, N_H18, and L_H18, respectively. Thus, for each type of perturbation under the moist environment, we have 3 different perturbed runs. The list of all the experiments can also be found in Table 1.

Fig. 2-8 shows the evolution of the domain integrated DTE for all the three experiments for each type of perturbations. We can find that the DTE between short-range forecasts (e.g., at 12 h) is positively correlated to the precipitation rate. For example, the DTEs at 12h in the H12 experiments are noticeably larger than that of the H06 experiments due to stronger precipitation at later times (Fig. 2-3). After 20 h, the relationship between precipitation and the error growth is not as clear. Although the H12 and H18 experiments still have larger DTE compared to the H06 experiment, the difference between the H12 and H18 experiments becomes very small. Nevertheless, the error growth process in all the three experiments at different times is similar. We will thus focus on the H12 experiment for the analysis for MOIST_NOISE and MOIST_LARGE experiments if not stated otherwise.

Moreover, the error growth for both types of initial perturbations (MOIST_LARGE and MOIST_NOISE) is overall consistent with each other, all of which can be broadly described by the three-stage conceptual model of Zhang et al. (2007). In particular, the large-scale initial error in MOIST_LARGE acts primarily to perturb small scales in the region of moist convection, which makes little or no physical differences if the model is perturbed with the Gaussian white

noises (NOISE). Additional experiments where we kept the LARGE perturbations only in the vicinity of moist convection (a circle with a radius of 200 km centered at the initial precipitation center) are also conducted (i.e., the initial error scale is reduced by at least an order of magnitude), the simulated DTEs are again quantitatively similar to the MOIST_NOISE and MOIST_LARGE experiments (except for the large-scale component of the DTE, not shown here). This high insensitivity of the upscale error growth to amplitude and structure of the perturbations is also demonstrated by Hohenegger and Schär (2007). In essence, the error energy for larger scales for the MOIST_LARGE experiments are not necessarily cascaded downscale (as found in Durran and Gingrich 2014) but more likely grows from smaller scale errors conditioned by the large-scale differences at the region of convective instability.

To summarize, consistent with previous studies of Zhang et al. (2007) and Selz and Craig (2015a), the experiments discussed in this section further support the three-stage conceptual model of Zhang et al. (2007), and strongly suggest that atmospheric predictability in the mesoscale might be intrinsically limited due to chaotic dynamics of moist convection despite being perturbed only by small-amplitude (unobservable) initial perturbations regardless of the initial-error scales.

2.5 Intrinsic versus practical predictability: Sensitivity to initial error amplitude

Given that in the current-generation numerical weather prediction systems, the initial condition errors can be both considerably large in scale and amplitude (as in Durran and Gingrich 2014), this section examines the connections and differences between intrinsic and practical limits of atmospheric predictability through further exploring the error growth dynamics of the moist baroclinic jet-front systems with different initial-perturbation amplitudes (for both types of initial perturbations: LARGE and NOISE). These experiments are listed in table 1. More

specifically, the initial amplitude of the perturbations in experiments LARGE10 (LARGE100) is increased such that the initial domain integrated DTE is 10 (100) times larger than that of LARGE (for both DRY and MOIST scenarios). The initial amplitude of the perturbations in experiment MOIST_NOISE/10 on the other hand is reduced such that the initial domain integrated DTE is 1/10 that of MOIST_NOISE.

To help us better understand the error growth behavior at different scales, following Zhang et al. (2007) and with two-dimensional spectral decomposition, the domain-integrated DTEs for three characteristic horizontal wavelength ranges (S: smaller-scale, L < 200 km; M: intermediate-scale, 200 km < L < 1000 km; L: larger-scale L > 1000 km) will be examined.

Under the DRY environment, the forecast errors for LARGE type perturbations have a clear dependence on the amplitude of initial large-scale error that we added (Fig. 2-9). For example, the final domain integrated DTE of DRY_LARGE10 (DRY_LARGE100) at 36 h is approximately 10 (100) times larger than the final DTE of DRY_LARGE. Moreover, this quasi-linear relationship holds true not only for the total DTE but also for DTE at different scales (Fig. 2-9). This set of DRY sensitivity experiments with LARGE type initial perturbations demonstrates that error growth in dry baroclinic waves is primarily controlled by the exponentially growth of the baroclinic mode due to the background baroclinic instability.

Under moist condition, to elucidate of the limit of intrinsic predictability, we further reduce the initial domain integrated DTE of experiment MOIST_NOISE with the Gaussian white noise to one-tenth of its original value and mark this experiment as MOIST_NOISE/10. The forecast error in terms of DTE at 36 h for MOIST_NOISE/10 is almost the same as that of MOIST_NOISE, a strong indication of nonlinear error growth at the small scales. Further examination shows that, although starting at a smaller initial value, the small-scale error in the MOIST_NOISE/10 case grows much faster at the first few hours and catches up quickly with that in MOIST_NOISE. After the error at small scales saturated for both sets of experiments, the

upscale error growth is similar in both MOIST_NOISE and MOIST_NOISE/10. This is also consistent with Hohenegger and Schär (2007). The strong nonlinear error growth at the small scales, and the insensitivity to the initial error amplitude in these MOIST experiments further demonstrates that atmospheric predictability can be intrinsically limited under the influence of moist convection, *which means that our forecast accuracy will be limited no matter how small the initial error amplitude is.*

Nevertheless, given that the initial condition errors in the weather prediction models at present are certainly not infinitesimally small either in scale and amplitude (as discussed in Durran and Gingrich 2014), our attention is now turned to the limit of practical predictability through changing the (large-scale) initial perturbation amplitude in the MOIST_LARGE experiments. If we increase the initial DTE by a factor of 10 (MOIST_LARGE10), the final DTE at 36 h is only slightly larger (~ 1.5 times) than in the MOIST_LARGE experiment. The final DTE of MOIST_LARGE10 is also very close to that of the NOISE experiment, including a close match for all of the three characteristic scale ranges (L, M, and S scales, Fig. 2-9). A further examination of the DTE evolution at the three characteristic scale ranges for MOIST_LARGE10 shows that, at the earlier simulation times before 20 h, the large-scale error generally follows the baroclinic growth in the DRY_LARGE case, while the small-scale error growth is similar to that of the MOIST_NOISE case. At later times, when the large-scale baroclinic growth slows down considerably (Fig. 2-9b, whereas the error begins to saturated at smaller scales), the error growth at the larger scales begins to come primarily from the upscale propagation of intermediate- and small-scale errors.

For the MOIST_LARGE100 experiment where the initial DTE is increased to 100 times that of MOIST_LARGE (with the maximum difference wind speed being around 2 m/s, comparable with the ensemble spread of current operational model), the error growth at the large scales now is similar to the DRY_LARGE100 experiment, although at later times (after 20 hour) the large-

scale error in MOIST_LARGE100 is slightly larger than that of DRY_LARGE100 likely due to upscale error growth from smaller scales in the MOIST_LARGE100 experiment. The total DTE at 36 h in MOIST_LARGE100 is more than twice higher than that of DRY_LARGE100, primarily due to a much more energetic small and intermediate scale error under the influence of moist convection. The error growth in the MOIST_LARGE100 experiment evolves more like that in Durran and Gingrich (2014), in the sense that the short-range large-scale error growth is hardly affected by the upscale growth of smaller scale errors. In other words, if the initial condition error is large in scale and considerably large in amplitude, as in the case of practical predictability, the considerably large-amplitude initial condition error at the large scales is likely to be the most influential to the forecast quality. In this case, we can improve our forecast results through reducing the initial condition error at the large scales, consistent with the findings of the recent study of Durran and Gingrich (2014), as well as Zhang et al. (2002), Bei and Zhang (2007), and many other authors.

However, even though Durran and Gingrich (2014) did not explore explicitly the growth of smaller-scale small-amplitude error as in the case of intrinsic predictability, they argued that the "butterfly effect" (nonlinear upscale error growth from small scales) could be easily overwhelmed by the growth from a relatively small-amplitude large-scale initial error. Their conclusion is not supported by our sensitivity experiments presented above. As in both of the MOIST_LARGE and MOIST_NOISE experiments (as well as MOIST_NOISE/10), regardless of the scales of the initial-condition error, if the amplitude of the initial perturbations is small, the short-range forecast is dominated by the upscale error growth from the small scales (the so-called butterfly effect), not necessarily cascading from large scale initial condition error.

Moreover, the drastic difference of the error growth and the final DTE amplitude between our DRY and MOIST experiments further illustrates the fundamental role of moist convection in limiting the intrinsic predictability. Sensitivity of the error growth to initial perturbations at

different stages of the moist baroclinic life cycle also suggests that the stronger the convective instability, the faster error saturation at the smaller scales, and the more rapid upscale transfer of error to larger scales, as is shown in Seiz and Craig (2015a). The sensitivity of error growth to the degree of convective instability can be further verified through the RH50 experiments perturbed with initial error of both LARGE and NOISE (Fig. 2-10), in which the background relative humidity of the initial baroclinic wave is reduced to 50% of the control moist experiment. Not surprisingly, with reduced moisture and convective instability, convection and precipitation in RH50 are much delayed and weaker. Consequently, the forecast error in these RH50 experiments is much smaller than that in the corresponding MOIST experiments.

2.6 Error growth dynamics across different scales

In the previous two sections, we have shown the distinction between intrinsic and practical predictability. We have also demonstrated that the upscale error growth from small scales under the influence of moist convection may critically limit the intrinsic predictability of the atmosphere at all scales. However, it remains uncertain whether the upscale error growth is still relevant under the practical predictability scenario where the initial error at the large scales is considerably large. We will investigate in more detail these questions in this section through diagnosing error growth and transfer across scales.

Figure 2-11 shows the evolution of power spectra for the domain integrated difference total energy (DTE), which gives us a better sense of how the error grows at different scales. The spectral energy density of the full model state (24h-36h after perturbation) in control experiments is also plotted and multiplied by a factor of 2 (which does not change the slope), so that it represents the saturation level for the DTE. It is interesting to note that with the inclusion of moisture, the slope for the full model state transited from a steep -3 to a shallower close to -5/3

power law at a wavelength around 400 km. This transition is indeed consistent with the observational study of Nastrom and Gate (1985). As for the growth of the DTE, a clear cascading process could be found under the DRY environment and the power spectra of the DTE grow at nearly the same rate at all scales. The DTE does not saturate until very late in the DRY_LARGE100 experiment. However, under the MOIST environment, the DTE at small scales quickly saturate after the perturbation is added regardless of the initial amplitude of the perturbation (refer to MOIST_LARGE, MOIST_LARGE100).

For the practical predictability scenario with considerably large initial condition error at the large scale (MOIST_LARGE100), the upscale growth of error from smaller scales becomes less evident. Similar to the real-data case of Durran and Gingrich (2014), the error shows a more uniformed growth over all the scales (especially for larger scales, see Fig. 2-11d). This is also similar to the DRY_LARGE100 experiment (Fig. 2-11b), except that in the MOIST_LARGE100 case, the spectral slope of for small-scale error with a wavelength smaller than 400 km flattens to approximately -5/3 rather than -3. To further examine if the upscale growth plays a role in the change of the error spectral slope, a budget analysis for DKE at the three characteristic scale ranges (L, M and S) is performed. The equation for DKE budget at large scale can be written as:

$$\frac{\partial}{\partial t}(DKE)_L = \left[-\bar{\rho}(\delta u)_L \delta\left(\boldsymbol{u}\cdot\boldsymbol{\nabla_h}u + w\frac{\partial u}{\partial z}\right)_L - \bar{\rho}(\delta v)_L \delta\left(\boldsymbol{u}\cdot\boldsymbol{\nabla_h}v + w\frac{\partial v}{\partial z}\right)_L\right]$$

$$+ \left[-\bar{\rho}(\delta u)_L \delta\left(\frac{1}{\rho}\frac{\partial p'}{\partial x}\right)_L - \bar{\rho}(\delta v)_L \delta\left(\frac{1}{\rho}\frac{\partial p'}{\partial y}\right)_L\right] + (Damping)_L \qquad (2.3)$$

where $(DKE)_L = \frac{1}{2}\bar{\rho}\left[(\delta u)_L^2 + (\delta v)_L^2\right]$. The derivation for this equation can be found at Appendix B). For intermediate and small scales, the equations are essentially the same except that the subscripts of the terms are changed to M or S. The two terms in the first bracket on the right-hand side of this equation is the nonlinear advection term (referred as ADV), which is responsible

for the redistribution of the error across different scales. The terms in the second bracket is the pressure term, which mainly represents the conversion between difference potential energy and difference kinetic energy (See Appendix C).

The results of the DKE budget analysis for three different scales are given in Fig. 2-12. Under the dry environment, there is a clear downscale error transfer for DRY_LARGE100 (upper-most panel of Fig. 2-12), where the peak of large-scale error growth shows first, followed then by the peak of the medium scale, the peak of small-scale error growth comes last. Also worth pointing out that, for this downscale error transfer, the ADV term leads the pressure term and dominates the error growth for the medium and the small scales, consistent with the hypothesis that error first propagates to smaller scales through the nonlinear advection term.

The MOIST_NOISE and MOIST_LARGE experiments, on the other hand, demonstrate an apparent upscale error growth picture as seen from the budget analysis. The error growth first starts at the small scales, and then gradually expands to the medium and the large scales. The pressure term and the ADV term contribute equally at all the scales. The ADV term is actually enhanced by the pressure term (through the buoyancy flux). If we turn off the latent heating, not only the pressure term but also the ADV terms will immediately drop to near zero.

For the MOIST_LARGE100 experiment, both the downscale and upscale error growth processes are present. At the large scale, the error grows similarly to the corresponding dry experiment in the first 20 hours, while at the small scale, the upscale growth is apparent, with the pressure term and ADV term contributing equally to the growth. For the intermediate scale in this case, due to the influence of downscale propagation of the large-scale initial error, the ADV term plays a slightly bigger role than the pressure term. Nonetheless, the pressure term is also very important for the intermediate scale error growth, especially at later simulation times when the background baroclinic growth is weakened. The upscale propagation effect can be convincingly demonstrated through the error growth budget for the large scale after 20 h: the growth of DKE

for the large scale in the MOIST_lARGE100 case continues while the growth at the large scale diminishes in the corresponding DRY_LARGE100 experiment due to weakening of the background baroclinic growth.

Moreover, with the energy spectra flattened to a slope close to -5/3 in the moist environment, the mesoscale energy spectra (wavelength < 400 km) increase dramatically in the MOIST case, the forecast short-range error (36 h) for intermediate and small scales in the MOIST_LARGE experiment is more than three times larger than that in the corresponding DRY_LARGE100 experiment (Fig. 2-9). Thus the dominant error source for the mesoscale is due to convection. Failure to predict the location and/or the strength of the convection characters would likely lead to a more inaccurate mesoscale forecast. Hence the weak sensitivity of the convective cells to initial perturbation and the upscale growth not only leads to less intrinsically predictability but likely also plays a substantial role in limiting the practical predictability at mesoscale. To further verify this, the power spectrum of the latent heating forcing difference, which shows the scale of moist forcing (buoyance production), is plotted in Fig. 2-13 for both the MOIST_NOISE and the MOIST_LARGE100 experiments. This forcing at different scales can be defined as in Equation 7 of Waite and Snyder (2013)

$$F(\boldsymbol{k}) = \frac{1}{2} \delta\left(\hat{\theta}^*(\boldsymbol{k})\right) \delta\left(\hat{H}(\boldsymbol{k})\right) + c.c. \qquad (2.4)$$

Where H is the potential temperature tendency due to moist physics and c.c denotes complex conjugate. A 12-h time-average is used in Fig. 2-13, where the semi-log axis is considered to preserve the area. The latent heating forcing shows no significant difference between the MOIST_NOISE and the MOIST_LARGE100 experiments. At first, this forcing acts mainly on the small scales (wavelength ~ 100 km). Later, it expands to larger scales, with the peak spectral power of the forcing remaining at the meso- and smaller scales. The similarity of these two experiments further suggests that experiment MOIST_LARGE100 (under the practical

predictability scenario) does not bring more (additional) forcing through buoyancy production than MOIST_NOISE (under the intrinsic predictability scenario). In other words, the primary role of the initial large-scale perturbation in this MOIST_LARGE100 experiment is through direct projection of the initial difference to trigger the error growth, saturation and upscale transfer of small-scale moist convection that is similar to the MOIST_NOISE experiment, not necessarily through the downscale error cascade from the initial large-scale perturbation.

2.7 Concluding remarks

Through a series of "identical twin experiments" with Weather Research and Forecast (WRF) model by adding initial condition errors of different scales and amplitudes, this study explores the limits of both intrinsic and practical predictability and the multi-scale error growth dynamics of the baroclinic jet-front systems with varying degree of convective instabilities.

In the dry experiments free of moist convection (and the "fakedry" experiments that suppress convection through turnoff of diabatic heating), only the baroclinic growth of the large-scale perturbation can be found in the 36-h short-range forecast. The forecast error under the dry environment has a quasi-linear dependence on the amplitude of the initial large-scale perturbation. This suggests that the forecast accuracy can be continuously improved through reducing the initial condition and thus predictability for the dry baroclinic waves can be continuously improved without an apparent limit at the synoptic time scales if the forecast model and the initial conditions are nearly perfect (though other sources of smaller scale instabilities such as boundary layer turbulence and shear instability that are not studied here may also trigger upscale error growth that may eventually limit the intrinsic predictability).

The limits of both intrinsic and practical predictability are found to be drastically different under the moist environment with strong convective instability. The rapid upscale error growth

from moist convection will lead to the forecast error being increasingly less sensitive to the scale and amplitude of the initial perturbations when the initial error amplitude is sufficiently small, as characterized in the multi-stage error growth conceptual model of Zhang et al. (2007). Due to the strong nonlinear upscale error growth from moist convection, there will be diminishing returns (increasing smaller improvements) in the forecast accuracy through further reducing the initial condition error, a key indicator of limit of intrinsic predictability (Lorenz 1969; Rotunno and Snyder 2008; Palmer et al. 2014). In other words, the distance between the practical and intrinsic predictability limits become smaller and smaller as the initial condition accuracy continues to improve. On the other hand, when the initial perturbations are sufficiently large in scale and amplitude, as for most current-day operational models, the baroclinic growth of large-scale finite-amplitude initial error will play a more dominant role in the forecast accuracy at all scales for both dry and moist baroclinc waves. The forecast accuracy can be further improved (and thus the limit of practical predictability can be extended) through reduction of initial condition errors, especially those at larger scales. Even in this case, the upscale error growth from convective instability under the moist environment could still be crucial for predictability of mesoscale processes. In addition, as is pointed out in Rodwell et al. (2013), the upscale error growth might also become relevant for larger scales at longer forecast lead times, although its importance may be flow dependent. Furthermore, an insufficiently simulated upscale error growth may well be one of the reasons for the underdispersion issue in nowadays ensemble predictions. All of these studies imply the practical importance of the butterfly effect --- the rapid upscale error growth from moist convection that has an intrinsic predictability limit.

It is also worth noting here that, if we consider the life cycle of the baroclinic wave, the results showed above will have dependence on the development stage of the baroclinic system. For example, to focus on the convective instability, the forecast experiments in this paper start from day 5 when the baroclinic system has been already in a mature stage and tended to cease an

exponential growth as shown in Fig. 2-2. Hence, the period during which the baroclinic wave grows exponentially is quite short of $O(1)$ day (Fig. 2-3), as evident in the error growth shown in Fig. 2-9, which indicates that the large-scale error ceases the exponential growth after about one day for the DRY_LARGE experiment. As shown in Zhu and Thorpe (2006), the large-scale error usually sustains exponential growth during a period of at least 77 hours when the basic state is specified by an initial developing stage of the baroclinic system. Hence, we might underestimate the error growth of large-scale motions associated with the inherent baroclinic instability in the current study. The underestimation might be related to the result on the relative importance of convective instability and the subsequent upscale error growth. Similar caveat is also noted in Palmer et al. (2014) by conducting forecasts experiments based on the surface quasi-geostrophic equation from different initial conditions. They remarked on the intermittent characteristic of the butterfly effect and the flow-dependent nature of the large-scale forecast sensitivity to small-scale initial error. Thus, the crucial role of convective instability in the large-scale error growth discussed in the current study might also depend strongly on the prescribed initial flow conditions.

The connection and difference between practical and intrinsic predictability was also succinctly illustrated in the schematic diagram of Fig. 18 in Melhauser and Zhang (2012), which is abstracted from the mesoscale predictability study of a strong warm-season bow echo and squall line event. We believe this conceptual diagram can be generalized to the current study of idealized moist baroclinic waves, as well as to our studies of winter snowstorms (Zhang et al. 2002, 2003), spring-time tornadic thunderstorms (Zhang et al. 2015, 2016), warm-season flooding (Zhang et al. 2006; Bei and Zhang 2007) as well as hurricanes and tropical cyclones (Zhang and Sippel 2009; Zhang and Tao 2013; Tao and Zhang 2014, 2015).

The predictability behavior is closely linked to the flow's kinetic energy spectrum. As mentioned in the introduction, previous studies have already shown the existence of a

predictability limit with a shallower than -3 slope (Rotunno and Snyder 2008). Under the moist environment with the inclusion of strong moist instability, the slope of the background kinetic energy spectrum decreases from -3 to -5/3. This transition of the spectral slope emphasizes the importance of convection to both the intrinsic and practical limit of mesoscale predictability within the moist baroclinic jet-fronts systems. However, the exact reason(s) for this transition is beyond the scope of the current study. This change may be due to the strong turbulent motions that are induced by moist convection that becomes more homogeneous and isotropic, and/or much stronger gravity waves induced by convection (as shown in Wei and Zhang 2014). Past theoretical studies suggest that both three-dimensional turbulent motion and the linear gravity waves could have a slope of -5/3 (e.g., Vallis 2006). However, neither of these two hypotheses is ready to explain the transition scale at a horizontal wavelength around 500 km, which is found in our simulations as well as in observational studies (e.g., Nastrom and Gage 1985). Recently, Callies et al. (2014) utilized a modified Helmholtz decomposition method to process the observation data by the flight through which they claimed that the small-scale fluctuations are dominated by gravity wave activity. If this is the case, since linear inertia gravity waves do not propagate error upscale in the same way as the vortical turbulent flows discussed by Lorenz (1969), the forecast times of weather systems could potentially be extended considerably. We plan to conduct further research on this topic. Nonetheless, the change of the kinetic energy spectrum slope is clearly due to moist convection and emphasizes the importance of convection on the limit of mesoscale predictability.

Chapter Figures and Tables
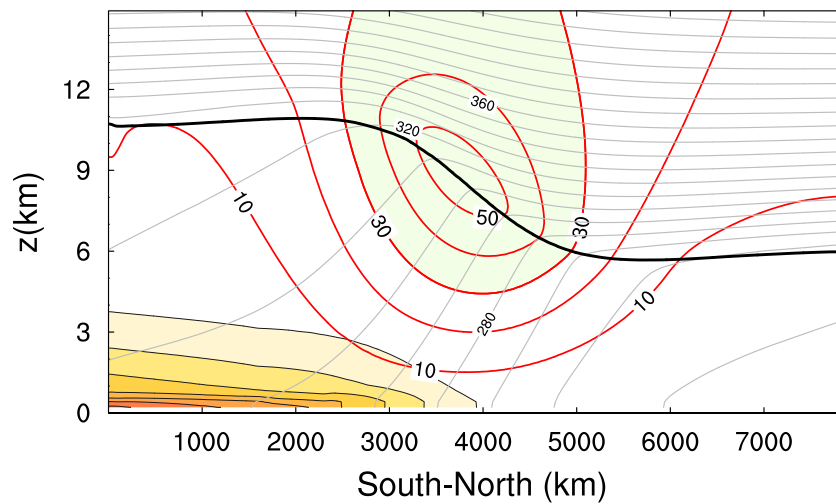
Figure **2-1.** Vertical cross section of the initial jet for zonal wind (red, every 10 m s^{-1}, >30 m s^{-1} light green shaded), potential temperature (grey, every 5 K), the tropopause denoted by dark line where the potential vorticity equals 1.5 PVU, and initial water vapor mixing ratio (shaded every 2 g kg^{-1}).
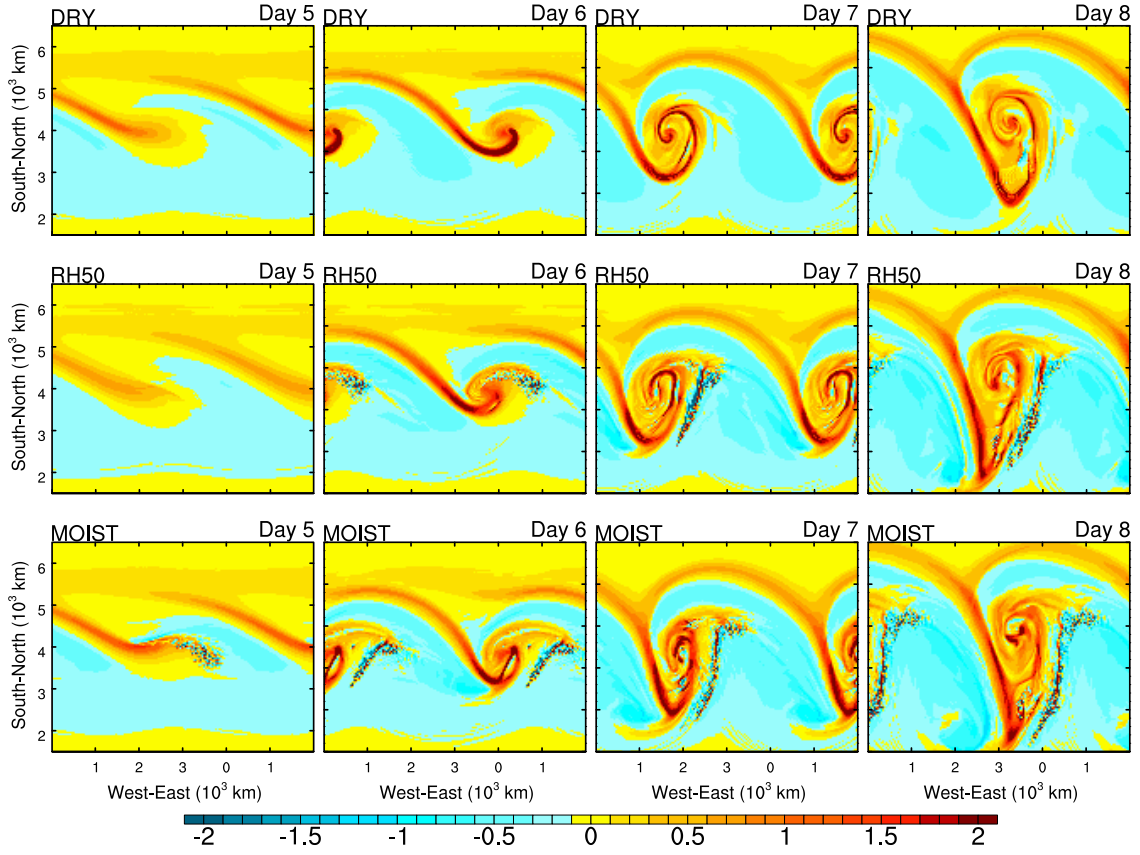
Figure 2-2. Horizontal snapshots of the 500-hPa relative vorticity (10^{-4} s^{-1}) from day 5 to 8 for the control experiments of DRY, RH50 and MOIST, respectively. The distance between the tick marks in the axes is 1000 km. Regions within 1500 km of the southern and northern boundaries of the model domain are omitted.
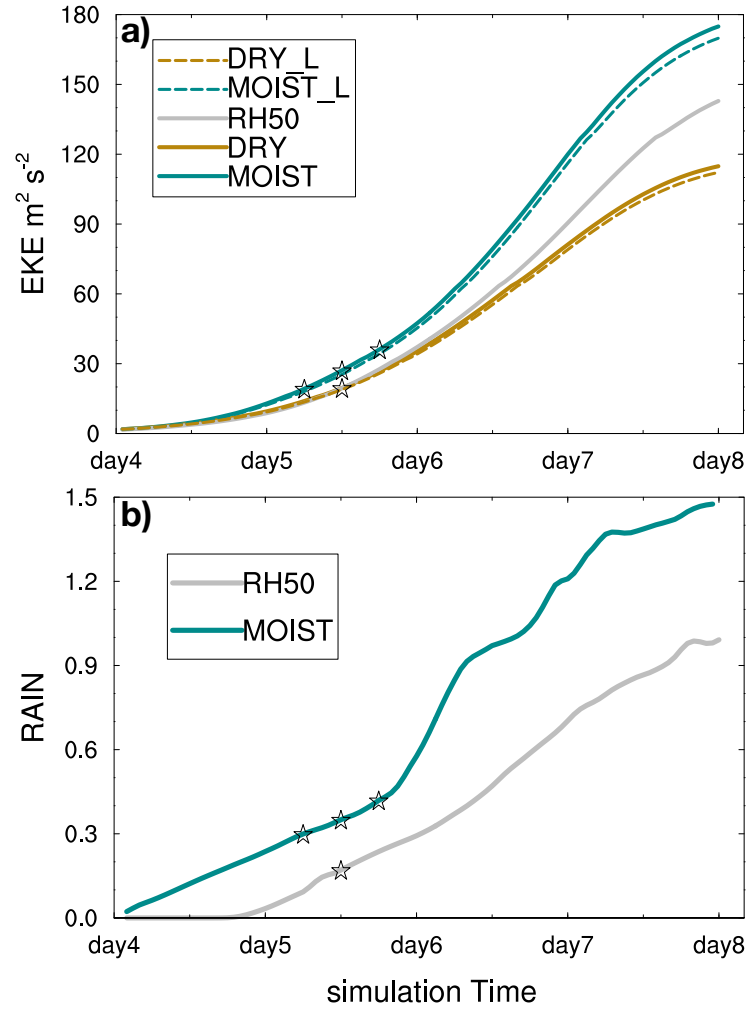
Figure **2-3.** **a)** Time series of the simulated eddy kinetic energy per unit mass from different experiments. Dash line shows the long-wave end of the eddy kinetic energy (wavelength > 1000 km). **b)** Time series of the domain-averaged precipitation rate (mm every 12 h, averaged over 3-h intervals). The stars in both plots imply the time when the initial perturbations are added.
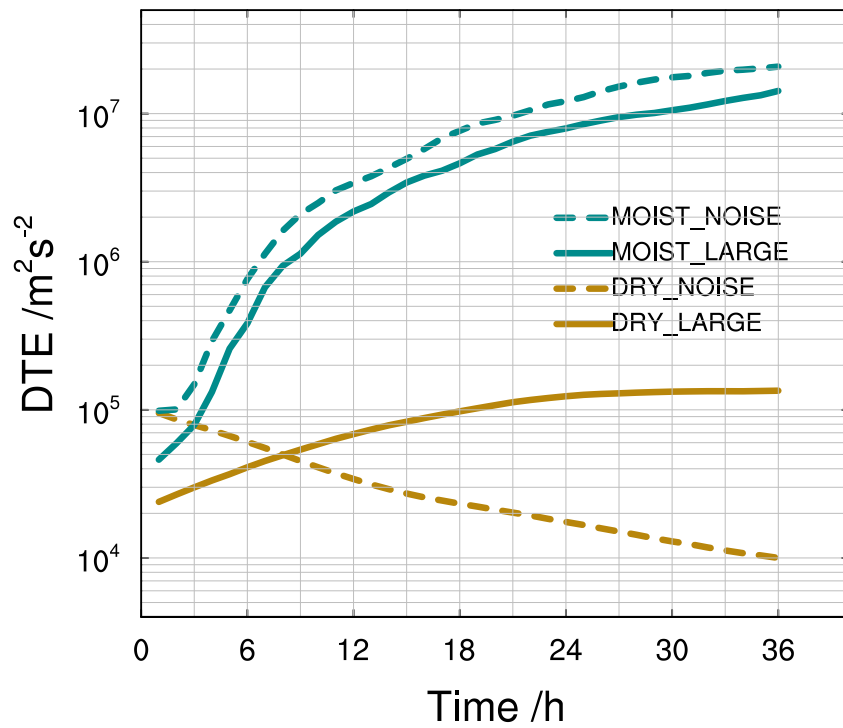
Figure **2-4.** Time series of the domain integrated difference total energy (DTE) for the NOISE (dashed) and LARGE (solid) experiments under DRY (gold) and MOIST (cyan) environment, respectively.
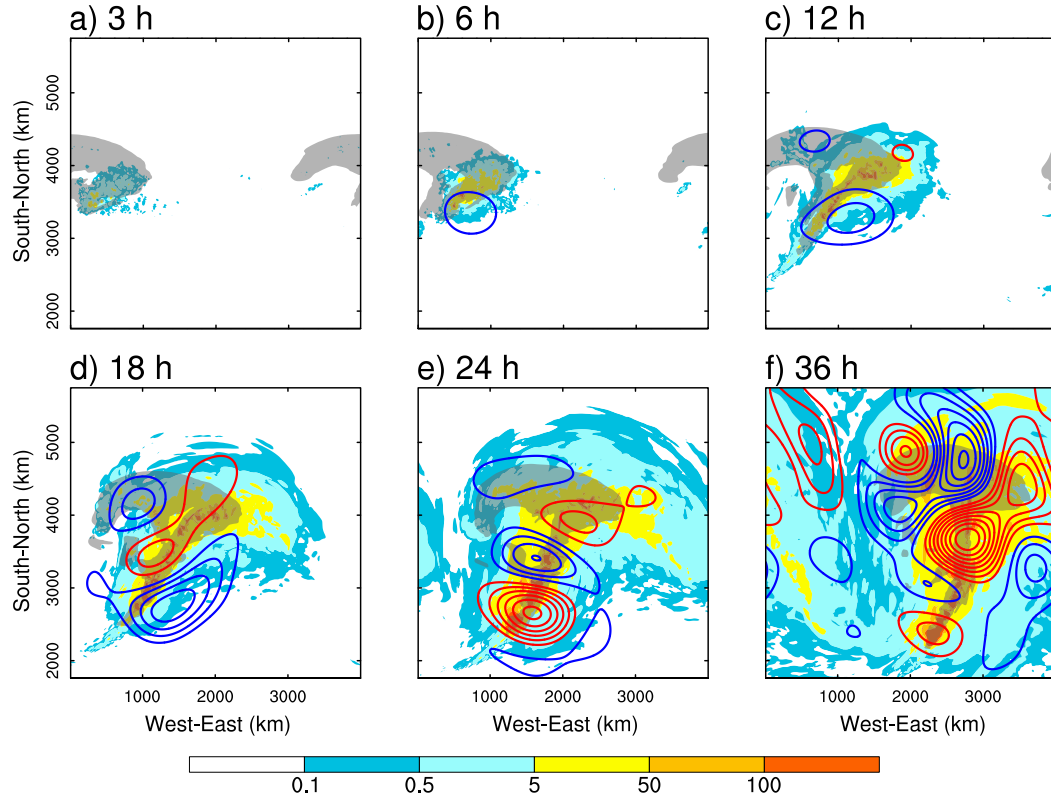
Figure 2-5. Snapshots of column maxima of DTE (m^2 s^{-2}) for the MOIST_NOISE experiment valid at 3, 6, 12, 18, 24, and 36 h after the initial perturbations are added. The contours show the long-wave filtered sea-level pressure difference (wavelength > 1000 km, every 5 Pa, red contour implies positive values, whereas blue contour means negative). Grey shaded regions indicate where the precipitation rate is larger than 0.1 mm per hour.
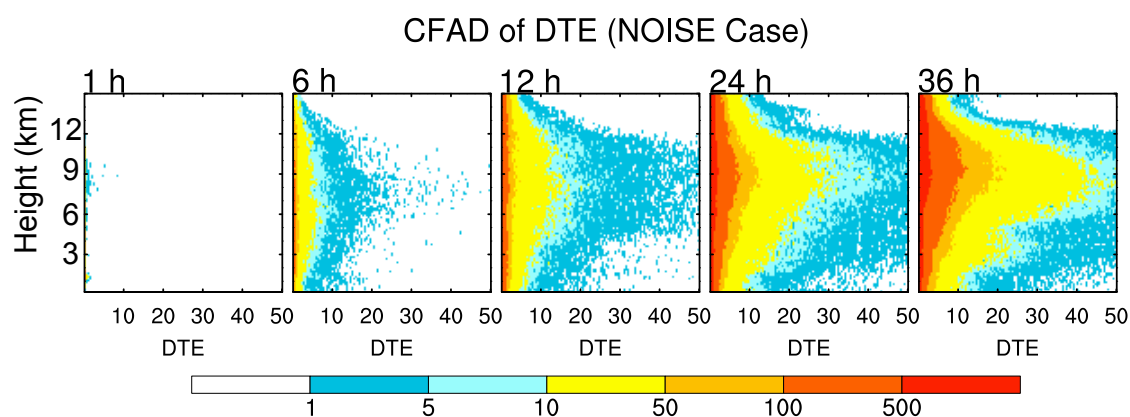
Figure 2-6. Vertical distribution of DTE for the MOIST_NOISE experiment, shaded parts show the frequency (number of points) of DTE at a particular height.
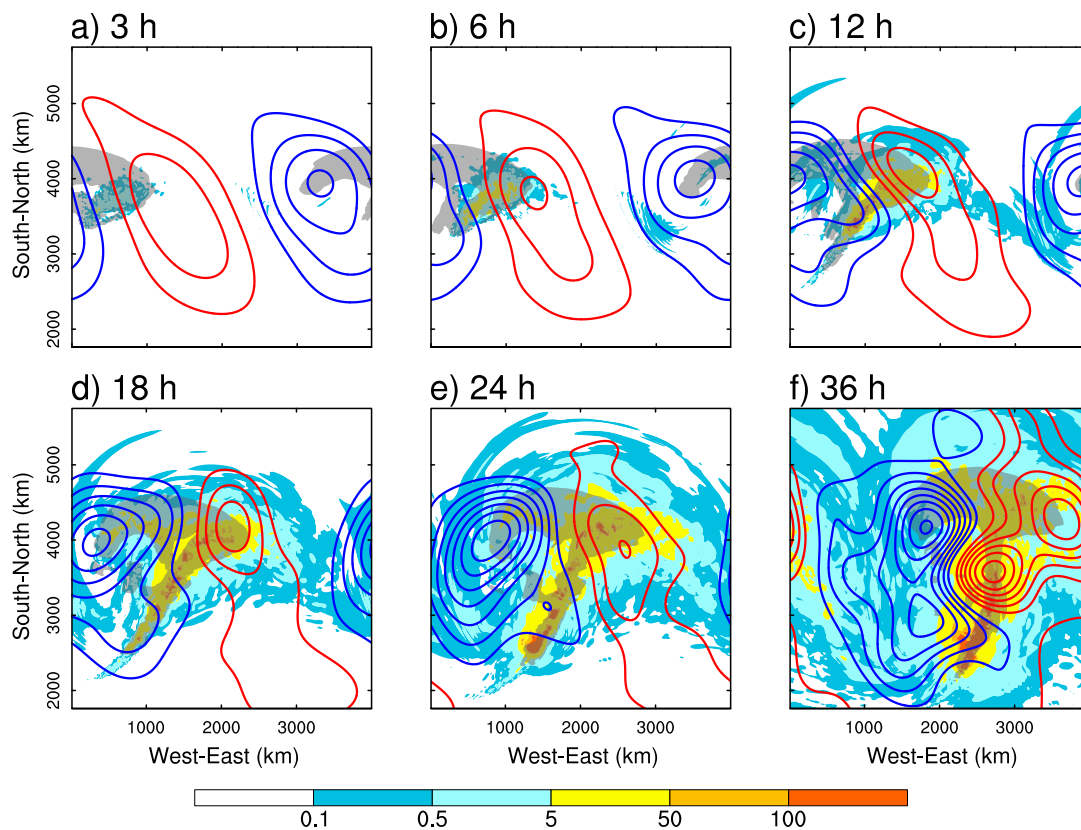
Figure **2-7.** Same as Figure 2-5, but for the MOIST_LARGE experiment.
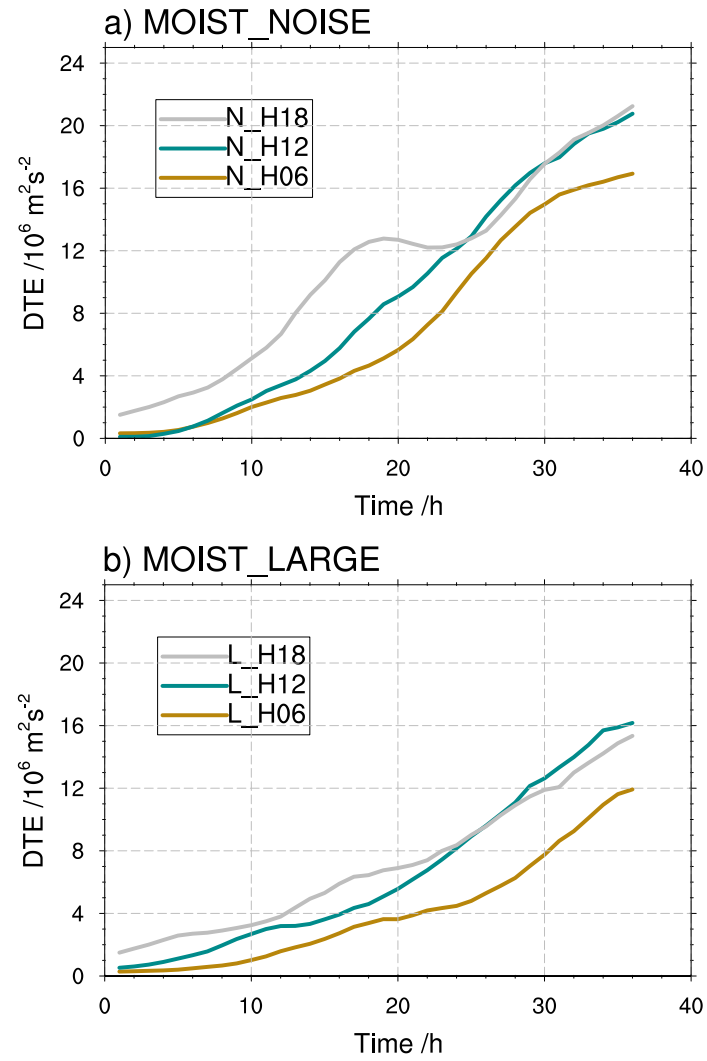
Figure **2-8.** Evolution of domain integrated DTE for various MOIST_NOISE and MOIST_LARGE experiments perturbed at slightly different times (see text for more details).
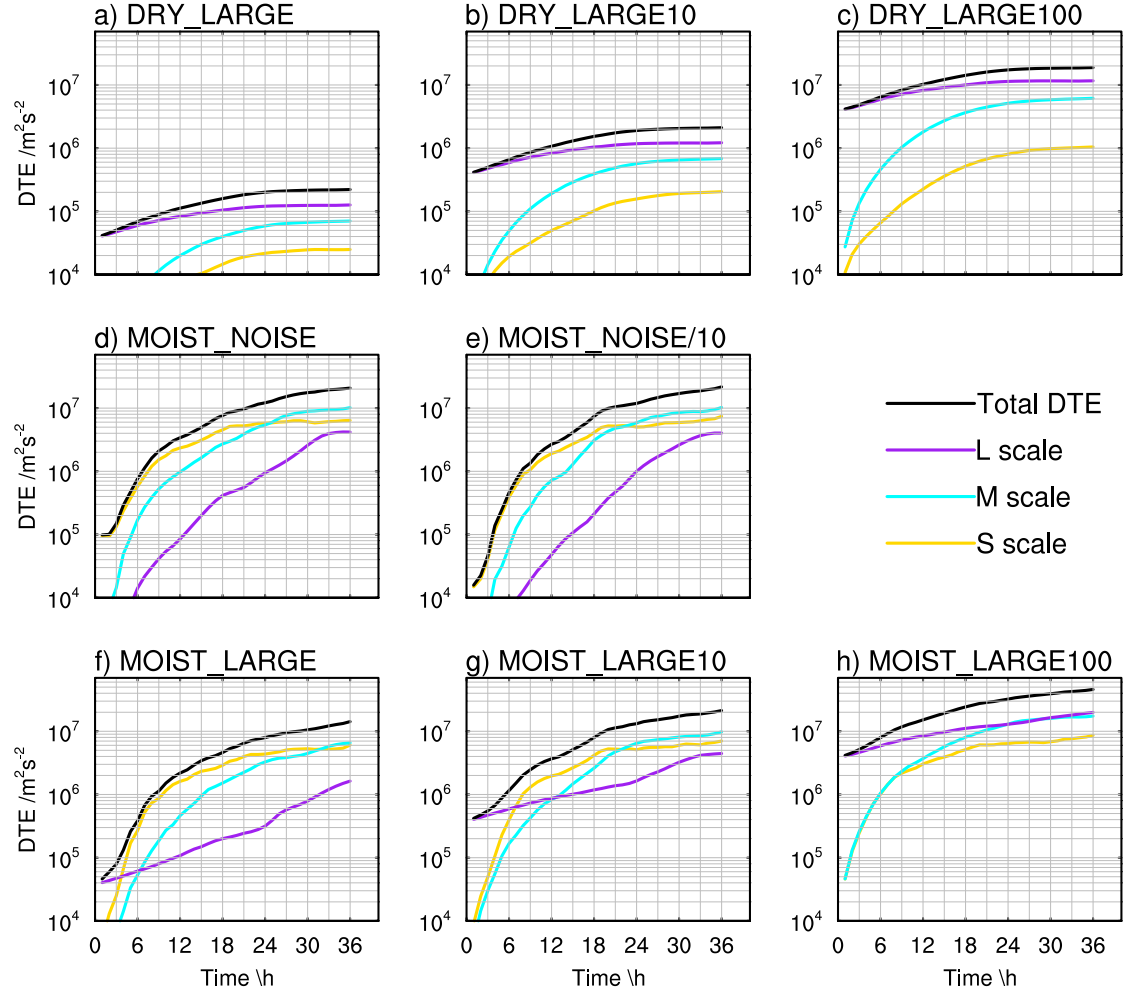
Figure **2-9.** Evolution of domain integrated DTE for different wavelength ranges (L scale: wavelength > 1000 km; M scale: 1000 km > wavelength > 200 km; S scale: 200 km > wavelength) in different experiments of various initial amplitudes. The number behind each experiment name implies the change of initial error amplitude compared with its corresponding experiment (table 1).
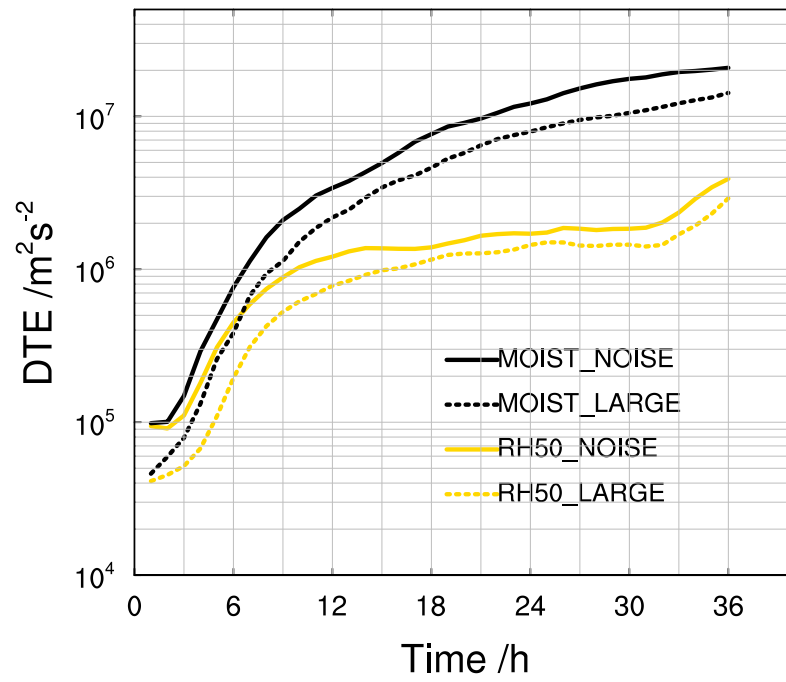
Figure **2-10.** Evolution of domain integrated DTE under different moisture environment. RH50 here means the initial Relative Humidity (RH) is reduced by half to that of the moist case.
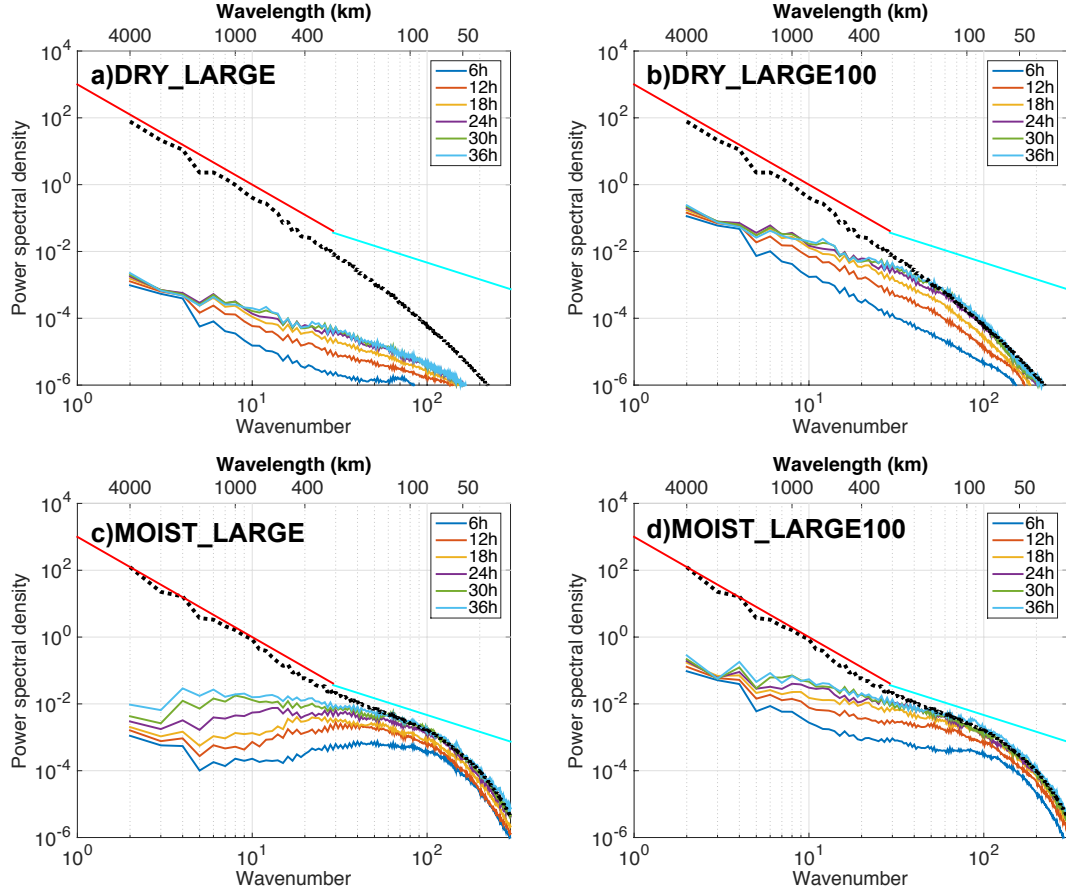
Figure **2-11.** Evolution of spectra of the DTE every 6h after different initial perturbations are added for a) DRY_LARGE, b) DRY_LARGE100, c) MOIST_LARGE, and d) MOIST_LARGE100 experiment. Dotted lines show the spectra of the full state background flow in the control experiment, averaged between 24h and 36h after the perturbation. The red and blue lines show the reference line for -3 and -5/3 power law, respectively.
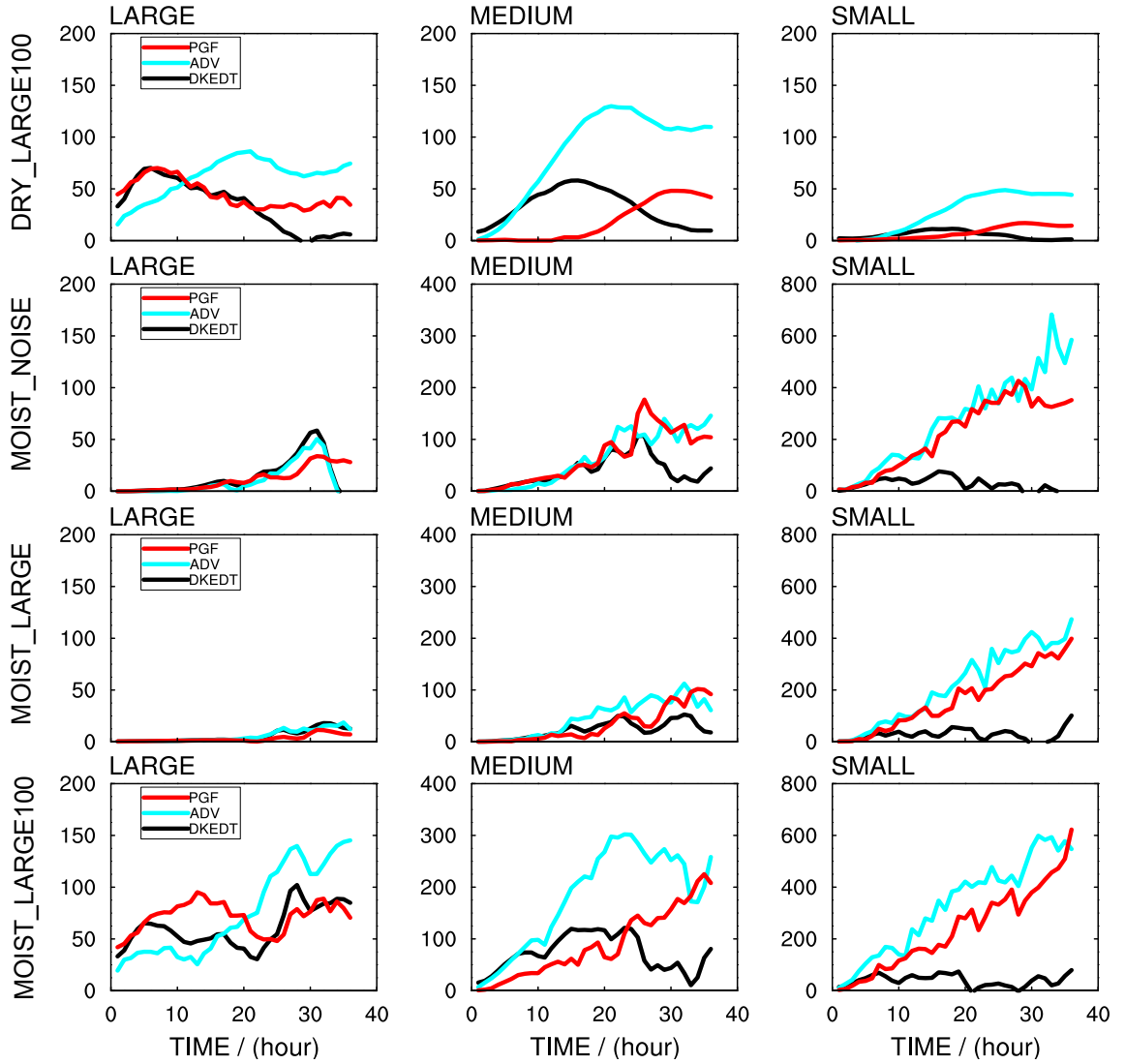
Figure **2-12.** Time series of budget calculation for the sources and sinks of the difference kinetic energy (dDKE/dt, kg m^2 s^{-3}, Equation 2.3, values are integrated over the domain) at different wavelengths within DRY_LARGE100, MOIST_NOISE, MOIST_LARGE, and MOIST_LARGE100 experiment, respectively. The cyan line represents the contribution of the advection term; the red line here represents the contribution of the pressure term, while the black line is the actual increment of DKE after diffusion and damping. Note that the DRY_LARGE100 experiment has different vertical scales from the others.
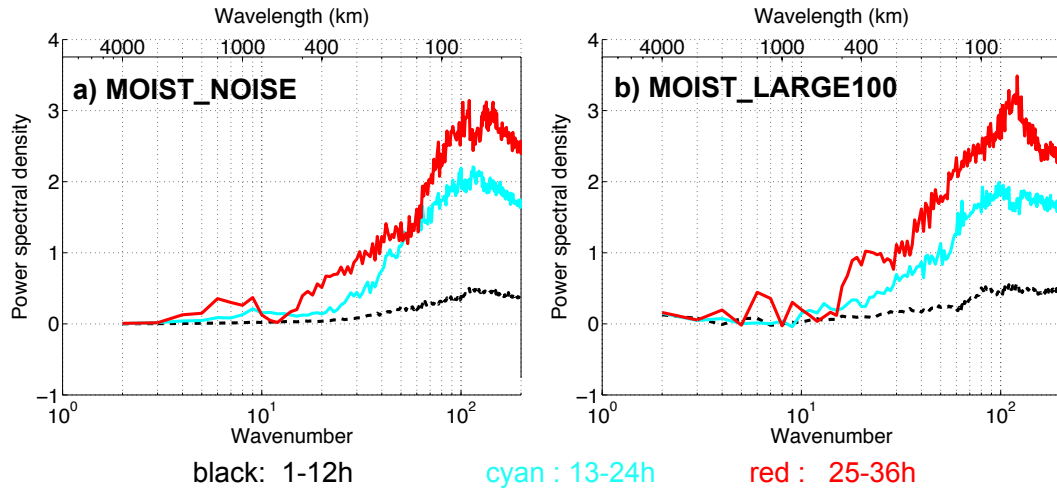
Figure **2-13.** Difference buoyancy production spectra for experiments a) MOIST_NOISE, and b) MOIST_LARGE100 environment. Black dash line, cyan line, and red line show time average over 1-12 h, 13-24 h, and 25-36 h, respectively. The buoyancy production is multiplied by the wavenumber in order to preserves the area on a log-linear plot.

Chapter Tables

Moisture / Perturbation Type	DRY	MOIST	RH50	FAKEDRY
LARGE	DRY_LARGE	MOIST_LARGE; (L_H06, L_ H12, L_H18)	RH50_LARGE	FAKEDRY _LARGE
	DRY_LARGE10	MOIST_LARGE10		
	DRY_LARGE100	MOIST_LARGE100		
NOISE	DRY_NOISE	MOIST_NOISE; (N_H06, N_H12, N_H18)	RH50_NOISE	FAKEDRY _NOISE
		MOIST_NOISE/10		

Table **2-1**. All the experiments conducted in this chapter.

Chapter 3

Contributions of moist convection and internal gravity waves to building the atmospheric "-5/3" kinetic energy spectra

3.1 Introduction

The energy spectrum of the atmosphere and its underlying physical mechanisms remain active research topics despite decades of observations and scientific research. Long-range passenger aircraft have collected velocity and temperature measurements since 1970s. These measurements indicate an energy spectrum varying as k^{-3} (k is wavenumber) or a "-3" energy spectrum at synoptic scales with a transition to a "$-5/3$" spectrum within the mesoscale (<500 km) (Nastrom and Gage 1985). Charney's theory of geostrophic turbulence (Charney 1971) is the generally accepted explanation of the synoptic scale -3 spectrum. However, there is no general agreement on the mechanism(s) behind the mesoscale -5/3 spectrum. Many hypotheses for explaining the spectrum at the mesoscale have been proposed, including, but not limited to, an inverse two-dimensional (2D) cascade of small-scale energy produced perhaps by convection (Lilly 1983), production of inertia-gravity waves (e.g., VanZandt 1982; Koshyk et al. 1999), the signature of stratified turbulence at scales where rotational constraints become less important (Lindborg 2006), and the nature of surface quasi-geostrophy (SQG) due to the development of fronts at the edge of synoptic-scale cyclones and anticyclones at the top of the troposphere (Tulloch and Smith 2006).

The above-mentioned mechanisms for the -3 and -5/3 spectra are based on idealized models. Several full-physics models have successfully captured the observed transition of the spectrum slope from -3 to -5/3 (e.g., Skamarock 2004; Hamilton et al. 2008; Skamarock et al. 2014), yet

only limited discussion has been given to explain the mechanism(s) behind it. None of these earlier studies looked into the details of the growth process of the mesoscale energy spectrum. Recently, Waite and Snyder (2013) found that moist processes could energize the mesoscale and thus help the transition of the slope. A similar full-physics idealized baroclinic wave simulation in Sun and Zhang (2016) also found this distinct transition of the simulated kinetic energy spectrum at a scale of ~400 km in their moist experiment. Interestingly the dry experiment in their study maintains the steep -3 slope all the way to the mesoscale in the upper troposphere. This result emphasizes the critical role of moist convection in the creation of the shallower -5/3 slope. Compared to the dry experiment, moist convection generates many gravity-wave-like signals at the upper levels of the troposphere (Wei and Zhang 2014, 2015; Wei et al. 2016), which might be responsible for the spectrum transition from -3 to -5/3 at those levels. More recently, Durran and Weyn (2016) shows that a -5/3 spectrum evolves and reaches to scales comparable to observations in their simulations of convective cloud systems.

Motivated by these recent findings, this study aims to investigate the mechanisms responsible for the -5/3 slope in Durran and Weyn (2016), especially the contributions of moist convection and internal gravity waves generated by convective systems. This study confirms their finding of an approximate -5/3 spectrum and provides new information for each specific height level. The remainder of the paper is organized as follows; Section 2 introduces the model setup for our simulation. Section 3 gives a brief overview of the simulation and analyzes the evolution of the mesoscale energy spectrum through a spectral energy budget. Further discussion and concluding remarks are given in section 4.

3.2 Methodology

The Weather Research and Forecast (WRF, version 3.6.1, Skamarock et al. 2008) model is used in an idealized mode for this study. The domain size of the simulation is 800km×800km, with a horizontal grid spacing of 2km. The model top is fixed at 20 km. In order to get an accurate calculation of kinetic-energy spectra budget, we have 200 layers in the vertical direction. The vertical grid spacing is approximately 100 m, although the vertical layers are not equally spaced in the WRF model. Coriolis forces are neglected, unless otherwise stated. Periodic lateral boundary conditions are implemented here to facilitate the spectral analysis. To further simplify both the model and the interpretation, we use a free-slip bottom boundary condition in the simulation. No PBL or surface scheme is used in the current simulation. Also, no cumulus or radiation parameterization are used. Near the upper boundary, an absorbing layer as described by Klemp et al. (2008) is applied for the uppermost 5 km of the model domain to reduce artificial reflection of gravity waves. This sponge layer has proved successful in the idealized squall line simulation done by Klemp et al. (2008). The Morrison scheme is used for the microphysics parameterization (Morrison et al. 2009).

Figure 3-1 shows our initial sounding profile for the simulations. It is based on Weisman and Klemp (1982), except that we fix the mixing ratio below 1 km at 14 $g\ kg^{-1}$ and cap the RH at 75% for any level above 1.4 km. A unidirectional horizontally uniform background wind profile is specified in which the zonal winds linearly increase from $-10\ m\ s^{-1}$ at the surface to $10\ m\ s^{-1}$ at a height of 5 km and remain $10\ m\ s^{-1}$ at higher levels (Fig. 3-2a).

Seven localized warm bubbles with positive temperature anomaly of 3 K are put into the initial condition to initiate convection. These warm bubbles are aligned from north to south at the domain center, with a horizontal radius of 10 km and a vertical radius of 1.5 km. Their centers lie at 1.5 km above the surface, with a horizontal distance of 20km away from each other. The warm

bubbles, each evolving into a convective cell, then interact with each other under the wind shear. The evolution of these cells will be briefly introduced in the next section. A 20-member ensemble is produced through perturbing the water vapor mixing ratio at lowest 1-km boundary layer with a Gaussian white noise of 0.5 g kg^{-1} to reduce case dependency in the statistics. All the simulations are integrated for 6 hours, with fields output every 30 seconds. The output fields are interpolated to constant height levels with a vertical interval of 50m to facilitate the calculation of the spectra.

3.3 Results

3.3.a Overview of the simulation

Before we start the spectral analysis, we would like to first take a look at the evolution of our simulation. Figure 3-3 visualizes the development of the convective cells in one member of our ensemble. Initially (0-2 h), each warm bubble evolves into a convective cell of similar scale, with a strong embedded updraft. After 2 hours, the convective cells start to interact with each other under the vertical wind shear. While the convective cells in the middle of the line get weaker, the cells at both ends of the line become stronger and "eat" all the other cells gradually. At the end of the 6-hour simulation, two supercell like systems form at both ends of the line. Slightly different from our expectations, these cells do not organize into a squall line in almost all the ensemble members. This is likely due to the relatively deep vertical wind shear in our simulation. Another possible reason is that the initial line of warm bubbles is perpendicular to the wind shear direction. Sensitivity runs of adding the warm bubbles at different zonal locations and/or adding vertical shear in the meridional direction are more favorable of the formation of a squall line. As a result of this weak organization of the convective cells, the cold pools are also relatively weak in our simulation. The grey shading in Fig. 3-3 depicts the anomaly virtual potential temperature

less than -0.5 °C. Compared to Skamarock et al. (1994), both the range and absolute value of the cold-pool temperatures are smaller, which implies a weaker convective system in our simulation. Despite these differences between our simulated convective system and previous studies, their effects on the spectrum are not critical, as we will show later in further sensitivity experiments.

Strong gravity waves can be generated by these convection cells. Figure 3-4a shows a south-north cross-section over the domain center at 2 h for the same ensemble member as shown in Fig. 3-3. The location of each convective cell can be identified by the 25 dbz reflectivity line. The region with vertical velocity greater than 0.1 m/s is shaded in cyan, while the potential temperature is plotted using gray lines. Clear gravity-wave signals generated by the convective cells can be found at levels above 12 km (lower stratosphere), where the vertical velocity and the potential temperature show a quadrature phase relationship. In the troposphere, due to turbulent motions induced by the convection cells, linear gravity-wave signals cannot be easily identified. This result is further supported by the profile of the domain averaged vertical heat transport ($\overline{w'T'}$, Fig. 3-4b). Since linear non-growing gravity waves which have a quadrature relationship between w and T do not transfer heat, we see negligible transport at levels above 12 km; whereas for the troposphere, there is considerable heat transfer due to convection. Figure 3-4c also shows the domain-averaged vertical energy flux ($\overline{w'p'}$). According to linear gravity-wave theory, upward (downward) propagation of the gravity waves leads to positive (negative) vertical energy transport. We will discuss in more detail the energy transport in the spectrum-analysis part of this study.

The convective cells and the gravity waves they generate have a downgradient effect on the mean flow (Fig. 3-2b). We see a slight increase of the mean zonal wind ($\sim 0.1 \, m \, s^{-1}$) in the 0-5-km layer; above 5 km, the mean zonal wind decreases a small amount ($\sim 0.1 \, m \, s^{-1}$). This downgradient effect leads to the loss of mean kinetic energy, which will be discussed later. The mean meridional wind is also plotted in Fig. 3-2c. With the symmetric model setting we used, the

mean meridional wind should be zero. Our calculation shows a noisy mean-v wind signal with an amplitude of $0.001\ m\ s^{-1}$ (two orders of magnitude smaller than mean zonal wind change) due to numerical error. The accuracy of our calculation demonstrates that the change of the mean zonal wind ($\sim 0.1\ m\ s^{-1}$), thus the lost of the mean kinetic energy, is due to mixing induced by convection and gravity waves.

3.3.b Kinetic energy spectra

The spectrum of the kinetic energy is calculated using the 2D discrete cosine transform (DCT) method (Denis et al, 2002; Peng et al, 2014) at each vertical level. More details on this method can be found in the Appendix. For a 2D field with periodic boundary conditions, the DCT is equivalent to the discrete Fourier transform, yet it is more generally applicable to non-periodic domains. We use a curly bracket here to denote the DCT spectral coefficients of a field q as $\{q(\mathbf{k})\}$, where $\mathbf{k} \equiv (k_x, k_y)$ is the horizontal wave vector. The dependence of spectral quantities on z and t is suppressed for clarity.

By neglecting the density perturbation, we can approximate the total horizontal kinetic energy per unit volume for each specific height level as:

$$E_h = \frac{1}{2}\bar{\rho} \iint (\mathbf{u} \cdot \mathbf{u})\, dxdy = \frac{1}{2}\bar{\rho} \iint (u^2 + v^2)\, dxdy \qquad (3.1)$$

where $\mathbf{u}$ is the horizontal wind vector, $\bar{\rho}$ is the horizontal averaged density (function of height only). The kinetic energy spectrum $E(k_h)$, can then be defined by

$$E_h = \frac{1}{2}\bar{\rho} \iint (u^2 + v^2)\, dxdy = \frac{1}{2}\bar{\rho} \iint (\{u(\boldsymbol{k})\} \cdot \{u(\boldsymbol{k})\} + \{v(\boldsymbol{k})\} \cdot \{v(\boldsymbol{k})\})\ dk_x dk_y$$

$$= \int E(k_h)\, d\, k_h \qquad (3.2)$$

where the horizontal wavenumber k_h is defined as $k_h^2 = k_x^2 + k_y^2$. The kinetic-energy spectrum $E(k_h)$ is obtained by taking the sum over wavenumber bands $k_h - \frac{\Delta k}{2} < k_h \leq k_h + \frac{\Delta k}{2}$. Note that these definitions are all based on a 2D plane, thus we will conduct the calculation at each specified height.

The derived mean kinetic energy spectra, averaged over all 20 ensemble members every 2 hours and over all the levels between 0 and 15 km, is shown in Fig. 3-5. Since the resolution of the simulation is 2km, signals with a wavelength shorter than 15 km (grey shaded area) are not well resolved by the model. The slope of the spectrum in this region falls off quickly due to implicit dissipation in the model. Any results within this range should be treated with caution. We will focus here on the well-resolved range (wavelengths > 15 km). For the first 2 hours, the energy spectrum clearly shows a peak at a scale around 20 km, which is the scale of the warm bubble and the convective cells. Note that the spectral decomposition of an isolated feature projects onto all scales and most prominently onto the largest scales, thus the initial large-scale signal in the spectrum analysis is mainly due to the projection of energy associated with the limited extent of the convective cells. After 2 hours, the growth of the spectrum extends to larger scales. For the time period between 4-6 h, the energy spectrum approaches a quasi -5/3 slope for scales shorter than 100 km. Although there are slightly different evolutions of the convective cells in the 20 members, the evolution of the kinetic energy spectrum is insensitive to the details of the convective cells. All the 20 members have formed the quasi -5/3 slope as in the ensemble mean result after 6 hours of integration. This is consistent with Durran and Weyn (2016), which shows that the kinetic energy spectrum with a slope close to -5/3 could indeed be built solely from convection. Further examinations with a smaller time interval (not shown) indicate that the kinetic energy spectrum at scales smaller than 100 km becomes quasi-steady after 5h when it reaches the "-5/3" slope. We also did one experiment with slightly different model settings in

which the simulation was integrated for eight hours. The supercells in that experiment maintain themselves and bring the spectrum at larger scale (> 100km) closer to the -5/3 reference line, though the change is much slower. The growth process of the quasi -5/3 slope for scales < 100 km in our ensemble experiments is the focus of this study.

The kinetic energy spectrum can also be further decomposed into horizontally rotational and divergent parts, $E_R(k_h)$ and $E_D(k_h)$, which are given by

$$\int E_R(k_h)\, dk_h = \iint \frac{1}{2}\bar{\rho}\frac{\{\boldsymbol{\zeta}\}\cdot\{\boldsymbol{\zeta}\}}{k_h^2} dk_x dk_y, \quad (3.3)$$

$$\int E_D(k_h)\, dk_h = \iint \frac{1}{2}\bar{\rho}\frac{\{\boldsymbol{\sigma}\}\cdot\{\boldsymbol{\sigma}\}}{k_h^2} dk_x dk_y, \quad (3.4)$$

where $\boldsymbol{\zeta}$ and $\boldsymbol{\sigma}$ are the vertical vorticity and horizontal divergence, respectively. Figure 3-6 shows the result after the decomposition. Unlike previous studies involving baroclinic waves and moist convection (e.g., Waite and Snyder 2013), the divergent energy spectrum in the present physical situation is not the only component responsible for the shallower -5/3 slope. At the end of the simulation (4-6 h), the rotational kinetic energy also has a quasi -5/3 slope within the wavelength range of 15-100 km. The magnitude of the rotational kinetic energy within the -5/3 slope range (15-100 km) is even slightly larger than that of the divergent kinetic energy. A closer look shows that the ratio of the divergent to the rotational kinetic energy increase with height. In the troposphere, the amplitude of the rotational kinetic energy is stronger, due to the mesoscale convective vortices produced by the convective systems (Davis and Weisman 1994). While in the lower stratosphere, the divergent kinetic energy dominates over the rotational kinetic energy, as gravity waves are the primary signals there. Analysis of observational datasets in previous studies led to different conclusions with regard to the ratio of divergent to rotational kinetic energy. Callies et al. (2014) conclude that the divergent component of the kinetic energy is slightly stronger for the mesoscale energy spectrum. On the contrary, other studies find that the rotational

kinetic energy is more important (Cho et al. 1999; Lindborg 2015). Difference in data analysis and dataset might be responsible for different conclusions (Bierdel et al. 2016). Further study is clearly needed to reach agreement on this.

Figure 3-7 shows the kinetic energy spectrum averaged over 0-4 km, 6-10 km, and 12-15 km (lower troposphere, upper troposphere, and lower stratosphere, respectively). The kinetic energy is stronger in the troposphere than it is in the stratosphere due to decreasing density with height. What is more interesting is that, although it differs slightly[1], an approximate -5/3 slope in the wavelength range 15~100 km does show up at all levels throughout the atmosphere towards the end of our simulation (Fig. 3-7). The upper troposphere, where aircraft measurements lie, is not the only level that has a spectrum slope of -5/3; the lower troposphere and the lower stratosphere also have such a slope. The present model thus offers an alternative to the surface quasi-geostrophic hypothesis in Tulloch and Smith (2006). Since no surface scheme or boundary layer scheme is adopted in our simulation, the creation of the kinetic spectrum is clearly due to the convection systems (diabatic heating, which has a maximum in the upper troposphere and a close to zero value near the surface and above the tropopause). Any boundary process plays at most a secondary role since no PBL or surface scheme is used in our simulations.

3.3.c Spectral budget analysis

More insight can be gained into the dynamics of the horizontal kinetic energy spectrum by examining processes contributing to the evolution of the spectrum. The tendency of the kinetic energy spectrum is shown in Fig. 3-5b. The derived tendency term is multiplied by wavenumber k in order to preserve the area in this log-linear plot. Even after this multiplication, for an energy

---

[1] The calculated linear-fit slope varies from -1.61 to -2.05 for wavelength between 16 and 100 km at different height levels during 4-6 h of our simulations. The steeper slope of -2 mainly lies in the stratosphere, especially where the gravity-wave signal is relatively weak. For the constant-Coriolis experiment shown in Fig.3-11, the slope range is much smaller (-1.64 ~ -1.72) due to more organized convection.

spectrum with a -5/3 power-law slope, it can be proven that the tendency term will decrease with decreasing scale, as is shown by the black line for the range of wavelengths smaller than 100 km. To be clear on the sources and sinks for the energy spectrum $E(\boldsymbol{k})$, we compute the budget equation for $E(\boldsymbol{k})$:

$$\frac{\partial E(\boldsymbol{k})}{\partial t} = A(\boldsymbol{k}) + P(\boldsymbol{k}) + D(\boldsymbol{k}), \qquad (3.5)$$

where the $A(\boldsymbol{k})$ term is the energy transfer due to advection,

$$A(\boldsymbol{k}) = -\bar{\rho}\{\boldsymbol{u}\} \cdot \left\{ \boldsymbol{u} \cdot \nabla_h \boldsymbol{u} + w\frac{\partial \boldsymbol{u}}{\partial z} \right\}, \qquad (3.6)$$

the $P(\boldsymbol{k})$ term is the spectral tendency due to the horizontal pressure gradient. If we adopt the Exner function form of the pressure gradient force, $P(\boldsymbol{k})$ can be written as:

$$P(\boldsymbol{k}) = -\bar{\rho}\{\boldsymbol{u}\} \cdot \left\{ C_p \theta_v \nabla_h \pi' \right\}, \qquad (3.7)$$

where C_p is the heat capacity at constant pressure, θ_v is the virtual potential temperature, and π' is the anomaly Exner function. The quantity $D(\boldsymbol{k})$ in equation 5) is simply the dissipation.

As the nonlinear term in the momentum equation, advection is responsible for all the interactions across different scales. The $A(\boldsymbol{k})$ term in spectral budget equation acts to redistribute energy between different scales. However, the level-by-level transfer caused by $A(\boldsymbol{k})$ is not strictly conservative; that is, its sum over all wavenumber k is not zero. In addition to the conservative exchange of kinetic energy between different wavenumbers, $A(\boldsymbol{k})$ has a contribution from the divergence of vertical kinetic energy flux. To resolve this issue, the $A(\boldsymbol{k})$ term can be further decomposed as:

$$A(\boldsymbol{k}) = \underbrace{-\bar{\rho}\{\boldsymbol{u}\} \cdot \left\{ \boldsymbol{u} \cdot \nabla_h \boldsymbol{u} + \frac{\boldsymbol{u}(\nabla_h \cdot \boldsymbol{u})}{2} \right\} - \frac{1}{2}\bar{\rho}\{\boldsymbol{u}\} \cdot \left\{ w\frac{\partial \boldsymbol{u}}{\partial z} \right\} + \frac{1}{2}\bar{\rho}\left\{ \frac{\partial \boldsymbol{u}}{\partial z} \right\} \cdot \{w\boldsymbol{u}\}}_{T(k)}$$

$$\underbrace{-\frac{1}{2}\frac{\partial(\bar{\rho}\{\boldsymbol{u}\} \cdot \{w\boldsymbol{u}\})}{\partial z}}_{divergence\ of\ vertical\ energy\ flux}, \qquad (3.8)$$

proof of this decomposition is given in the Appendix. By separating the vertical energy flux term out, $T(\boldsymbol{k})$ is the strictly conservative term we need, i.e., the sum of $T(\boldsymbol{k})$ over wavenumber k is zero (Appendix, Eq.(E5)).

Similarly, $P(\boldsymbol{k})$ also includes a contribution due to the divergence of the vertical energy flux. As derived in the Appendix, the $P(\boldsymbol{k})$ term can be rewritten as;

$$P(\boldsymbol{k}) \sim \underbrace{C_p \frac{\partial}{\partial z}(\bar{\rho}\bar{\theta}\{w\}\cdot\{\pi'\})}_{divergence\ of\ vertical\ energy\ fluxes} + \underbrace{C_p\bar{\rho}\bar{\theta}\{w\}\cdot\left\{\frac{\partial\pi'}{\partial z}\right\}}_{B(k)}, \qquad (3.9)$$

where $B(\boldsymbol{k})$ is the buoyancy flux, which reflects the conversion between potential and kinetic energy. Combining the two flux terms in 8) and 9), equation 5) becomes

$$\frac{\partial E(\boldsymbol{k})}{\partial t} = T(\boldsymbol{k}) + B(\boldsymbol{k}) + Flux(\boldsymbol{k}) + D(\boldsymbol{k}) \qquad (3.10)$$

Figure 3-8 shows the contribution of all the terms in (5) and (10) as a function of horizontal wavenumber k_h summed over each wavenumber band. The dissipation term (Fig. 3-8c) has a negative contribution and mainly acts at small scales, as expected. When integrated over all the vertical levels, the flux term should go to zero; our calculation shows very small negatives (Fig. 3-8f). The reason is that the calculation is done over the levels below 15 km and there is still a very small portion of the energy propagating to higher levels (Fig. 3-4c). Nonetheless, this contribution is tiny. Given that the $A(\boldsymbol{k})$ term could be written as the sum of the $T(\boldsymbol{k})$ term and a flux term, as shown in equation (9), we found an almost identical shape between $A(\boldsymbol{k})$ term and $T(\boldsymbol{k})$ term when integrated over the whole domain (0-15 km, Fig 3-8a,d). The same argument can be applied to the $P(\boldsymbol{k})$ term (Fig. 3-8b) and the $B(\boldsymbol{k})$ term (Fig. 3-8e). Moreover, the consistency between these terms also imply the anelastic approximation used to decompose these terms is valid. Also note that some of the terms shown here and in the following figures have peaks in the not-well resolved gray shaded spectral bands where subgrid mixing can be important. Our experiment with a different diffusion scheme gives similar results which makes us more confident

in the present finding. Nonetheless, as mentioned earlier, results in this region of wavenumber space should be interpreted with caution.

The sum of $T(k)$ over the wavenumbers shown on Fig. 3-8d (wavelength < 800 km) is greater than zero. Since the sum of $T(k)$ over all wavenumbers adds to zero, there must be a loss of energy from the mean flow (i.e., $T(0)$ is negative). This loss was implied by the downgradient mixing process shown in Fig. 3-2b. If we check the 6-h average of the $T(k)$ term (black line), positive values of $T(k)$ are found mainly in small scales, whereas $T(k)$ is close to 0 at scales greater than 100 km. This result seems to indicate that the small-scale features could directly withdraw energy from the mean flow, not necessarily through a cascade effect[2] from the large scales.

Compared to the $T(k)$ term (Fig. 3-8d), a more important source for $E(k)$ is the buoyancy production $B(k)$ term (Fig. 3-8e, conversion from potential energy). For the whole domain, $B(k)$ is positive at almost all the scales, with a peak at the small convective scales and a plateau at larger scales. A closer look at the $B(k)$ term at different time periods tells us that this plateau is closely related to the convective organization. Initially (0-2h), $B(k)$ has a secondary maximum at around 100 km, which is roughly the length of the warm bubble line we added in the initial condition. At later times (3-4 h), this secondary maximum shifts towards larger scales due to the elongation of the convective systems in the meridional direction. At the end of the simulation, only two strong supercell-like systems remain, thus $B(k)$ is slightly smaller and the location of the secondary maximum of $B(k)$ also shifts towards the scale of the supercells.

The $E(k)$ budget analysis for different levels is given in Fig. 3-9, averaged over 0-4 km, 6-10 km, and 12-15 km, respectively. Since the kinetic energy spectra at these levels generally follow a similar quasi $-5/3$ power law (Fig. 3-7), the tendency of the spectra averaged every 2

---

[2] In classical turbulence theory, an energy cascade often refers to the transfer of energy from larger scales of motion to smaller scales –also called a direct energy cascade. If T(k) is negative at relative larger scales and positive at small scales, this is consistent with the cascade picture. Otherwise it is not.

hours at these different levels also follows a similar shape to that in Fig. 3-5b**.** The dissipation term $D(\boldsymbol{k})$ (not plotted) also maintains its shape in Fig. 3-8c for each height level. Attention here will be focused on the $T(\boldsymbol{k})$, $B(\boldsymbol{k})$ and $Flux(\boldsymbol{k})$ terms where significant differences between the vertical levels are found.

Figure 3-9e shows that in the upper troposphere, the diabatic heating is the strongest which is reflected in $B(\boldsymbol{k})$ reaching its largest amplitude with a peak at the small convective scales and a plateau at larger scales consistent with the domain-averaged profile in Fig. 3-8. However, the strong positive contribution of $B(\boldsymbol{k})$ is largely cancelled by the $Flux(\boldsymbol{k})$ term at this level (Fig. 3-9f). From Fig. 3-4c, we know that there is an increasing upward vertical energy transport in the upper troposphere (thus a positive value for the divergence of the energy flux), which explains the negative contribution of the $Flux(\boldsymbol{k})$ term; the energy withdrawn by the energy flux term at this level is deposited into both the lower troposphere and the lower stratosphere.

In the lower troposphere, the buoyancy production has a smaller effect (Fig. 3-9b). It is positive at scales larger than 50 km, likely due to the formation of the cold pools that contain organized downdrafts and negative potential temperature anomalies due to evaporative cooling. The negative $B(\boldsymbol{k})$ at small scales is linked to the lifting parcels that overcoming the convective inhibition (CIN). The total contribution of the $B(\boldsymbol{k})$ term integrated over all wavenumbers is largely cancelled by these two processes and may be even slightly negative at some levels (Fig. 3-4c). The input energy flux by the $Flux(\boldsymbol{k})$ term (Fig. 3-9c) is the primary contributor for the lower troposphere, it is positive at all but the smallest (convective) scales. Note here both $B(\boldsymbol{k})$ and $Flux(\boldsymbol{k})$ have little or negative contribution at small/convective scales, in the meantime we know $D(\boldsymbol{k})$ also has a strong negative contribution at small scales, hence, to generate a -5/3 spectrum, $T(\boldsymbol{k})$ must balance all the negative contribution at small scales and remove some extra forcing at larger scales, as is shown in Fig. 3-9a. The shape of $T(\boldsymbol{k})$ in the lower troposphere suggests a downscale-cascade scenario; however, this downscale "cascade" is still considerably

different from that of the classic three-dimensional turbulence theory since the forcing of $B(\boldsymbol{k})$ and $Flux(\boldsymbol{k})$ acts at all the scales, and unlike the classical turbulence theory, there is not a well-defined inertial subrange here. As also suggested by Waite and Snyder (2009), it is possible that the mesoscale kinetic energy spectrum does not arise from a cascade process.

Figure 3-9i shows that in the lower stratosphere, convection-generated gravity waves inject a significant amount of energy mainly into small scales through the $Flux(\boldsymbol{k})$ term. This term serves as the dominant source for the kinetic energy in this region. The $B(\boldsymbol{k})$ term has zero contribution everywhere except for the small convective scales where it is slightly negative likely due to some overshooting air parcels. The $T(\boldsymbol{k})$ term (Fig. 3-9g) acts to redistribute the injected energy into different scales to maintain the approximate -5/3 spectrum. Since the injected energy is mostly at small scales, we can find negative contribution of the $T(\boldsymbol{k})$ term at small scales and slight positive contribution of $T(\boldsymbol{k})$ term at relative large scales (16 ~100 km).

In summary, although all the levels yield an approximate -5/3 spectrum slope, the underlying physical processes behind them are substantially different. Both the downscale process [e.g. $T(\boldsymbol{k})$ at the lower troposphere] and the upscale process [e.g. $T(\boldsymbol{k})$ at the lower stratosphere] appear to exist at the same time. The vertical energy flux terms are also critical for each specific level, implying a strong connection between the energy spectrum slopes at different vertical levels.

3.3.d sensitivity experiments

In the above simulations, we use an ensemble of 20 members to reduce the case dependency of our results. Yet, all these members use the same model setup and physics schemes. To ensure that our results are robust, various sensitivity runs are also conducted. Figure 3-10 shows the kinetic energy spectrum for the DOUBLE experiment, where the horizontal size of the domain is doubled to 1600km×1600km. Similar approximate -5/3 spectrum shows up again for this

experiment. Moreover, additional experiments containing different model setups (e.g. different boundary conditions, reduced vertical layers, different shear profiles) all give similar -5/3 spectrum (not shown), implying that the -5/3 spectrum generated by the convective systems is not sensitive to the model setup.

The stratified turbulence theory proposed by Lindborg (2006) requires that vertical scales of U/N (U is the horizontal wind, while N is the Brunt–Väisälä frequency, U/N is around 1 km in the troposphere) be well resolved to drive the $-5/3$ mesoscale energy spectrum. In our simulation with only 40 vertical layers (a vertical grid spacing of ~500 m), the quasi -5/3 spectrum is still very clear. As we mentioned above, with the strong $B(\mathbf{k})/Flux(\mathbf{k})$ terms at all scales, it is likely that the turbulent motion due to convective systems is different from what a classic turbulent theory would expect. The vertical resolution requirement for resolving the stratified turbulence proposed by Lindborg (2006) is not satisfied in our simulation. Note here, this does not mean that theories invoking stratified turbulence to explain the mesoscale spectrum and transition are invalid (Skamarock et al. 2014).

As for the impact of different model physics, microphysics is the only parameterization scheme used here and we do not expect significant differences for the kinetic energy spectrum if other microphysics schemes were adopted. Hence, instead of changing any of the physics scheme, a constant Coriolis parameter (f = 1.0e-4 s^{-1}) is added to the model, which would affect the organization of the convective cells (Skamarock et al. 1994). Consistent with Skamarock et al. (1994), the evolution of the convective cells with Coriolis effect exhibits significant asymmetries. At later hours of the simulation, the convective cells at the southern part of the domain center become much stronger than that in the control no-Coriolis simulations, while convective cells in the northern part decay. This asymmetry leads to a systematic reorientation and the convective system moves towards the right of the wind shear. Due to this asymmetry, the convective cells,

especially at the southern flank, tend to be more organized and form a quasi-squall-line structure, the intensity of the system is also stronger than that of the no-Coriolis experiment.

Figure 3-11 shows the kinetic energy spectrum for the experiment with the Coriolis effect. Compared with the no-Coriolis experiment, the energy spectrum is stronger, especially for the later times of the simulation when the -5/3 spectrum extends to a scale of 400 km at the upper troposphere. The $E(k)$ budget analysis better explains the difference (Fig. 3-12). The results in the first 4 hours (blue lines) are qualitatively and even quantitatively similar to the no-Coriolis experiment. After 4 hours (red and yellow lines), due to the formation of the squall line on the southern flank, the buoyancy production $B(k)$ term becomes much stronger in the upper troposphere (Fig. 3-12e), which also causes the enhancement of the $Flux(k)$ term (Fig. 3-12f) and adjustment of the $T(k)$ term (Fig. 3-12d). The $T(k)$ term shows some negatives at relatively smaller scales and is positive at larger scales in the upper troposphere (Fig. 3-12d), which implies some kind of upscale propagation of the kinetic energy. In the lower troposphere, the stronger convective systems with Coriolis effects also bring a peak of $B(k)$ term at scale around 50 km (Fig. 3-12b), which leads to a negative $T(k)$ contribution at this scale (Fig. 3-12a). Significant differences with the no-Coriolis experiment also exist in the lower stratosphere, where stronger gravity waves generated by enhanced convection gives much stronger $Flux(k)$ term (Fig. 3-12i) at small scales, leading to an enhanced upscale propagation by the $T(k)$ term (Fig. 3-12g). The positive contribution of $T(k)$ term at relatively large scales (25–200 km wavelengths) is much more evident in this layer compared to the no-Coriolis experiment.

3.4 Discussion and Concluding Remarks

Using an ensemble of high-resolution cloud-model simulations, this study explores the kinetic energy spectrum of organized convective systems under vertical wind shear. Our results

further confirm a recent finding by Durran and Weyn (2016) showing that convective systems alone could generate a background mesoscale kinetic energy spectrum with a slope proportional to the -5/3 power of the wave number. Building upon this result, the present study gives a picture of the growth processes of the -5/3 spectrum in this physical situation. At each specific height level, the physical processes actively contribute to the formation of the kinetic energy spectrum are: 1) conversion from available potential energy to kinetic energy (buoyancy production or $B(k)$ term), which primarily lies in the mid-upper troposphere, with a peak at small convective scales and a plateau at larger scales; 2) divergence of the vertical energy flux ($Flux(k)$ term) which withdraws the energy generated by buoyancy in the upper troposphere and deposits it into both the lower stratosphere and the lower troposphere; and 3) filling out of the energy spectrum through nonlinear interactions ($T(k)$ term) among different scales.

Sensitivity experiments of varying domain size or boundary conditions all give similar approximate -5/3 spectrum in our simulations. Thus our results are very robust in terms of different model settings. The -5/3 spectrum is also not affected by the organization of the convective systems. In the experiment with a constant nonzero Coriolis parameter, the interaction between different convective cells is greatly altered especially at later times of the simulation. Thus the forcing terms of the kinetic energy spectrum (e.g., $B(k)$ term) also change accordingly. Yet the kinetic energy maintains the approximate -5/3 spectrum through adjustment of the nonlinear interaction ($T(k)$ term).

Although the picture that deep convection is able to generate the -5/3 spectrum resembles Lilly's hypothesis, the building up process of the spectrum is not the 2D inverse cascade as proposed by Lilly (1983). For each specific level, the divergence of vertical energy flux is critical, which means there are strong connections between different levels, and it is therefore a three-dimensional process. Moreover, buoyancy production and vertical flux of energy act at all the scales and so the dynamics cannot be described as an inertial-subrange cascade, as also pointed

out by Waite and Snyder (2009). In addition, the filling out of the energy spectrum by nonlinear interactions varies greatly between different vertical levels. It goes through a downscale propagation from the lower troposphere to an upscale-like propagation in the lower stratosphere. Both downscale and upscale processes happen at the same time but at different levels. We rarely find any true cascade signal in the simulations (consistent with Durran and Weyn 2016). Small-scale convection can even directly interact with the mean flow.

While convection is the ultimate source for the kinetic energy spectrum in our simulations, at high altitudes where the aircraft observations lie, it is the convection-generated gravity waves that are the primary contributors to $E(\boldsymbol{k})$. Since moist convection is not the only source for the gravity waves, one can see why Waite and Snyder (2009) found a -5/3 spectrum in the lower troposphere of their dry simulation since gravity waves are generated in association with a large-amplitude baroclinic wave. Nonetheless, moist convection is much more efficient and powerful in generating the gravity waves (Waite and Snyder 2013; Wei and Zhang 2014; Sun and Zhang 2016). Hence a quasi-steady -5/3 spectrum could be built within hours after strong convection is initiated as in our experiments.

A better understanding of the creation of the atmospheric energy spectrum is beneficial for the study of the atmospheric predictability. It has been proposed that the error growth behavior is closely related to the energy spectrum of the basic flow within which the errors grow (Lorenz 1969; Rotunno and Snyder 2008). For a flow with energy spectra of power law behavior (k^{-p}), studies find that if the slope $p < 3$, the error-doubling time decreases with scale and the upscale spreading of initially small-scale error provides an effective limit to the predictability of such flows. This upscale error propagation scenario has been verified by numerous studies using full physics models and simulations (e.g., Zhang et al. 2007; Selz and Craig 2015; Sun and Zhang 2016). However, if $p \geq 3$, it is concluded that there is no such limit. The implication of different

physical processes behind the simulated -5/3 spectrum for the atmospheric predictability is the subject of our future study.

We also want to emphasize that convection is not the only explanation for the observed -5/3 spectrum. We cannot rule out all the other hypotheses that have been proposed to explain the spectrum, although we have shown that some of them are not necessary in a moist environment. It is still an open question of how important convection is in the observed -5/3 spectrum of the real atmosphere. Moreover, although the current study clarifies the sources of $E(\boldsymbol{k})$ in these simulations of mesoscale convective systems, the authors have been unable to develop a simple explanation for why a -5/3 slope develops in the mesoscale range.

Chapter Figures
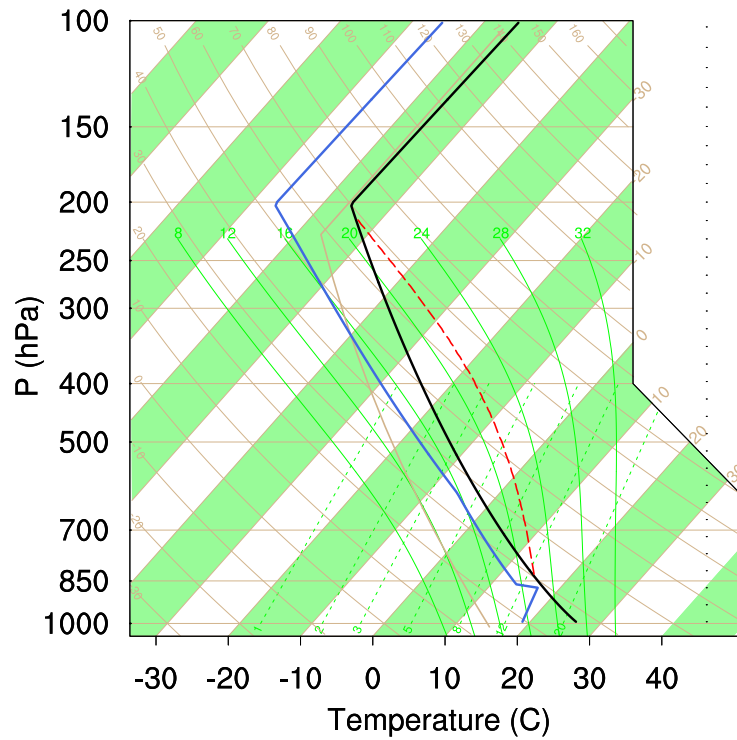
Figure **3-1.** The Skew-T diagram of thermodynamic sounding profile used for all simulations presented herein. The sounding has a CAPE value of ~2000 J kg^{-1} and a surface mixing ratio of 14 g kg^{-1}.
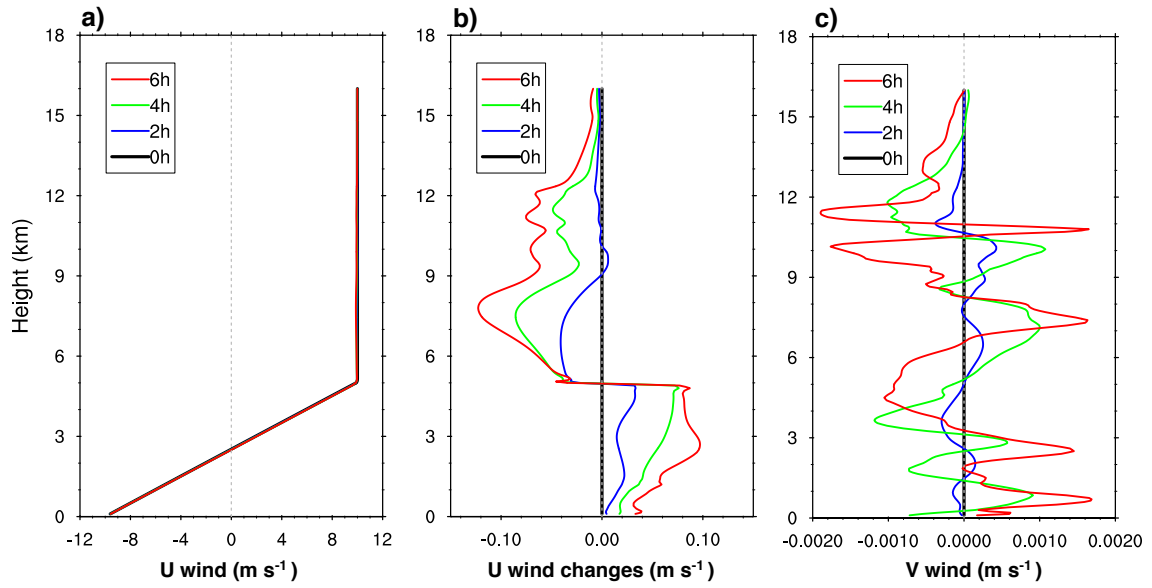
Figure **3-2.** Vertical profiles of (a) zonal mean wind, and the changes from the initial mean averaged over each horizontal plane and all 20 ensemble members for (b) zonal and (c) meridional winds.
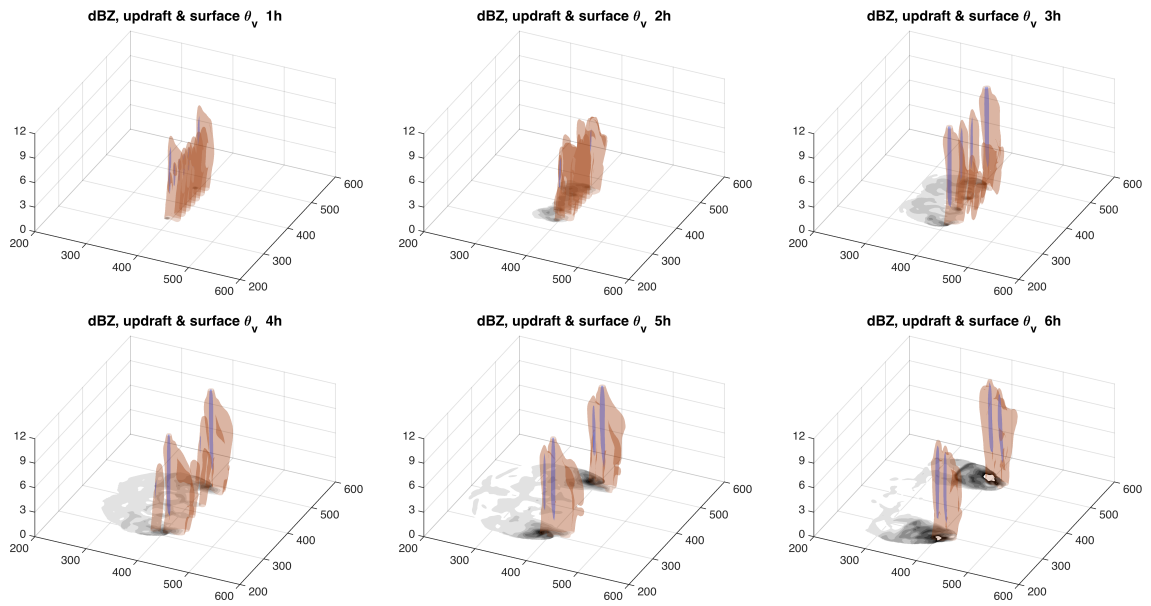
Figure **3-3.** Time evolution of simulated convective cells in one of the ensemble members. The isosurface of vertical velocity (w = 10 m s^{-1}, purple), radar reflectivity (25 dBZ, brown) and surface cold pool contours (θ_v anomaly < -0.5°C, gray) are plotted every hour.
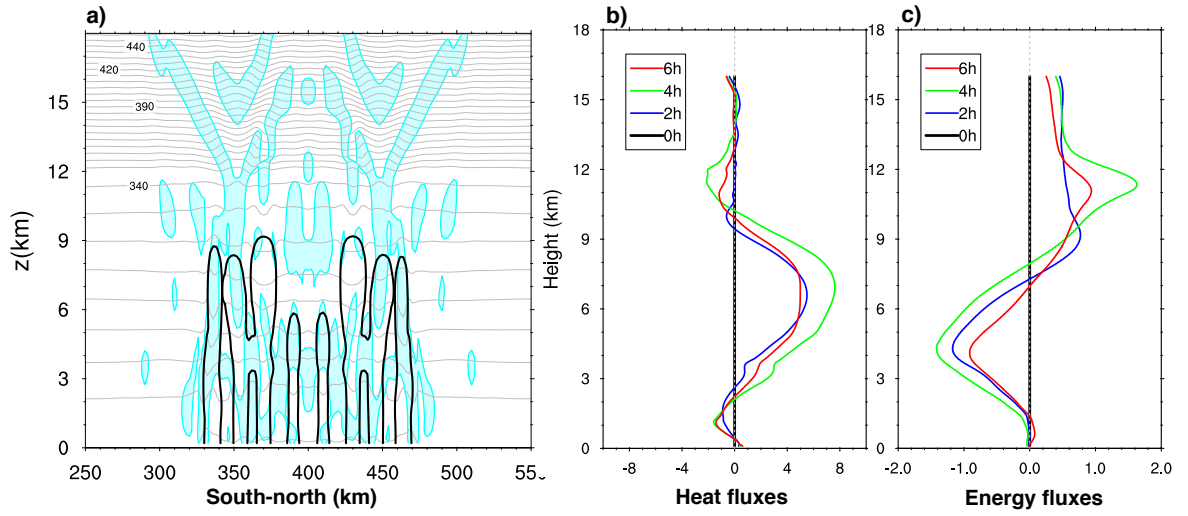
Figure **3-4.** (a) South-north cross-section at the domain center for the same member as in Fig. 3-3, showing the gravity-wave signals and convective activity (w > 0. 1 m s^{-1}, cyan shaded;   dBZ > 25, black line;   potential temperature, gray); the vertical profiles of (b) heat fluxes ($\overline{w'T'}$, $m \cdot K\ s^{-1}$ and (c) energy fluxes ($\overline{w'p'}$, $m \cdot hpa\ s^{-1}$), averaged over all 20 members and displayed every 2 h.
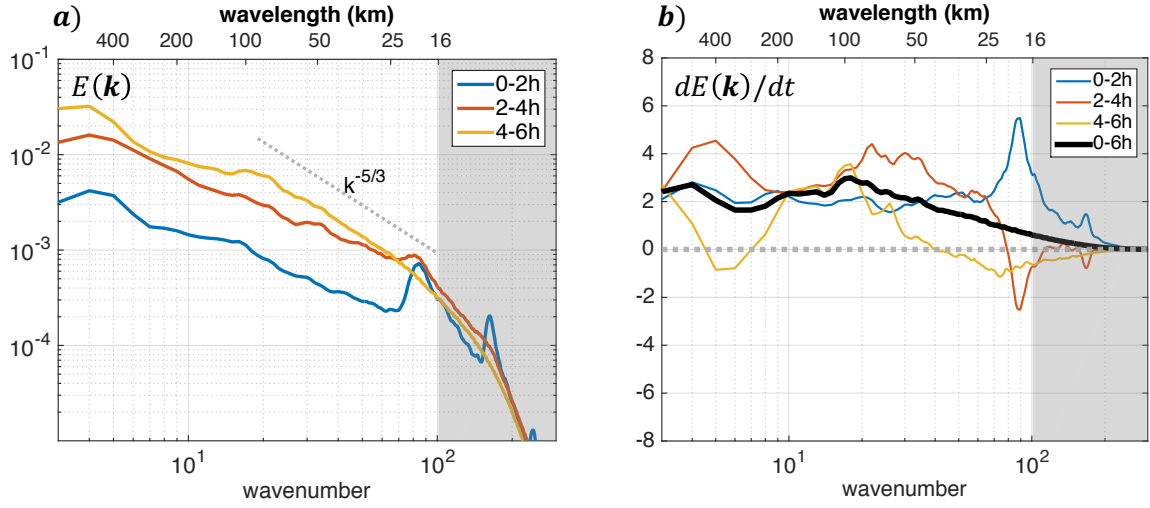
Figure 3-5. (a) Time evolution of the kinetic energy spectrum ($m^2 s^{-2} kg\ m^{-3}$), averaged between 0-15 km over every 2 hour period for all the 20 ensemble members; (b) k*dE(k)/dt term ($10^{-6} m^2 s^{-3} kg\ m^{-3}$) derived from (a). The tendency terms in (b) are multiplied by wavenumber k in order to preserves the area in a log-linear plot; black line shows time average over 0~6 h.
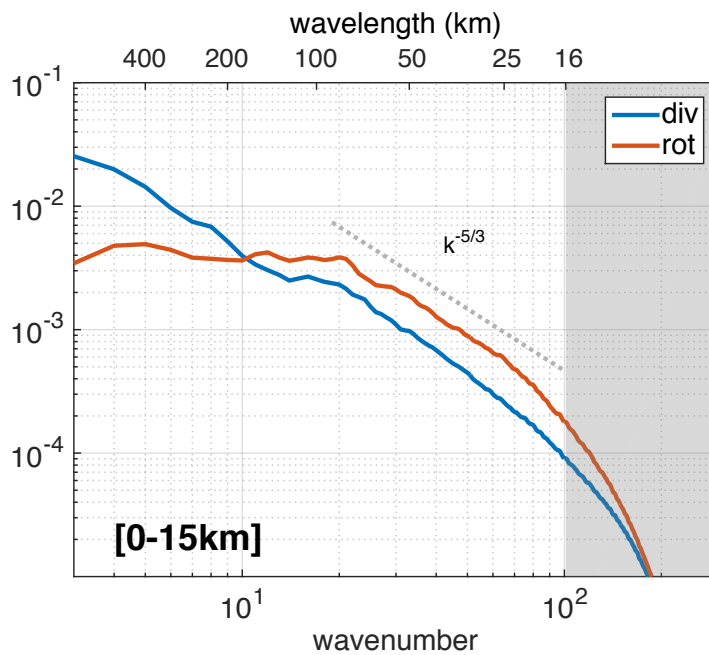
Figure **3-6.** Ensemble mean rotational (red) and divergent (blue) kinetic energy spectrum ($m^2 s^{-2} kg\ m^{-3}$) averaged between 4-6 h. The definition of rotational and divergent kinetic energy spectrum is given in the text.
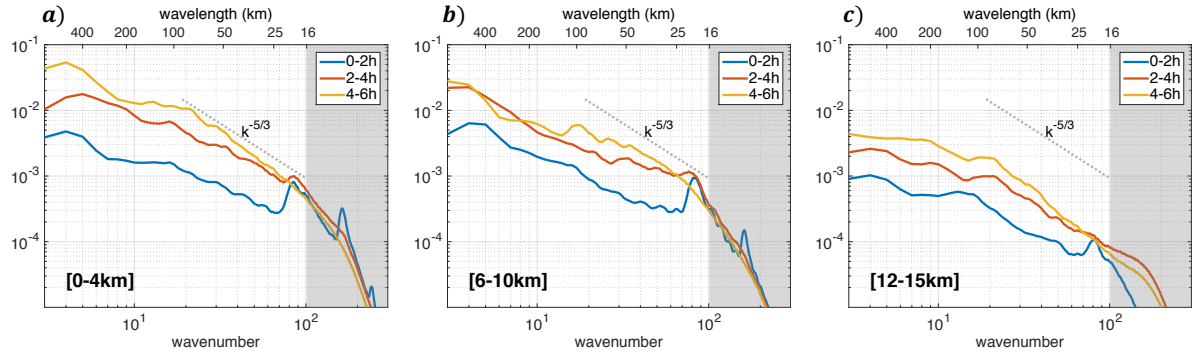
Figure **3-7.** Kinetic energy spectrum ($m^2 s^{-2} kg\ m^{-3}$) as in Fig. 3-5a but for averages over different height levels for (a) lower troposphere (0-4 km); (b) upper troposphere (6-10 km); and (c) lower stratosphere (12-15 km).
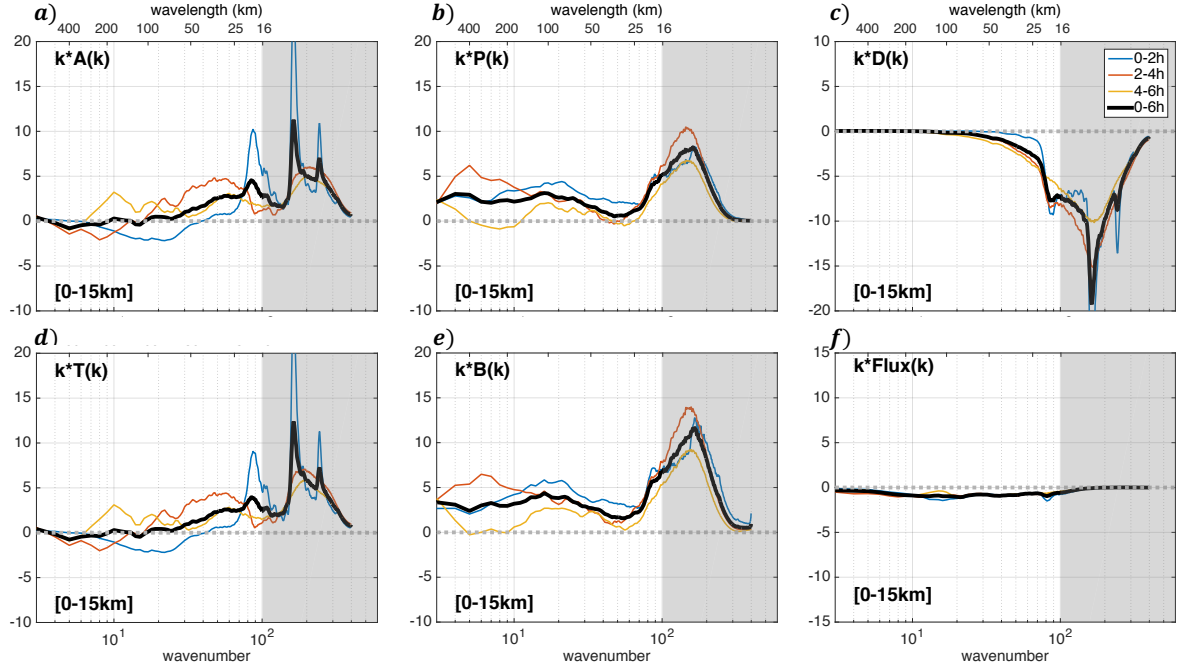
Figure **3-8.** (a-c) kinetic energy spectrum budget terms ($10^{-6}m^2s^{-3}kg\ m^{-3}$) in equation (6) and (d-f) decomposition of advection and pressure terms in equation (11) averaged over 0-15 km for all the ensemble members. Refer to the text for details on equations (6) and (11).
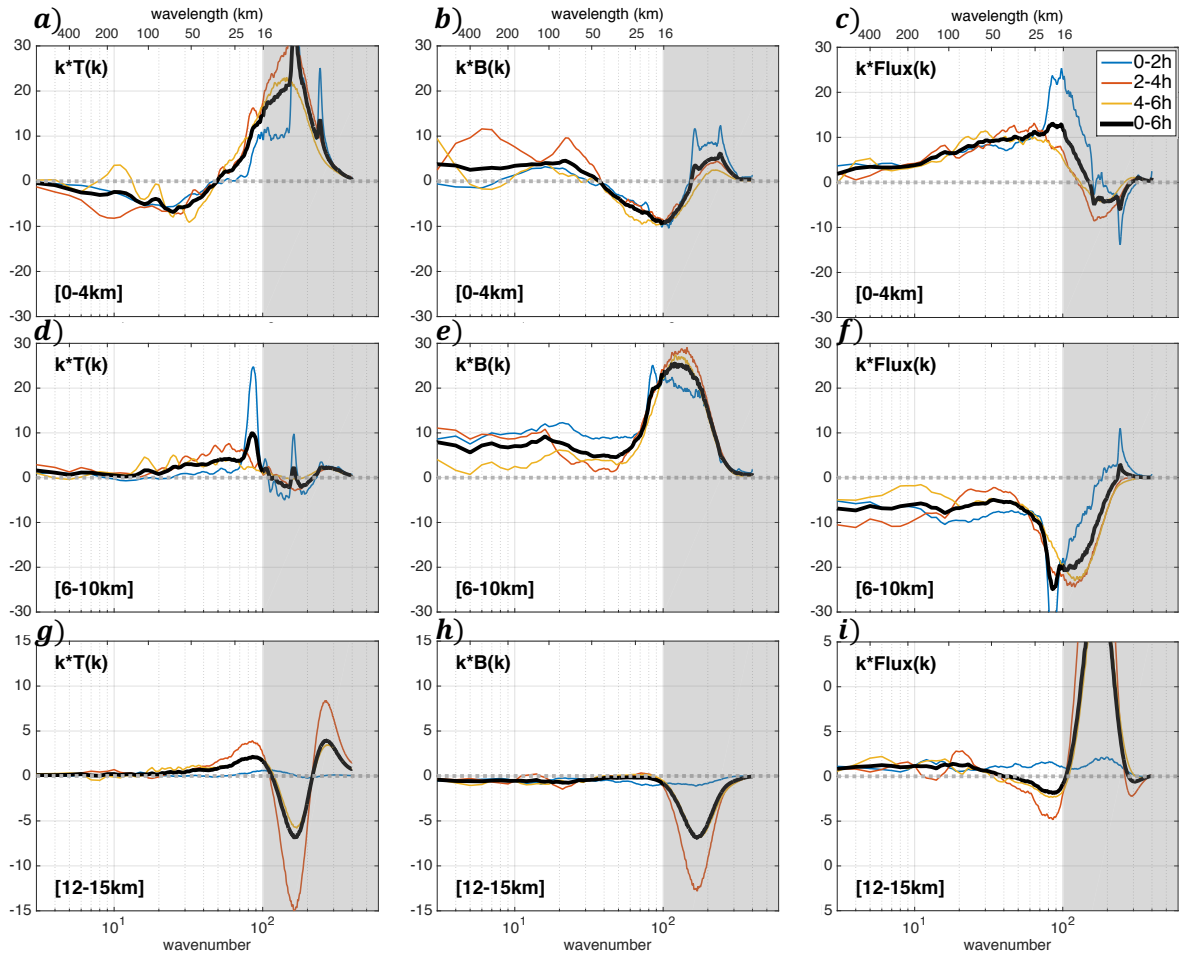
Figure 3-9. Kinetic energy spectrum budget ($10^{-6} m^2 s^{-3} kg\ m^{-3}$) analysis similar to that in Fig. 3-8 but at different height levels for (a-c) lower troposphere (0-4 km), (d-f) upper troposphere (6-10 km) and (g-i) lower stratosphere (12-15 km).
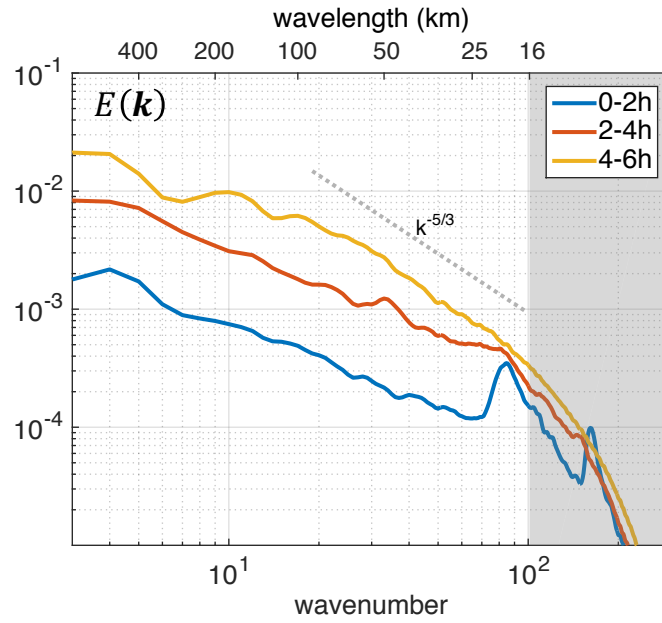
Figure 3-10. Kinetic energy spectrum ($m^2 s^{-2} kg\, m^{-3}$) same as Fig. 3-5a, but for experiment with the domain size doubled.
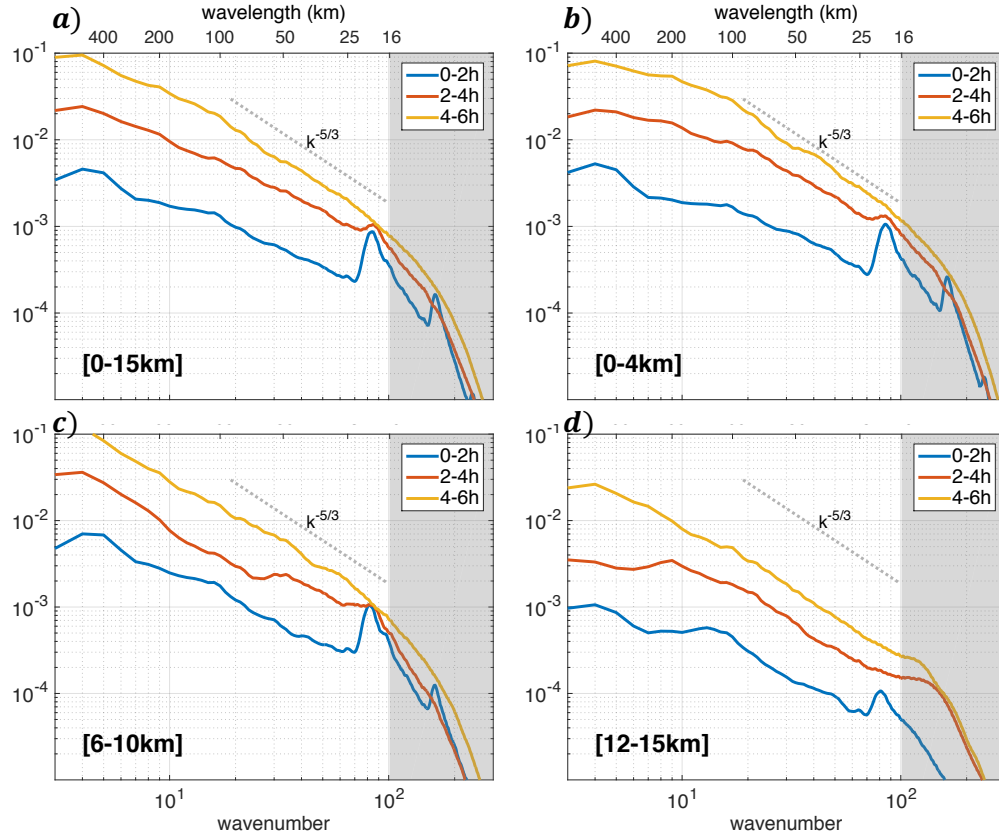
Figure **3-11.** Kinetic energy spectrum ($m^2 s^{-2} kg\ m^{-3}$) same as Fig. 3-5a and Fig. 3-7, but for experiment with constant Coriolis parameter added to the model ($f = 10^{-4}$ s^{-1}).
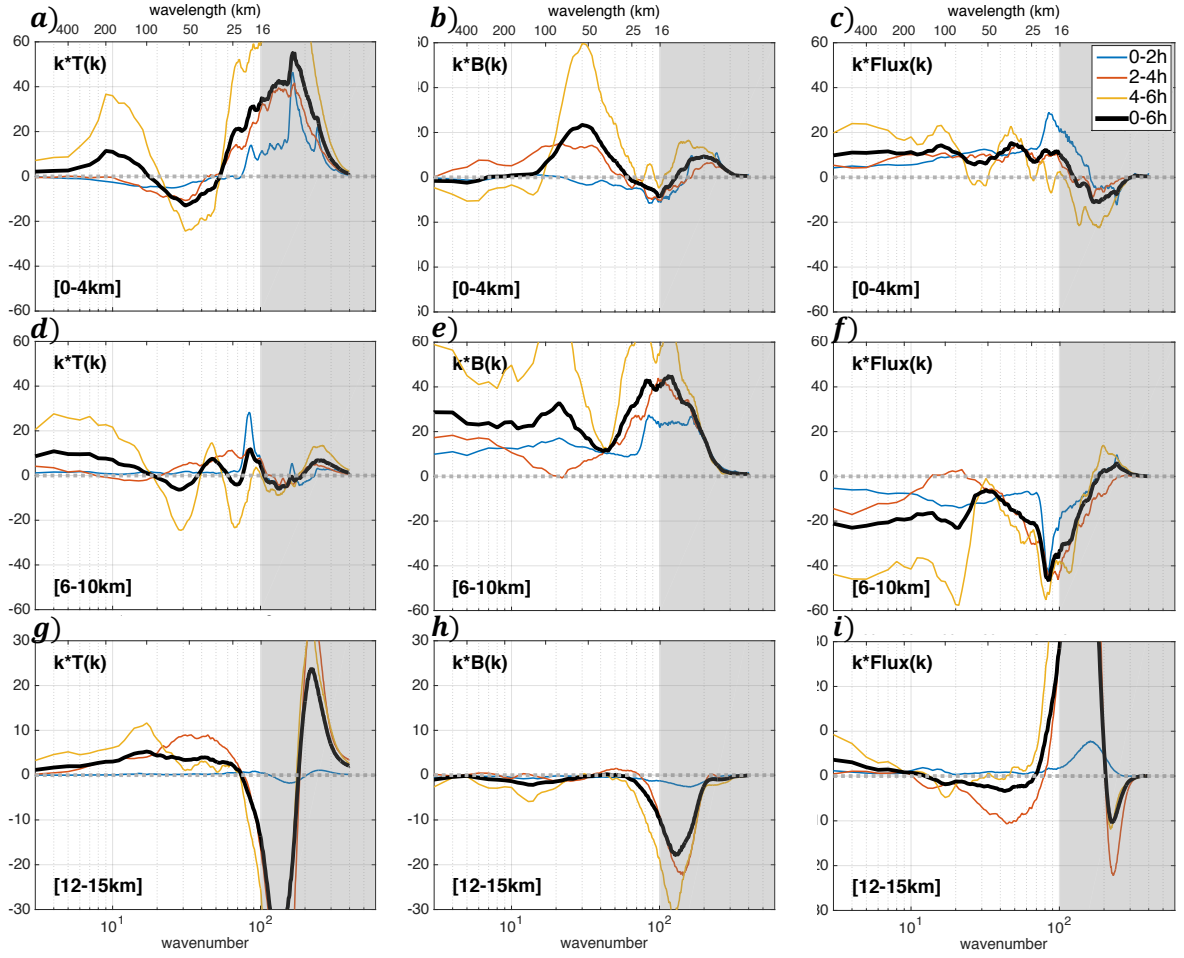
Figure **3-12.** Same as in Fig. 3-9, but for the experiment with constant Coriolis parameter.

Chapter 4

Error Growth and Ultimate Predictability limit for Mid-Latitude Weather Systems Revealed from High-resolution Global Ensembles

4.1 Introduction

The predictability of the atmosphere, as any chaotic dynamic systems, is intrinsically limited due to the so-called "butterfly effect" (e.g., Lorenz 1969; Palmer et al. 2014). This effect shows that even the smallest amplitude small-scale error will amplify and grow upscale with time, eventually rendering accurate weather prediction feasible only for a finite length of time.

Estimates of *the finite time* during which accurate predictions can be made is noted to be intimately connected with the eddy turnover times in a turbulent fluid, and these are determined by the slope of the background energy spectrum of the fluid. For a flow with energy spectra of power law behavior (k^{-p}), studies find that if the slope p < 3, the error-doubling time decreases with scale and the upscale spreading of initially small-scale error provides an effective limit to the predictability of such flows; if p ≥ 3, it's concluded that there is no such limit (Lorenz 1969; Rotunno and Snyder 2008). Observational measurements indicate that the energy spectra in the atmosphere show a distinct transition from a slope of -3 at synoptic scales to a shallower -5/3 slope at mesoscales (~500 km or smaller, Nastrom and Gage 1985). Recent study using full-physics idealized baroclinic wave simulations (Sun and Zhang 2016) using the Weather Research and Forecasting (WRF) model also found the observed transition of the kinetic energy spectrum slope at a scale of ~400 km in the moist experiment. Interestingly the dry simulation in their experiments with exactly the same initial conditon maintains a steeper -3 slope all the way to the

mesoscales. This indicate that convection might be responsible for the transition of the energy spectrum and plays a critical role in the upscale spreading of the error (Sun et al. 2017).

There have been considerable evidences and studies showing that convection is important in the growth of the forecast error (e.g., Zhang et al. 2003). Zhang et al. (2007) proposed a multistage conceptual model for error growth behavior in the moist baroclinc waves of mid-latitude: 1) the initial convective growth stage, which begins with convective instability followed by rapid error saturation [$\sim O\,(1)$ h]; 2) the intermediate adjustment stage, during which error projects to balanced field [$\sim O(2\pi/f)$]; and 3) the large-scale growth stage where error grows with larger-scale baroclinic instability. This three-stage conceptual model is demonstrated to be effective in explaining the atmospheric predictability of a real-case study by Selz and Craig (2015). They showed that 60 h after perturbing their operational forecast model with negligible initial small-scale error, the large-scale 500-hPa geopotential height error induced by upscale error growth was about half the spread of the ECMWF 6-h ensemble forecast. Further studies also show that this intrinsic growth of the error is not sensitive to the scale of the initial perturbation added (Sun and Zhang 2016; Hohenegger and Schär 2007). Moreover, moist convection not only is important for local error growth (e.g., Zhang et al. 2003), but also has implications downstream (Langland et al. 2002; Stensrud 1996; Tribbia and Baumhefner 2004). Rodwell et al. (2013) related poor forecasts over Europe to high convective Bactivities over North America a couple of days ahead, indicating that large uncertainties introduced by convection will propagate over the storm track region and might have a global effect.

Due to computational limitation, previous studies on error growth is limited to either regional model with convection-permitting resolution (e.g., Zhang et al. 2007; Selz and Craig 2015) or global simulations with coarse resolution not able to allow convection (Tribbia and Baumhefner 2004). The simulation time is often limited, usually much shorter than 10 days, which is the estimated current practical limit for the mid-latitude weather events based on the

anomaly correlation coefficient (Bauer et. al, 2015). The use of regional model has caveats given that the error could not grow naturally at lateral boundary of the model; while coarse resolution global models often fails to reproduce the convective process, which is crucial to the error propagation process as discussed above. With advances in computational capability, the use of high-resolution convection-permitting models in near-hemispheric or even the global domain is becoming feasible in recent days (Mapes et al. 2008; Bretherton and Khairoutdinov 2015). As the ECMWF launches their new model cycle with highest-ever horizontal grid spacing of 9km, we are entering a new era in which global atmospheric models start to resolve the cumulus convection process. As an extension of previous studies, this study explores this 9km high-resolution ECMWF ensembles to study the intrinsic predictability of the synoptic-scale weather systems from a global perspective, with a focus on the error growth from convective to planetary scales.

Section 2 of this study introduces more details on the newly updated ECMWF model and the ensemble perturbations we adopted. Predictability results and the error saturation time is presented in section 3. Section 4 investigates further more on the propagation of the errors to better understand the dynamical process. Discussion and concluding remarks are given in section 5 and section 6, respectively.

4.2 Methodology

4.2.a Model

The results presented herein explores the most recent upgrade (cycle 41r2) of ECMWF, the highest-resolution (~9km) ever global operational model. More details of this model upgrade can be found on the official website of ECMWF

(http://www.ecmwf.int/search/elibrary/part?solrsort=sort_label%20asc&title=part&secondary_titl e=41r1&f[0]=ts_biblio_year%3A2016). Different from previous versions, this new ECMWF model implements a cubic octahedral reduced Gaussian grid (with spectral truncation denoted by $T_{CO}1279$) instead of the linear reduced Gaussian grid. With this cubic reduced Gaussian grid, the shortest resolved wave is represented by four rather than two grid points. The octahedral grid is also globally more uniform than the linear reduced Gaussian grid. In the vertical, ECMWF model has 137 levels. This corresponds to over 900 million grid points in total after this resolution upgrade. In addition to resolution increase, the realism of the kinetic energy spectrum is also significantly improved with more energy in the smaller scales due to a reduction of the diffusion and removal of the dealiasing filter, enabled by the change to using a cubic truncation for the spectral dynamics. The semi-Lagrangian departure point iterations used to solve the primitive equations are also increased in the new model to remove numerical instabilities. The integration time step upgraded accordingly to 450s.

Updated parameterization schemes that represents our comprehensive understanding of the physical processes are used in the model. Although running at convection-permitting 9km resolution, moist convection scheme evolved from Tiedtke (1989) is still used to better simulate the convective process. The clouds and microphysics are parametrized with a number of prognostic equations based on modification of Tiedtke (1993). The radiation scheme is the updated Rapid Radiation Transfer Model (RRTM, Mlawer et al., 1997; Iacono et al., 2008). The surface layer turbulence fluxes are computed based on the Monin–Obukhov similarity theory. Above the surface layer a K-diffusion turbulence closure is used to represent the turbulent diffusion process, except for unstable boundary layers where an Eddy-Diffusivity Mass-Flux (EDMF) framework is applied, to represent the non-local boundary layer eddy fluxes (Köhler et al., 2011). The land surface scheme is explained in Balsamo et al. (2009) and Balsamo et al. (2011). The effects of unresolved orography on the atmospheric flow are parametrized as a sink

of momentum (drag), based on the scheme in Beljaars et al. (2004). Non-orographic gravity wave drag parameterization proposed by Orr et al. (2010) is also adopted.

4.2.b Ctrl experiments and perturbations

For the ctrl experiment, we first run a 20-day integration initialized at 0000 UTC 26 December 2015 and extending to 0000 UTC 15 January 2016. This experiment is run as a historical re-forecast where the ECMWF reanalysis fields at the initial time of the integration is used for the initial condition. This time period is quasi-randomly picked as a winter case after ECMWF finished their ~9km resolution update. No "forecast bust" is found during this period (Lillo and Parsons 2016). To reduce case dependence of this study, we also run two additional 20-day integrations initialized from 0000 UTC 25 December 2015 and 0000 UTC 24 December 2015, respectively. All these three experiments give very similar results regarding their error growth behavior. We will focus on the 0000 UTC 26 December case unless otherwise specified.

Ensemble perturbation fields are added to the initial conditions of the ctrl experiments to study the error growth behavior. For each ctrl experiment, two sets of perturbations are added. The first set of perturbations is derived from the operational Ensemble of Data Assimilations (Iaslsen et al., 2010) of ECMWF, representing our current operational uncertainty for the initial condition. We note hereafter these perturbed runs as EDA. To explore the intrinsic predictability of the weather systems, the second set of perturbations is the same as the first set, except that their amplitudes are reduced to 10% of their original values, noted as 0.1EDA. 10 perturbed runs are conducted for each set of perturbations.

As intrinsic predictability implies the upper limit for our weather prediction given the nearly perfect model, no perturbation is applied to any model parameter and no stochastic physics scheme is adopted.

4.3 Growth and saturation of the error

4.3.a Short-term error growth

The short-term evolution of the errors in 0.1EDA is very consistent with the error growth model proposed by Zhang et al. (2007). Figure 4-1 shows snapshots of the ensemble spread of 500 hpa meridional wind (shading) in 0.1EDA for the first 3 days. The ensemble spread, as illustrative of the errors, shows up in the convectively active regions first. The spread then develops quickly in terms of amplitude and evolves along with the convective system. In the meantime, the spread also extends both upstream and downstream of the convective system, increasing its spatial scale. Three days after the initial minute perturbation is added, the error spreads almost across the whole globe instead of be localized in the convective area initially.

A similar picture can also be found from analysis of the kinetic energy spectrum of the perturbation. The kinetic energy spectrum is calculated as in Skamarock (2004) and Durran et al. (2013). We have chosen to compute 1D spectrum of the velocity fields along the east-west coordinates of the model grid points. Let $u_{i,j,n}$ and $v_{i,j,n}$ denote the zonal and meridional velocity components for the nth ensemble member, subtracting the ensemble mean fields first if we are calculating the kinetic energy spectra for the perturbations. The Fourier transforms of the velocity components $\hat{u}_{j,n}(k)$ and $\hat{v}_{j,n}(k)$ are then computed along zonal direction for each ensemble member and all the meridional j indices. Then the kinetic energy spectra density can be written as:

$$E_{j,n}(k) = \frac{\Delta x}{2N_x}\left[\hat{u}_{j,n}(k)\hat{u}^*_{j,n}(k) + \hat{v}_{j,n}(k)\hat{v}^*_{j,n}(k)\right] \tag{4.1}$$

where N_x is the number of grid points along the east-west direction in the model. The asterisk denotes the complex conjugate. We can then average $E_{j,n}(k)$ over j and n to get the kinetic energy spectrum for the full ensemble and the latitude band of interest. One advantage of

this method is that we could fully utilize the periodicity of the global model in the east-west direction without further processing the data. Figure 4-2 shows the kinetic energy spectra for the perturbations at 500 hpa averaged over the $40^{o}N \sim 60^{o}N$ in the 0.1EDA every 12 hours after the initial minute perturbations are added. We could see that the evolution of the perturbation kinetic energy spectrum in the first 3 days resembles previous result in regional model (Selz and Craig 2015, their Fig. 4). Note here the power spectrum of the perturbation seems to grow at all the scales simultaneously. This does not invalid the hypothesis proposed by Zhang et al. (2007). Recall that the spectral decomposition of a Gaussian function with small characteristic scale results in another Gaussian function centered at wavenumber $k = 0$, the largest scale. Thus, the growth of the large-scale error is mainly due to the projection of isolated feature of convective systems, as described in Selz and Craig (2015). The initial growth rate of the errors at all scales is also much higher than expected value of the synoptic-scale dynamics, further implying the increase of the power spectrum at large-scale is mainly due to error growth in the convective region.

Figure 4-2 also plots the kinetic energy spectrum for the initial perturbation in EDA as the reference line. Since the perturbations in EDA are derived from ensemble of data assimilation systems with grid spacing ~18km, the reference line has weaker small-scale (<100km) signals compared with the perturbations in our 9km run. From comparison of the kinetic spectrum, we know that it takes a little bit longer than 3 days for the initially minute perturbations in 0.1EDA to catch up the initial perturbations in EDA. This has important implications. As our model will never be perfect and that we may never reach an initial condition uncertainty as small as in the 0.1EDA, three days may serve as the upper limit for us to further extend our current operational deterministic forecast.

4.3.b Medium range error growth and error saturation

We have shown that, after ~3 days, the minute initial perturbation in 0.1EDA will grow to an amplitude that is comparable to our current operational initial condition uncertainty. Yet, the errors developed from this cascade-like mechanism might have different physical structure with initial perturbations in EDA (our operational forecast system). Hence the medium-term growth of the perturbations in 0.1EDA need to be investigated to further verify our notion of the 3 day predictability gap.

Figure 4-3 shows the time evolution of the ensemble variance of 500 hpa horizontal winds for both EDA and 0.1EDA experiments. We can see that the growth of the ensemble spread in 0.1EDA resembles the error growth of errors in EDA except that it is delayed for 3-4 days. This result confirms our findings. According to this diagram, our 6-day forecast in the future might be as good as our current 3-day forecast through reducing the initial condition error, which means there are still quite some room for improvement of our weather forecast. However, since the error growth rate decrease with time, we get diminishing returns through reducing the initial condition errors (Sun and Zhang 2016).

Figure 4-3 also shows that errors in the 0.1EDA grow quasi-exponentially in the medium range (day 3 - day 8), consistent with quasi-exponentially growth in the first few days of the EDA experiment under baroclinicity. An estimated error doubling time of 2.4 days could be calculated if we fit a line for the exponential growth during day 0 to day 5 in the EDA experiment (or day3 to day 8 in the 0.1EDA experiment). This value agrees well with the estimate done by Lorenz (1982) using a totally different method. After day 5 (day 8) in the EDA (0.1EDA) experiment, as the errors grow to a large amplitude, the exponential growth of the error begins to slow down. We can tell that after day 10 (day 14) in the EDA (0.1 EDA) experiment, the errors appear to saturate. The increase of the variance is negligible after. The saturation of the error represents that the

amplitude of the error reaches that of the background fluid. As different members of the ensemble could give completely different weather scenario, our numerical weather forecast cannot provide any useful information after day 10 (day 14) in the EDA (0.1EDA) experiment.

We can also examine the growth of the perturbations at each different scale by calculating the perturbation kinetic energy spectrum based on Equation 1. Figure 4-4 plots the evolution of the perturbation kinetic energy spectrum in EDA and 0.1EDA experiments. Consistent with our previous findings, after 3 days the errors in 0.1EDA grows to similar amplitudes with the initial condition error in the EDA experiment (grey dot line in Fig. 4-4). The kinetic energy spectrum of the background flow averaged over this 20-day integration period is also plotted (black dot line), representing the saturation level of the errors at different scales. Once again, we find that after 15 days of integration, the errors in the 0.1EDA experiment saturates at all scales with wavelengths smaller than 5000 km, implying the ultimate limit for the prediction of synoptic-scale weather systems. It's also noted that the saturation time decreases with decreasing horizontal scales. For example, it only takes roughly one week for the error in 0.1EDA to saturate at a scale of 1000 km. In the EDA experiment, the time reduced to 3 or 4 days due to the predictability gap induced by larger initial condition error. This partially explains why our current medium-range weather forecast suffers for some systems; our initial condition is simply not good enough to produce meaningful 5 day forecasts for any system that has a characteristic scale smaller than 1000 km. This result is also supported by many previous case studies. Munsell and Zhang (2014) investigated the ensemble forecast for the mid-latitude landfall of tropical cyclone Sandy (2012) and found that the divergence of the track at longer lead times (4-5 days) could be attributed to the uncertainties in the environmental steering flow of the initial fields. As for mesoscale, the predictability time scale gets much shorter, Durran et al. (2013) suggested that uncertainties in the initial conditions could lead to ensemble spread becomes large enough to include both many members likely to produce rain and many likely to produce snow in 36 h.

The loss of predictability may be better illustrated by the physical fields. Figure 4-5 shows the evolution of the large-scale vorticity (filtered with wavelength > 1500 km) at 850 hpa for different ensemble members. This field is often used for tracking the movement of the synoptic storms in previous studies (e.g., Chen et al. 2014). At day 3, the differences between different members mainly shows up in small and meso-scale (Fig 1c, Fig. 5a), the large-scale vorticity center (storm location) is almost identical for all the members and the size for each storm (storm intensity) is also the same among different members. Notable differences can be found at day 6 as the errors grow with time. At day 9, different evolutions of storms in different members become significant. Storm in one ensemble member may split into two smaller centers while the same storm in another ensemble member get intensified. Figure 4-6 also plots the 12-hour accumulated precipitation at day 9 for different ensemble members in 0.1EDA. we can see that the precipitating region varies dramatically between different members though two main precipitating band can be identified. For the same region off the southeast coast of America (red box), 12h precipitation change from 0 (no precipitation) to 50mm, nearly the maximum value for the whole mid-latitude band during the same period. At day 12, the locations of the storms become quasi-chaotic. There is a large spread of the storms within the storm track region. It's becoming really hard to get any useful forecast out of this quasi-randomly distribution of the storms. At day 15, the distribution of storms among different members are really chaotic, we have reached the upper predictability limit for weather systems.

However, after day 15 (saturation time for the synoptic eddies), slow growth of the error at planetary-wave scale (wavelength > 10000km) still can be found (Fig. 4-4). The error growth at the planetary-wave scale after 15 days implies possible interactions between synoptic eddies and the quasi-stationary planetary Rossby waves. Different realizations of the synoptic-scale storms in different members will feedback to larger scale, leading to slightly different planetary waves for different ensembles. The ensemble mean result after 20-day integration resembles the monthly

mean fields during the simulation period (Fig. 4-7). These quasi-stationary signals provide theoretical bases for long-term sub-seasonal and seasonal forecast, which is beyond the scope of this study.

4.4 Error propagation and associated dynamical processes

We have demonstrated the predictability gap between our current operational weather forecast and the theoretical upper limit for the mid-latitude synoptic systems in previous section. It is helpful to understand more of the physical processes behind error growth so that we might be able to reduce the predictability gap and help improve our operational forecast.

As we discussed earlier (Fig. 4-1), the short-term error growth in 0.1 EDA largely resembles the conceptual model proposed by Zhang et al. (2007). There has been lots of discussion on this process in earlier studies (e.g., Sun and Zhang 2016, Selz and Craig 2015). We do not plan to go further into details here. The error growth of during this period is due to chaotic nature of the convective systems, and there is little we could do about that. For those small-scale phenomena with short intrinsic predictability limit, the best way is to give probability forecast using multi-physics or even multi-model ensembles to acknowledge our forecast uncertainties.

However, luckily or not, our initial condition estimate currently is still not good enough for us to worry about the impact of the upscale error growth to operational synoptic scale weather forecast. Given the 2.4-days error doubling time estimated in previous section, even if we could reduce our initial condition error to half of its current value, the exponential growth of the error will need 2.4 days to gain its amplitude back, which is shorter compared to the ~3 day predictability gap we found earlier. Thus, the baroclinic growth of the error will continue dominate until our initial condition error is reduced slightly less than half of its current value.

Hence, in order to improve our current operational forecast, it's important to know when and where should we reduce our initial condition error (Majumdar et al. 2016). Figure 4-8 is the hovmöller diagram for the ensemble spread of meridional wind at 500 hpa in the 0.1EDA experiment. For the first few days, as described earlier, errors show up in precipitating regions (such as convective systmes around 170W and 30W) and then evolve along with the convective systems. The propagation of the error initially reflects the movement of the synoptic storms, with a speed close to 15m/s (black dash line in Fig. 4-8). However, in the medium range (3-10 days) when the error growth is dominated by baroclinic instability, errors seem to be able to propagate at higher speed close to 30m/s as indicated by the red dash line, implying possible downstream development.

The downstream development of the error can be better illustrated by comparing the evolution of the errors with the movement of the storms. Figure 4-9 shows the spatial distribution of the ensemble spread in the medium range (5-7 days) in 0.1EDA. The large-scale vorticity at 850 hpa for two different members are also plotted to represent the evolution of the synoptic storms. At day 5, the largest error in the mid-latitude is associated with a weakening convective storm at 140W (Fig. 4-9a). This storm then dissipates at day 6, although the dissipation process differs within different members (Fig. 4-9b). The ensemble spread also has a maximum at the dissipation region. At day 7, after the old storm dies, a new storm develops in central US region, with a large ensemble uncertainty. Hence, instead of moving with the convective system at the phase speed, the propagation of the forecast error (ensemble spread) is rather linked to the energy propagation of the storm, transported from dying storm to the newly developed ones downstream. It has been well known that downstream radiation of energy through the ageostrophic geopotential fluxes is important for the development and maintenance of eddy activity (Chang and Orlanski 1993). The calculated group velocity of the synoptic eddies is also close to 30m/s (Chang et al. 2002), consistent with our hovmöller diagram for the error propagation here. Need

to note here, the moist convection further increases the forecast error and ensemble uncertainty during this downstream development process. Strong moist convection in the central US create a "hotspot" of the error and fuel its further development (Fig. 9c). Given that error will propagate through several highly convectively unstable regions within our interested medium-range, moist convection could play a significant role in the development of and maintenance of error amplitude.

As discussed above, the fast propagation of the error in the medium range in 0.1EDA stems from the downstream development of the background storms. To further verify this, Fig. 4-10 plots the hovmöller diagram for the meridional wind at 300 hpa averaged over $40^o N \sim 60^o N$. Green contour indicates the region of precipitation, which generally agrees well with the positive (polarward) meridional wind. we can see that, for each ensemble member, successive downstream development of synoptic features could be identified between 150W to 0 as baroclinic wave packets (e.g., black line in Fig. 4-10a). However, as the errors between different members grow with time, these baroclinic wave packets may have different amplitude, initiation time, and life cycles among different members. Hence the ensemble mean fields does not have any wave packets after 9 days of integration (Fig. 4-10b).

The downstream propagation of the errors has lots of implications to our operational weather forecast. If we want to improve weather forecast for certain region, the flow upstream is as important as local environment at this local region, if not more so. In some cases, it's even the subsynoptic features upstream that lead to the forecast errors downstream (Lamberson et al. 2016). If we could make targeted observation upstream and reduce the initial condition error there, similar as the relaxation experiments in Linus et al. (2017), our operational medium-range forecast would improve significantly. The challenge is that the targeted sensitivity area varies depend on different cases.

4.5 Discussions

With all these almost identical experiments in 0.1EDA, one of our goals is trying to investigate the ultimate predictability of synoptic scale mid-latitude weather systems. We implicitly assume that the model is perfect when we use the error saturation time in the model to estimate the predictability time of the real atmosphere. While ECMWF is, arguably, the best operational model we have right now, 9km is still in the "gray zone" where convective updrafts are not well resolved. Given the importance of moist convection in the upscale error propagation process in short range and its possible resolution dependence found in other studies (Selz and Craig 2015), two additional runs using the next generation global prediction system (NGGPS) at 3 km is conducted.

The NGGPS adopts the finite volume cubed-sphere (FV3) dynamical core developed at GFDL, with updated GFS physics scheme. The two runs are integrated using exactly the same initial condition in the ctrl and ensemble member1 of 0.1EDA, respectively. Figure 4-11 shows the evolution of the perturbation kinetic energy spectrum. The perturbation here is defined as the differences between these two runs. The difference spectra will then equal 2 times the full background kinetic energy spectrum as expected for a complete phase decorrelation of the modes, especially on small scales. Other than this difference by definition, the 3km NGGPS model results show surprisingly consistence with the ECMWF model (Fig. 4-4). After ~3 days, the differences between these two nearly identical experiments grow to an amplitude comparable with the initial condition error of the EDA experiments. The saturation times of the errors at different scales also agree well with the 9km ECMWF model. Agreements between these two models with very different physics and resolutions further strengthen our confidence on previous conclusions. This also implies that both models capture the error growth process in our real

atmosphere and it is valid to use these models to estimate the theoretical upper limit for mid-latitude weather systems.

The appearing quasi-random choice of 10% for reducing the amplitude might cause concerns on the accuracy of the estimate for the ultimate predictability. However, as shown in Sun and Zhang (2016), forecast error due to rapid upscale growth from moist convection gets increasingly less sensitive to the scale and amplitude of the initial perturbations when the initial-error amplitude is getting smaller. 10% of our current initial condition error is already in the zone where very limited return could be gained from further reducing the perturbation. The "super-exponential" growth of the error in the first few hours in 0.1EDA (Fig. 3) also implies this point.

4.6 Concluding Remarks

Using updated 9km high-resolution operational global ensemble experiments, this study examines both the intrinsic and the practical predictability limit for mid-latitude weather systems. We do find that an intrinsic predictability limit of around 2 weeks exist for the synoptic-scale storms, which means our current operational weather forecast could at best extend 3-4 days beyond current practical 10 day limit.

The error growth process within our model for nearly perfect initial condition is illustrated in Fig. 12. Errors will first be confined in the precipitating regions and grow under convective instability. Then these errors spread from convective regions to larger-scale balanced fields after 2-3 days and start to grow exponentially via baroclinic instability. Correspondingly, the propagation of the error switch from moving with the convective storm to faster propagation at the group velocity of baroclinic waves. The exponential amplification of the error finally leads to its saturation at synoptic-scales after ~2 weeks. After 2 weeks, there is still some amplification of

the error at planetary scales, although really slowly, which means that the planetary quasi-stationary waves could be affected by the synoptic-scale eddies.

While we only conduct experiments for several different days, different cases show very good consistency (Fig. 4-3). Averaging over the whole mid-latitude band composed by lots of storms at the same time also helps reducing the case dependence in the study. Agreement between ECWMF and NGGPS model further strengthen our confidence on our results.

The 3-4 day predictability gap for the synoptic scale weather means that there are still plenty of room for the improvement of our weather forecast, which will bring significant socio-economic benefits. Achieving this additional predictability limit needs coordinated efforts by the entire community through reducing the initial condition error with better observations and better use of observations with advanced data assimilation and computing techniques. On the other hand, the predictability gap will decrease with decreasing scales, as the intrinsic predictability time decrease. Some meso-scale phenomena might have an intrinsic predictability time that's shorter than 3 days. For these meso-scale feathers, reducing the initial condition error does not significantly help our forecast given that their intrinsic predictability time is short. Instead, it's more important to reduce the systematic model error if there is one. Also, using multi-physics or stochastic physics scheme to better represent the forecast uncertainty is critical (Palmer 2017).

This study only focus on the mid-latitude here. The error growth process in the tropics would be very different. For one thing, there is no baroclinic instability in the tropics region. Hence, all the behavior after 3 days in this study does not apply to the tropics region. Large-scale phenomena in the tropical region also tend to have a period that's much longer than the mid-latitude (such as the MJO), implying potential longer predictability. Further research on this topic is ongoing and will be reported in the near future.

Chapter Figures
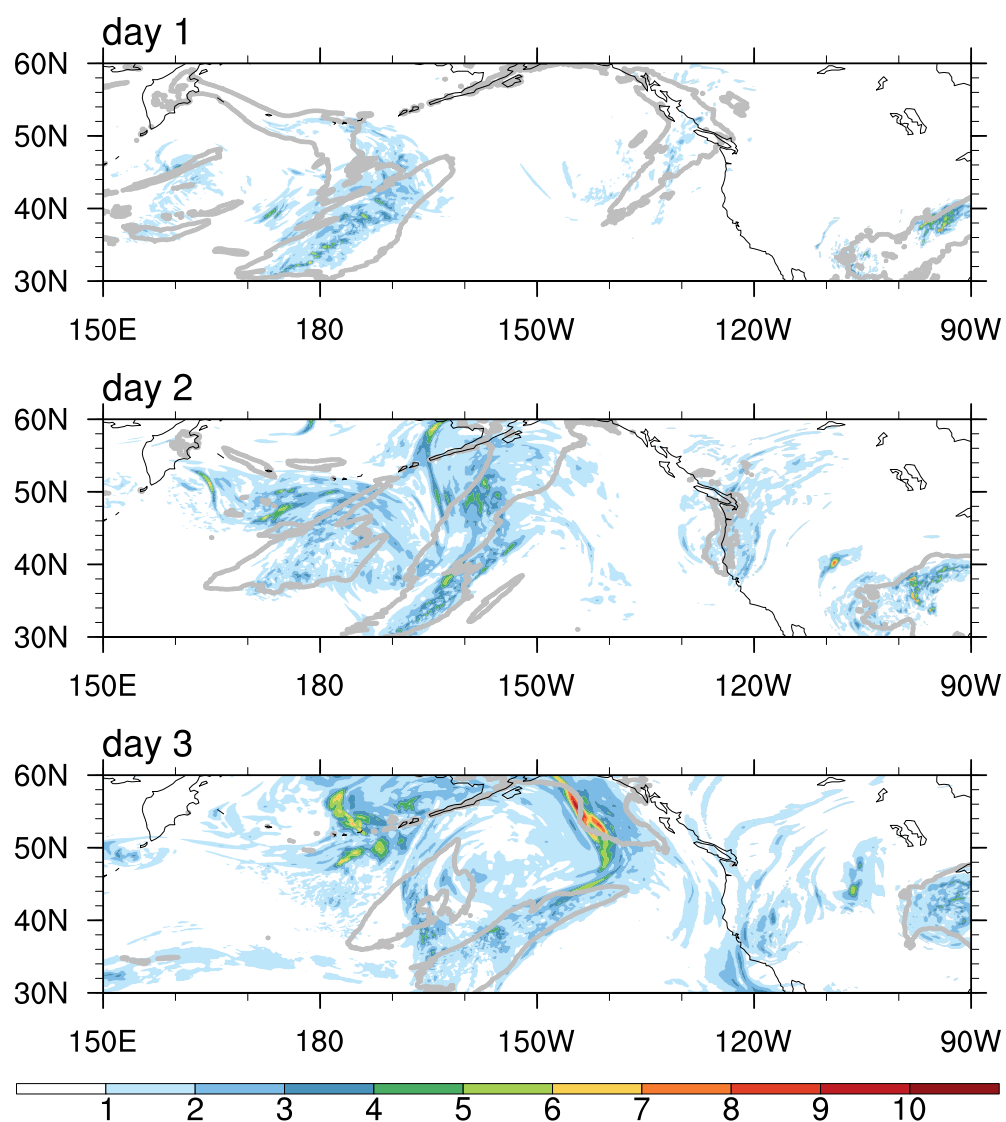
Figure **4-1**: snapshots of the ensemble spread of 500 hpa meridional wind (shading) in 0.1EDA for the first 3 days. Grey contour precipitating aera (24 h precipitation > 1mm).
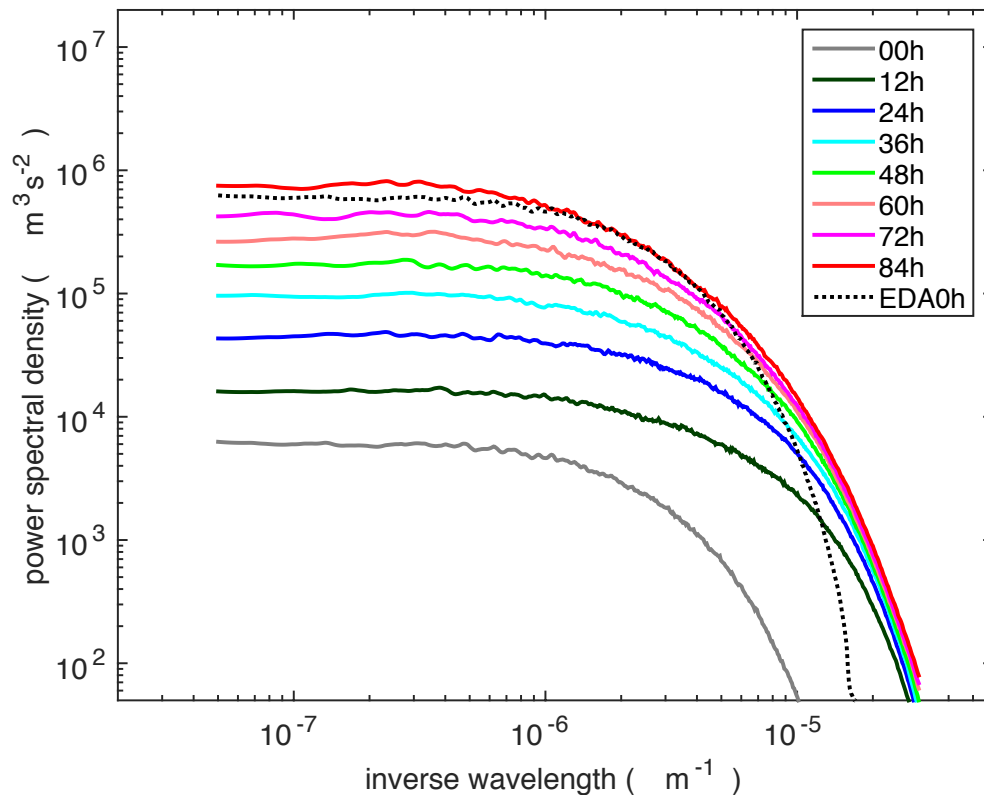
Figure **4-2**: Perturbation kinetic energy spectrum at 500 hpa averaged over the $40^oN \sim 60^oN$ latitude band in the 0.1EDA with an interval of 12 hours. Black dot line is the kinetic energy spectrum for the initial perturbation in EDA, representing our current initial condition uncertainty.
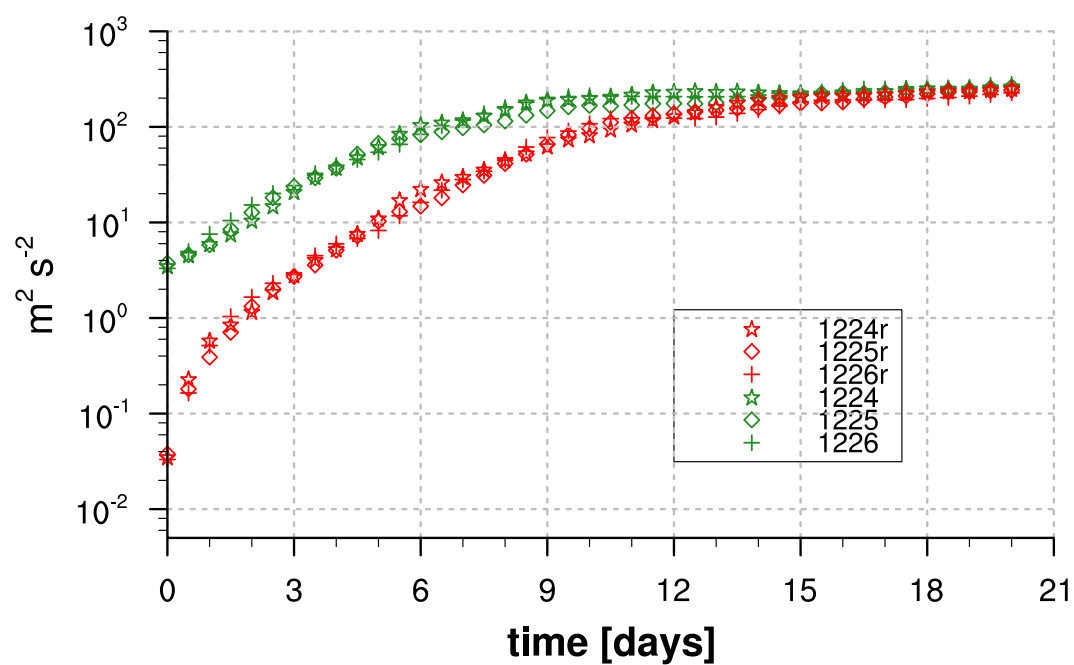
Figure **4-3**: Time evolution of the ensemble variance of 500 hpa horizontal winds for both EDA (green) and 0.1EDA (red) experiments. Different symbols represents cases with different initial time.
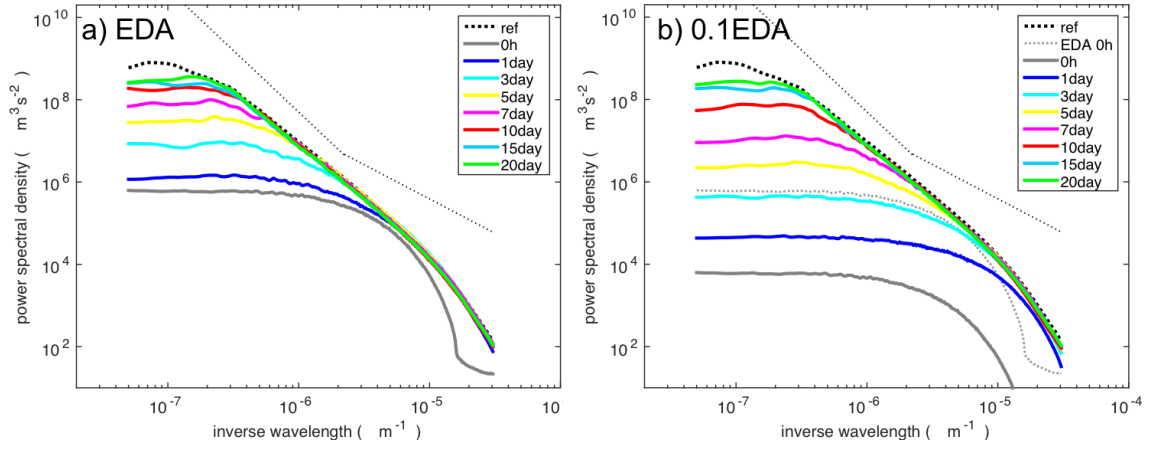
Figure **4-4**: Time evolution of the perturbation kinetic energy spectrum in **a)** EDA and **b)** 0.1EDA experiments similar as Figure 4-2. Black dot line is the kinetic energy spectrum of the background flow averaged over 20-day integration period, representing the saturation level.
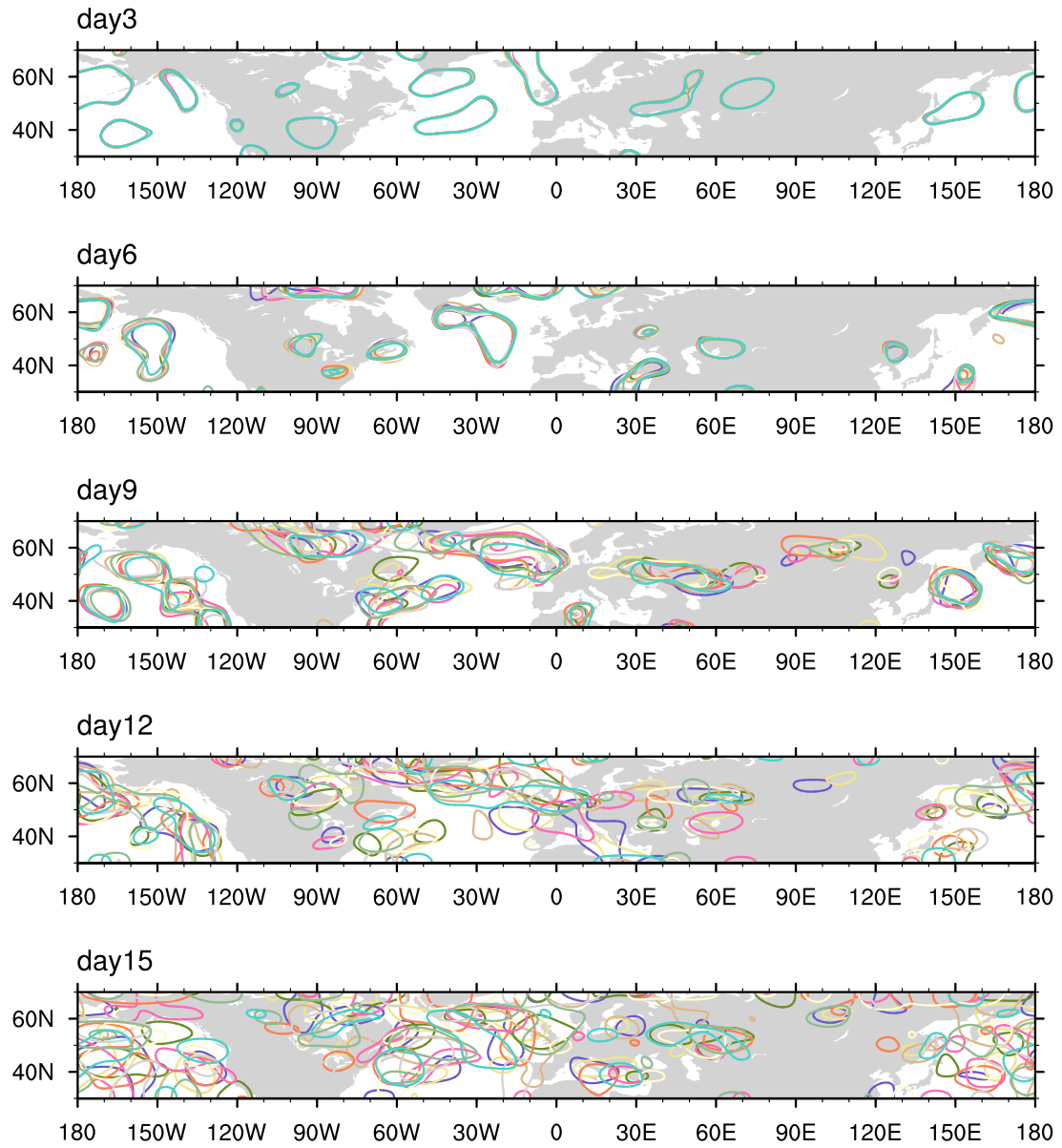
Figure **4-5**: The evolution of the large-scale vorticity (filtered with wavelength > 1500 km) at 850 hpa for different ensemble members. Contour value is $\zeta = 2e\text{-}5$ here. Different color means different ensemble member.
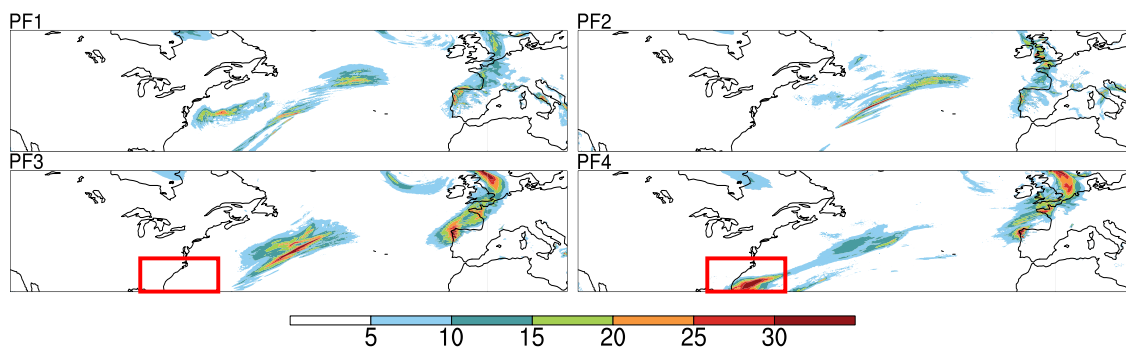
Figure **4-6**: Distribution of 12 h precipitation for the first four members in 0.1EDA after 9 days.
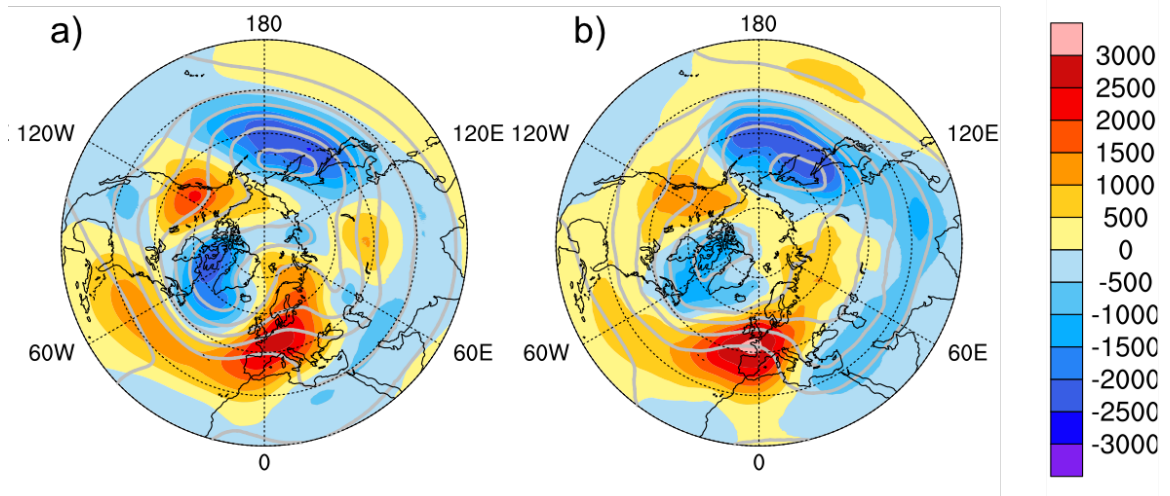
Figure **4-7**: Geopotential anomaly (shading, unit: $m^2\ s^{-2}$) for **a)** monthly (from Dec 20th 2015 to Jan 19th 2016) averaged fields over integration period, **b)** 10-member ensemble mean fields after 20-day integration in 0.1EDA.
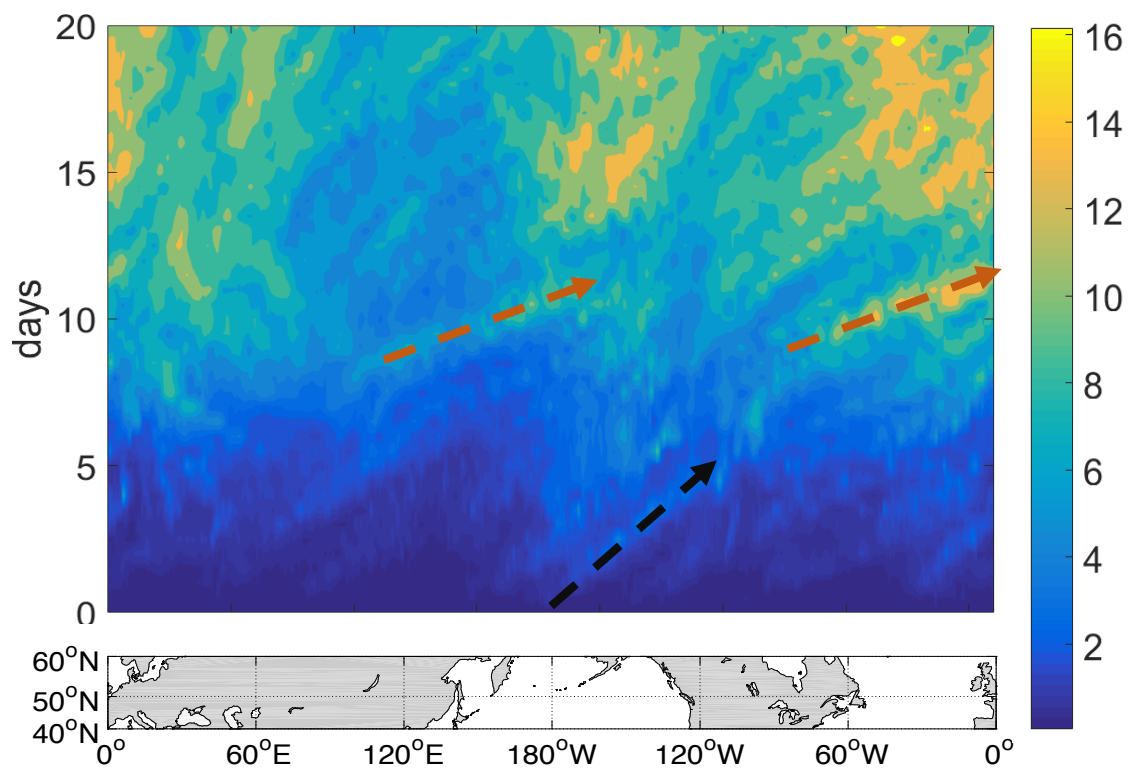
Figure **4-8**: Hovmöller diagram for the ensemble spread of meridional wind at 500 hpa in the 0.1EDA experiments.

day5

day6

day7
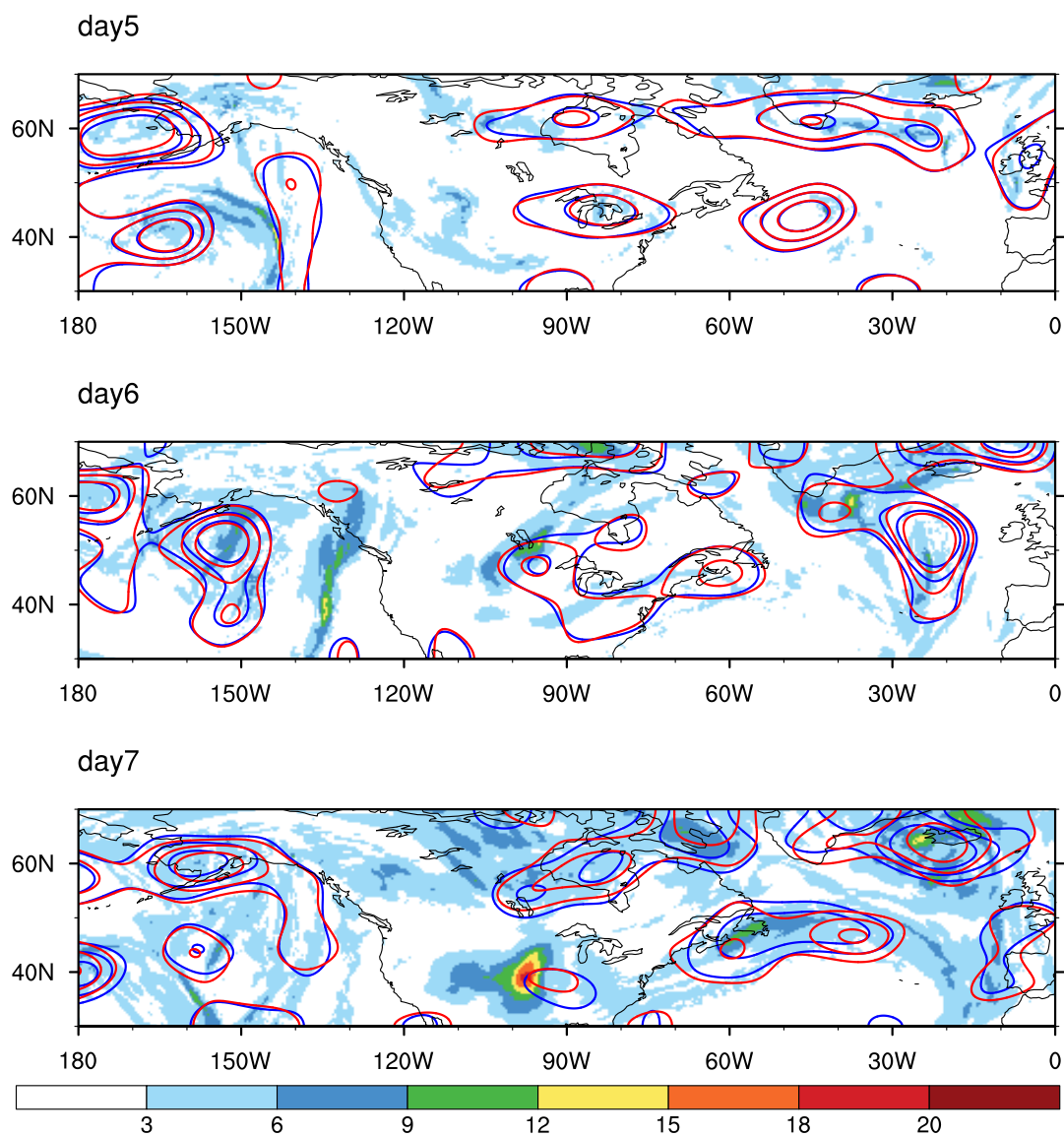
Figure **4-9**: The spatial distribution of the ensemble spread (shading) in the medium range (5-7 days) in 0.1EDA experiments. Contours are large-scale vorticity at 850 hpa for two different members.
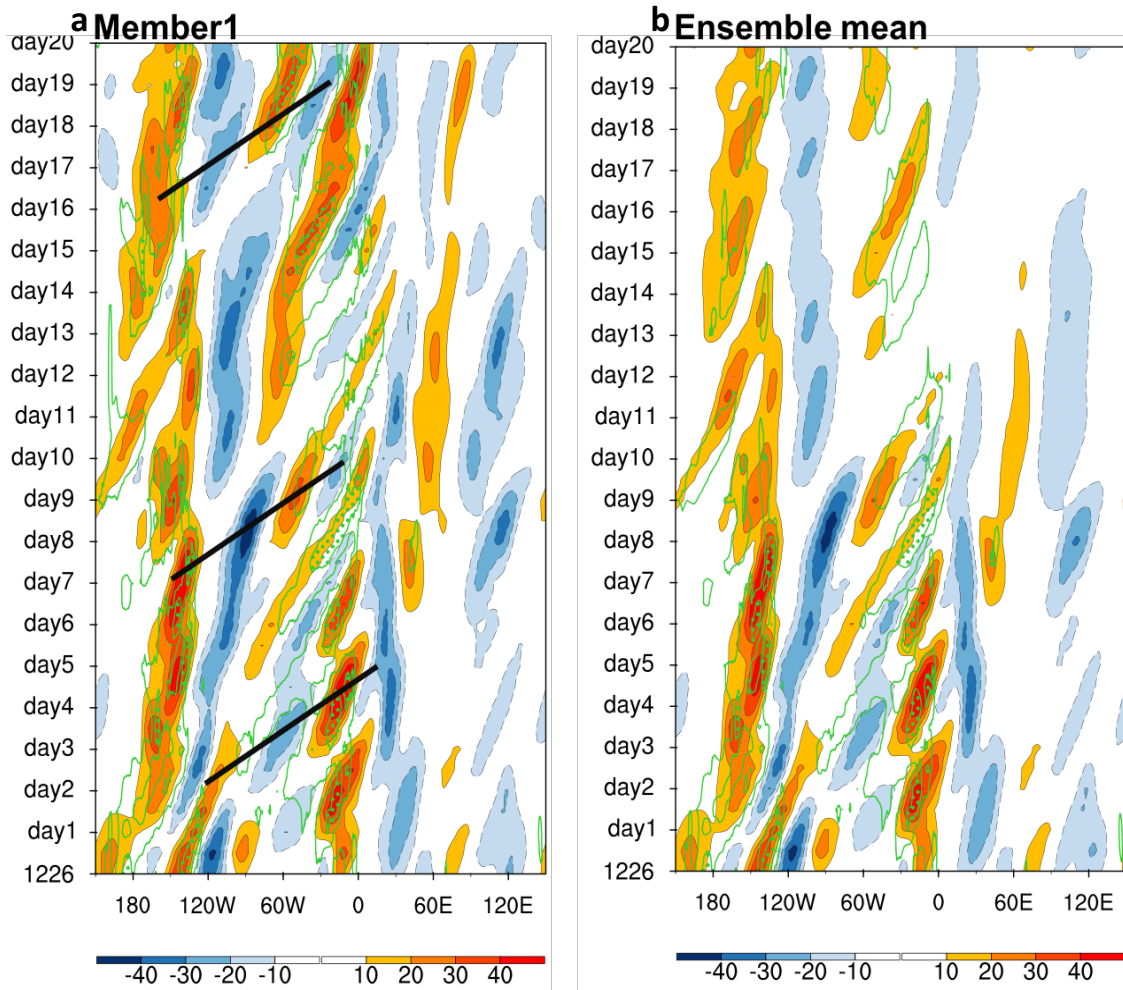
Figure **4-10**: The hovmöller diagram of the meridional winds at 300 hpa averaged over $40^oN \sim 60^oN$ latitude band for **a)** one member, **b)** ensemble mean fields. Green contour indicates the region of precipitation.
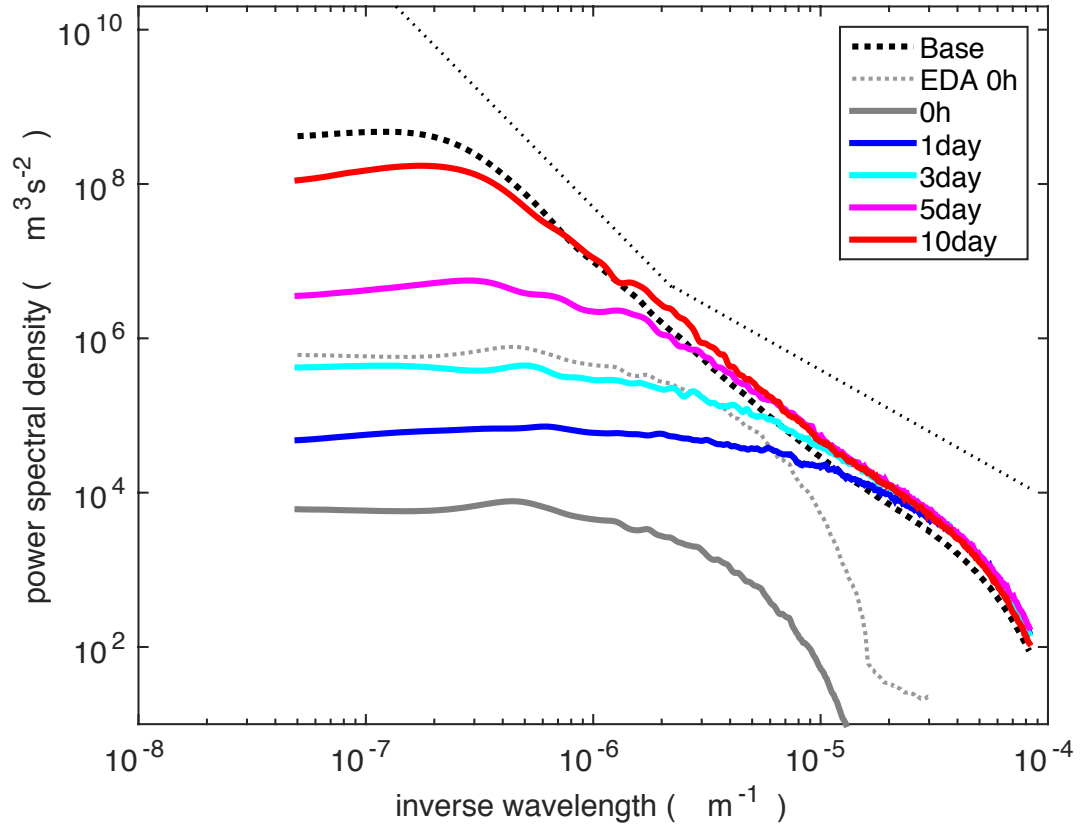
Figure **4-11**: Time evolution of difference spectra for 500 hpa horizontal winds similar as Figure 4-2, except for the 3km NGGPS FV3 experiment. The difference spectra are smoothed using 1-2-1 smoothing method.
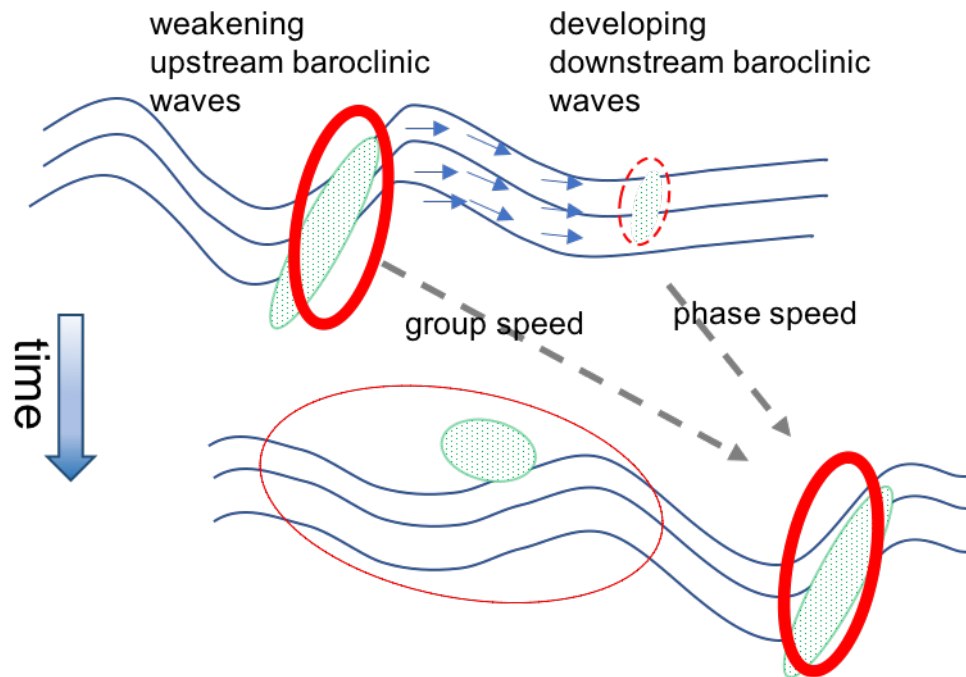
Figure **4-12**: Schematic picture of error growth and transport in mid-latitude weather systems. The thin solid lines represent height contours (decreasing toward the top). Green dotted area represents the precipitation region. Red circle represents the error maximum (width implies the amplitude). The vectors respresent the energy (error) flux.

Chapter 5

Summary and Future Work

5.1 Summary

In his pioneering 1963 publication Deterministic Nonperiodic Flow, Lorenz concluded the atmosphere may have an inevitable limit to predictability, stating:

"... [atmospheric] prediction of the sufficiently distant future is impossible by any method, unless the present conditions are known exactly. In view of the inevitable inaccuracy and incompleteness of weather observations, precise very-long range forecasting would seem to be non-existent".

This thesis, while following Lorenz's idea, examines the intrinsic and practical predictability of our real atmosphere using the most comprehensive model we have right now. The main contribution of this thesis is two-fold. First, the underlying dynamics that govern the upscale error growth in the atmosphere is studied and the role of moisture is emphasized (chapters 2, 3). Second, the intrinsic and practical predictability time is estimated for the synoptic-scale weather systems (chapter 4). The main findings of our thesis will be summarized in more detail in the following.

In the dry experiment free of moist convection, error growth is controlled primarily by baroclinic instability under which forecast accuracy is inversely proportional to the amplitude of the baroclinically unstable initial-condition error (thus the prediction can be continuously improved without limit through reducing the initial error). Under the moist environment with strong convective instability, rapid upscale growth from moist convection leads to the forecast error being increasingly less sensitive to the scale and amplitude of the initial perturbations when

the initial-error amplitude is getting smaller; these diminishing returns may ultimately impose a finite-time barrier to the forecast accuracy (limit of intrinsic predictability and the so-called "butterfly effect"). However, if the initial perturbation is sufficiently large in scale and amplitude (as for most current-day operational models), the baroclinic growth of large-scale finite-amplitude initial error will control the forecast accuracy for both dry and moist baroclinic waves; forecast accuracy can be improved (thus the limit of practical predictability can be extended) through the reduction of initial-condition errors, especially those at larger scales.

Regardless of the initial-perturbation scales and amplitude, the error spectrum will adjust toward the slope of the background flow. Inclusion of strong moist convection changes the mesoscale kinetic energy spectrum slope from −3 to ∼−5/3. This change further highlights the importance of convection and the relevance of the butterfly effect to both the intrinsic and practical limits of atmospheric predictability, especially at meso- and convective scales. This shallow -5/3 slope can be identified at almost all height levels from the lower troposphere to the lower stratosphere in our simulations of an idealized convective system, implying a strong connection between different vertical levels. Our chapter 3 also computes the spectral kinetic energy budget for these simulations to further analyze the processes associated with the creation of the spectrum. The buoyancy production generated by moist convection, while mainly injecting energy in the upper troposphere at small scales, could also contribute at larger scales, possibly as a result of the organization of convective cells into mesoscale convective systems. This latter injected energy is then transported by energy fluxes (due to gravity waves and/or convection) both upward and downward. Nonlinear interactions, associated with the velocity advection term, finally help build the approximate −5/3 slope through upscale and/or downscale propagation at all levels.

Through high-resolution deterministic and ensemble sensitivity experiments with state-of-the-science global numerical weather prediction models using respectively both realistic, large

and hypothetical, minute initial perturbation uncertainties, we estimated the ultimate predictability limit of mid-latitude day-to-day weather phenomena such as mid-latitude winter storms and summer monsoonal rainstorms. Such a limit is intrinsic to the underlying dynamical system and instabilities even if the forecast model and the initial conditions are nearly perfect. Minute uncontrollable initial conditions originated from convective and mesoscale instabilities can grow upscale that will eventually limit the predictability of various weather at increasingly larger scales. More specifically, from a global perspective, on average, the practical predictability limit of the midlatitude weather by the current state-of- the-science global models from lead numerical weather prediction centers is about 10 days while the ultimate intrinsic limit is likely to be within 2 weeks. In other words, even with a perfect model, reducing the initial condition uncertainties to an order of magnitude smaller than the realistic current level of uncertainty will at most extend the deterministic forecast lead times by 3-4 days for midlatitude day-to-day synoptic weather; much smaller room in improving the forecast lead times will be for smaller scale phenomena. For the mesoscales within 500 km, the global average limit will be within a couple of days, even shorter limit for convective storms. Nevertheless, this 3-4 more days of predictive potential for global synoptic day-to- day weather remains an encouraging and impactful goal to be achieved that will bring significant socioeconomic benefits. Achieving this additional predictability limit needs coordinated efforts by the entire community through designing better numerical models performing at higher resolutions, with better observations, and through better use of observations with advanced data assimilation and computing techniques.

5.2 Future work

This thesis only focus on the mid-latitude here. The error growth process in the tropics would be very different. For one thing, there is no baroclinic instability in the tropics region.

Hence, baroclinic error growth, which is the key factor of mid-latitude error saturation time, does not apply to the tropics region. Large-scale phenomena in the tropical region also tend to have a period that's much longer than the mid-latitude (such as the MJO), implying potential longer predictability. Given we are using global model (chapter 4), the methodology we used could be easily extend to the tropics, research on this topic is ongoing and will be reported in the near future.

For the scale interaction part, we mainly focus on the small to meso-scales in this thesis, where the upscale error growth process is most evident. Yet we have implied that synoptic eddies could also affect the planetary scale waves in chapter 4. It is also well known that the stationary waves have a strong control over the distribution of the synoptic storms. Utilizing the global simulation, the scale interaction on the large-scale end of the atmosphere and the decomposition used in chapter 3 could be easily applied to a global framework, although longer time simulation might be necessary, which mean more computational cost.

Appendix A

Initial moisture field of baroclinic wave simulations in chapter 2

The initial moisture field in our model setup is based on Tan et al. 2004, with only slightly modification. The x-independent relative humidity profile for the MOIST case is given by

$$RH(y,z) = RH_0 R(y) \begin{cases} 1 - 0.9\left(\dfrac{z}{z_{rh}}\right)^{\delta} & z < z_{rh}, \\ 0.1 & z \geq z_{rh}, \end{cases} \tag{A1}$$

$$R(y) = \begin{cases} R_1, & y \leq y_1 \\ R_1 + \dfrac{y - y_1}{y - y_2}(R_2 - R_1), & y_1 < y < y_2 \\ R_2, & y \geq y_2 \end{cases} \tag{A2}$$

where $RH_0 = 75$, $R_2 = 1$, $R_1 = 0.66$, $y_1 = 0.4y_c$, $y_2 = 0.9y_c$, $y_c = 4000\,km$, $z_{rh} = 8000\,km$, and $\delta = 1.25$.

For the **RH50** case, the relative humidity is further reduced to half of its initial value.

Appendix B

DKE budget equation for different scale

The derivation of the DKE budget equation is adapted from Zhang et al. (2007) and Peng et al. (2014). As in Zhang et al. (2007), the difference momentum equations can be written as

$$\frac{\partial \delta u}{\partial t} = -\delta \left(\mathbf{u} \cdot \nabla_h u + w \frac{\partial u}{\partial z} \right) - \delta \left(\frac{1}{\rho} \frac{\partial p'}{\partial x} \right) + f \delta v + \delta D_u \qquad \text{(B1)}$$

$$\frac{\partial \delta v}{\partial t} = -\delta \left(\mathbf{u} \cdot \nabla_h v + w \frac{\partial v}{\partial z} \right) - \delta \left(\frac{1}{\rho} \frac{\partial p'}{\partial y} \right) - f \delta u + \delta D_v \qquad \text{(B2)}$$

Note δD terms include not only the diffusion, but also the large scale damping effect due to planetary boundary layer scheme and the Rayleigh damping effect at the model top.

Multiply Eqns B1 and B2 by $\overline{\rho} \delta u$ and $\overline{\rho} \delta v$ respectively, then take the sum of these two eqns, we get

$$\frac{\partial}{\partial t}(DKE) = \left[-\bar{\rho}(\delta u)\delta \left(\boldsymbol{u} \cdot \boldsymbol{\nabla_h} u + w \frac{\partial u}{\partial z} \right) - \bar{\rho}(\delta v)\delta \left(\boldsymbol{u} \cdot \boldsymbol{\nabla_h} v + w \frac{\partial v}{\partial z} \right) \right]$$

$$+ \left[-\bar{\rho}(\delta u)\delta \left(\frac{1}{\rho} \frac{\partial p'}{\partial x} \right) - \overline{\rho(\delta v)\delta \left(\frac{1}{\rho} \frac{\partial p'}{\partial y} \right)} \right] + \mathcal{Damping} \qquad \text{(B3)}$$

here DKE is defined as $DKE = \frac{1}{2}\overline{\rho}\left[(\delta u)^2 + (\delta v)^2 \right]$.

In our analysis, we separate the budget into three different scale ranges (large scale or L, wavelength > 1000 km; intermediate scale or M, 1000 km > wavelength > 200

km; small scale or, wavelength < 200 km). Since the DKE budget equations for different scales are similar, here we only show the derivations for the large scale (L) budget equation.

Use a large scale filter for each term in B1) and B2), we have

$$\frac{\partial(\delta u)_L}{\partial t} = -\delta\left(\mathbf{u}\cdot\nabla_h u + w\frac{\partial u}{\partial z}\right)_L - \delta\left(\frac{1}{\rho}\frac{\partial p'}{\partial x}\right)_L + f(\delta v)_L + \delta(D_u)_L \quad \text{(B4)}$$

$$\frac{\partial(\delta v)_L}{\partial t} = -\delta\left(\mathbf{u}\cdot\nabla_h v + w\frac{\partial v}{\partial z}\right)_L - \delta\left(\frac{1}{\rho}\frac{\partial p'}{\partial y}\right)_L - f(\delta u)_L + \delta(D_v)_L \quad \text{(B5)}$$

Again, Multiplying Equations B4 and B5 by $\overline{\rho}(\delta u)_L$ and $\overline{\rho}(\delta v)_L$ respectively, we get the budget equation for Large scale DKE, Equation 3) in the text;

$$\frac{\partial}{\partial t}(DKE)_L = \left[-\bar{\rho}(\delta u)_L\delta\left(\boldsymbol{u}\cdot\boldsymbol{\nabla_h}u + w\frac{\partial u}{\partial z}\right)_L - \bar{\rho}(\delta v)_L\delta\left(\boldsymbol{u}\cdot\boldsymbol{\nabla_h}v + w\frac{\partial v}{\partial z}\right)_L\right]$$

$$+ \left[-\bar{\rho}(\delta u)_L\delta\left(\frac{1}{\rho}\frac{\partial p'}{\partial x}\right)_L - \bar{\rho}(\delta v)_L\delta\left(\frac{1}{\rho}\frac{\partial p'}{\partial y}\right)_L\right]$$

$$+ (Damping)_L \qquad \text{B6)}$$

Note here $(DKE)_L$ is defined as in $(DKE)_L = \frac{1}{2}\overline{\rho}\left[(\delta u)_L^2 + (\delta v)_L^2\right]$.

Appendix C

Decomposition of the pressure term in the DKE budget equation

C. 1: cross-scale contribution of the pressure term

Unlike the nonlinear advection term, the pressure term in the budget equation derived above does not have a contribution across the scale ranges. The proof is listed below. We can divide the density into two parts (mean and perturbation), $\rho = \bar{\rho} + \rho'$, assuming $\rho' << \bar{\rho}$, then

$$\delta\left(\frac{1}{\rho}\frac{\partial p'}{\partial x}\right) \sim \delta\left(\frac{1}{\bar{\rho}}\frac{\partial p'}{\partial x}\right) \sim \frac{1}{\bar{\rho}}\frac{\partial(\delta p')}{\partial x} \qquad \text{C1)}$$

The first part of the pressure term then becomes

$$-\bar{\rho}\delta u \delta\left(\frac{1}{\rho}\frac{\partial p'}{\partial x}\right) \sim -\bar{\rho}\delta u \frac{1}{\bar{\rho}}\frac{\partial(\delta p')}{\partial x} = \delta u\frac{\partial(\delta p')}{\partial x} = \delta u \delta\left(\frac{\partial p'}{\partial x}\right) \qquad \text{C2)}$$

Thus, the cross-scale contribution of the pressure term should be

$$-\bar{\rho}(\delta u)_l \, \delta\left(\frac{1}{\rho}\frac{\partial p'}{\partial x}\right)_m \sim (\delta u)_l \, \delta\left(\frac{\partial p'}{\partial x}\right)_m \rightarrow A\sin(lx)B\sin(mx) \qquad \text{C3)}$$

where l and m represent different wavenumbers, A and B are the amplitudes. Note that we need to integrate the pressure term over the whole domain to consider its total contribution. According to the orthogonality of the Fourier expansion, the integration equals zero, which means that the pressure term does not have any cross-scale contribution. The nonlinear advection term is the only term that is responsible for the redistribution of the energy across different scales.

C. 2: Decomposition of the pressure term

The pressure term can be further decomposed as follows:

$$
\begin{aligned}
PGF &= -\bar{\rho}\delta u\delta\left(\frac{1}{\rho}\frac{\partial p'}{\partial x}\right) - -\bar{\rho}\delta v\delta\left(\frac{1}{\rho}\frac{\partial p'}{\partial y}\right) \\
&\sim -\delta u\delta\left(\frac{\partial p'}{\partial x}\right) - \delta v\delta\left(\frac{\partial p'}{\partial y}\right) \\
&= -\delta\hat{\mathbf{u}}\bullet\delta(\nabla p') \\
&\sim -\delta\hat{\mathbf{u}}\bullet\delta\left(c_p\theta_v\bar{\rho}\nabla\pi'\right)
\end{aligned}
\qquad \text{C4)}
$$

where $\pi = (p/p_0)^{R_d/c_p}$ is the Exner pressure, $\pi' = \pi - \bar{\pi}$, $\theta_v = \theta(1+0.61q_v)$, and c_p is the specific heat of the dry air at constant pressure.

Using integration by part, we have

$$
\begin{aligned}
PGF &\sim -\delta\hat{\mathbf{u}}\bullet\delta\left(c_p\theta_v\bar{\rho}\nabla\pi'\right) \\
&\sim -c_p\theta_v\bar{\rho}\delta\hat{\mathbf{u}}\bullet\delta(\nabla\pi') \\
&= -c_p\theta_v\bar{\rho}\delta\hat{\mathbf{u}}\bullet\nabla(\delta\pi') \\
&= -c_p\theta_v\bar{\rho}(\nabla\bullet[(\delta\hat{\mathbf{u}})(\delta\pi')] - \delta\pi'\delta(\nabla\bullet\hat{\mathbf{u}})) \\
&= c_p\theta_v\bar{\rho}[\delta\pi'(\nabla\bullet\hat{\mathbf{u}})]
\end{aligned}
\qquad \text{C5)}
$$

Note the first term in the brackets becomes zero after integrating over the whole domain due to the idealized boundary conditions in our simulation.

Using the pseudo-incompressible Equation for moist air (A11 of Peng et.al 2014)

$$
\nabla\bullet\hat{\mathbf{u}} = \frac{H_m}{\bar{\theta}} - \frac{1}{\bar{\rho}\bar{\theta}}\frac{\partial\left(\bar{\rho}\bar{\theta}w\right)}{\partial z},
\qquad \text{C6)}
$$

We have

$$PGF \sim c_p \theta_\upsilon \overline{\rho} \left[\delta\pi' \delta(\nabla \bullet \hat{\mathbf{u}}) \right]$$

$$= c_p \theta_\upsilon \overline{\rho} \left[\delta\pi' \delta \left(\frac{H_m}{\overline{\theta}} - \frac{1}{\overline{\rho}\overline{\theta}} \frac{\partial(\overline{\rho}\overline{\theta}w)}{\partial z} \right) \right]$$

$$\sim c_p \overline{\rho} \delta\pi' \delta H_m - c_p \delta\pi' \frac{\partial(\overline{\rho}\overline{\theta}(\delta w))}{\partial z}$$

$$= c_p \overline{\rho} \delta\pi' \delta H_m - c_p \frac{\partial(\overline{\rho}\overline{\theta}(\delta w)(\delta\pi'))}{\partial z} + c_p \theta_\upsilon \overline{\rho}(\delta w) \frac{\partial(\delta\pi')}{\partial z}$$

C7)

     The first term represents the direct influence of the diabatic heating. This term is very small. The second term is the convergence of the difference vertical pressure flux, which corresponding to the gravity wave flux to the first order. Note if integrated over the entire domain then this term should be close to 0. The last term is the difference buoyancy flux, which represents the conversion of potential energy to horizontal kinetic energy; this is the dominant contribution term in this study.

     Since the pressure term does not have a cross-scale effect, as is shown in C. 1, the decomposition of pressure term for different scale is the same and will not be shown here.

Appendix D

Discrete Cosine Transform

All the spectrum and budget analysis in this article are calculated using discrete cosine transform (DCT) method defined as in Denis et al. (2002), which is more reliable than the widely used discrete Fourier transform (DFT) method. A brief introduction of this method is given as follows.

For a two-dimensional field *f(i, j)* of N_i by N_j grid points, the direct and inverse DCT are respectively defined as,

$$\{f(m,n)\} = \beta(m)\beta(n) \sum_{i=0}^{i=N_i-1} \sum_{j=0}^{j=N_j-1} f(i,j) \times cos\left[\frac{\pi m \left(i+\frac{1}{2}\right)}{N_i}\right] cos\left[\frac{\pi n \left(j+\frac{1}{2}\right)}{N_j}\right] \quad D1)$$

$$f(i,j) = \sum_{m=0}^{m=N_i-1} \sum_{n=0}^{n=N_j-1} \beta(m)\beta(n)\{f(m,n)\} \times cos\left[\frac{\pi m (i+\frac{1}{2})}{N_i}\right] cos\left[\frac{\pi n (j+\frac{1}{2})}{N_j}\right] \quad D2)$$

with

$$\beta(m) = \begin{cases} \sqrt{\frac{1}{N_i}}, & m=0 \\ \sqrt{\frac{2}{N_i}}, & m=1,2,3,..N_i-1 \end{cases} , \qquad \beta(n) = \begin{cases} \sqrt{\frac{1}{N_j}}, & n=0 \\ \sqrt{\frac{2}{N_j}}, & n=1,2,3,..N_j-1 \end{cases}$$

Let

$$\boldsymbol{e_{m,n}}(i,j) = \beta(m)\beta(n)cos\left[\frac{\pi m \left(i+\frac{1}{2}\right)}{N_i}\right] cos\left[\frac{\pi n \left(j+\frac{1}{2}\right)}{N_j}\right], \qquad D3)$$

it can be proven that $\boldsymbol{e_{m,n}}(i,j)$ is a set of orthogonal basis, which satisfies

$$\sum_{i=0}^{i=N_i-1} \sum_{j=0}^{j=N_j-1} \boldsymbol{e}_{m_1,n_1}(i,j) \cdot \boldsymbol{e}_{m_2,n_2}(i,j) = \begin{cases} 1, & m_1 = m_2 \text{ and } n_1 = n_2 \\ 0, & m_1 \neq m_2 \text{ or } n_1 \neq n_2 \end{cases} \qquad D4)$$

Utilizing equation A2 and A4), we have,

$$\sum_{i=0}^{i=N_i-1} \sum_{j=0}^{j=N_j-1} f(i,j) \cdot g(i,j)$$

$$= \sum_{i=0}^{i=N_i-1} \sum_{j=0}^{j=N_j-1} \left(\sum_{m=0}^{m=N_i-1} \sum_{n=0}^{n=N_j-1} \boldsymbol{e}_{m,n}(i,j)\{f(m,n)\} \right) \cdot \left(\sum_{m=0}^{m=N_i-1} \sum_{n=0}^{n=N_j-1} \boldsymbol{e}_{m,n}(i,j)\{g(m,n)\} \right)$$

$$= \sum_{m=0}^{m=N_i-1} \sum_{n=0}^{n=N_j-1} \{f(m,n)\} \cdot \{g(m,n)\}$$

$$= \sum_{k} \{f(\boldsymbol{k})\} \cdot \{g(\boldsymbol{k})\} \qquad D5)$$

Assume $g(i,j) = f(i,j)$, equation (D5) then implies that the total variance in the physical space equals the total variance in the spectral space. This serves as the foundation of equation (3) in the text. The energy spectrum can then be achieved by evaluating the variance of 2D fields as a function of different spatial scales. For a square domain, we associate each two-dimensional wavenumber pair $\boldsymbol{k}$(m, n) with a single-scale parameter k_h^2 , so that each element (m, n) on a given circle with the origin (m = 0, n = 0) has the same wavenumber. The one-dimensional wavenumber spectrum $E(k_h)$ is then obtained by taking the sum of the spectral variance over wavenumber bands $k_h - \frac{\Delta k}{2} < k_h \leq k_h + \frac{\Delta k}{2}$.

Also note here, the discrete cosine transform has no imaginary part, thus complex conjugate is not involved here, which is different with the discrete Fourier transform.

Appendix E

Decomposition of Advection and Pressure Term

The advection term is defined as,

$$A(k) = -\bar{\rho}\{\boldsymbol{u}\} \cdot \left\{\boldsymbol{u} \cdot \boldsymbol{\nabla}_h \boldsymbol{u} + w \frac{\partial \boldsymbol{u}}{\partial z}\right\}$$

$$= -\bar{\rho}\{\boldsymbol{u}\} \cdot \left\{\left(\boldsymbol{u} \cdot \boldsymbol{\nabla}_h \boldsymbol{u} + \frac{\boldsymbol{u}(\boldsymbol{\nabla}_h \cdot \boldsymbol{u})}{2} - \frac{\boldsymbol{u}(\boldsymbol{\nabla}_h \cdot \boldsymbol{u})}{2} + \frac{1}{2}\left(w\frac{\partial \boldsymbol{u}}{\partial z} + \frac{\partial(w\boldsymbol{u})}{\partial z} - \boldsymbol{u}\frac{\partial w}{\partial z}\right)\right)\right\} \qquad E1)$$

Rearranging all the terms in the bracket, we have

$$A(k) = -\bar{\rho}\{\boldsymbol{u}\} \cdot \left\{\boldsymbol{u} \cdot \boldsymbol{\nabla}_h \boldsymbol{u} + \frac{\boldsymbol{u}(\boldsymbol{\nabla}_h \cdot \boldsymbol{u})}{2}\right\} - \frac{1}{2}\bar{\rho}\{\boldsymbol{u}\} \cdot \left\{w\frac{\partial \boldsymbol{u}}{\partial z}\right\}$$

$$+ \frac{1}{2}\bar{\rho}\{\boldsymbol{u}\} \cdot \left\{\boldsymbol{u}(\boldsymbol{\nabla}_h \cdot \boldsymbol{u}) + \boldsymbol{u}\frac{\partial w}{\partial z}\right\}$$

$$- \frac{1}{2}\bar{\rho}\{\boldsymbol{u}\} \cdot \left\{\frac{\partial(w\boldsymbol{u})}{\partial z}\right\}$$

$$= -\bar{\rho}\{\boldsymbol{u}\} \cdot \left\{\boldsymbol{u} \cdot \boldsymbol{\nabla}_h \boldsymbol{u} + \frac{\boldsymbol{u}(\boldsymbol{\nabla}_h \cdot \boldsymbol{u})}{2}\right\} - \frac{1}{2}\bar{\rho}\{\boldsymbol{u}\} \cdot \left\{w\frac{\partial \boldsymbol{u}}{\partial z}\right\} \qquad E2)$$

$$+ \frac{1}{2}\bar{\rho}\{\boldsymbol{u}\} \cdot \left\{\boldsymbol{u}(\boldsymbol{\nabla}_h \cdot \boldsymbol{u}) + \boldsymbol{u}\frac{\partial w}{\partial z}\right\}$$

$$- \frac{1}{2}\frac{\partial(\bar{\rho}\{\boldsymbol{u}\} \cdot \{w\boldsymbol{u}\})}{\partial z} + \frac{1}{2}\bar{\rho}\left\{\frac{\partial \boldsymbol{u}}{\partial \boldsymbol{z}}\right\} \cdot \{w\boldsymbol{u}\} + \frac{1}{2}\frac{\partial\bar{\rho}}{\partial z}(\{\boldsymbol{u}\} \cdot \{w\boldsymbol{u}\})$$

Notice here $\frac{\partial\overline{\rho}}{\partial z}$ and $\bar{\rho}$ are both constant at each height level. Utilizing the continuity

equation under anelastic approximation,

$$(\boldsymbol{\nabla}_h \cdot \boldsymbol{u}) + \frac{\partial w}{\partial z} + \frac{w}{\bar{\rho}}\frac{\partial\bar{\rho}}{\partial z} = 0, \qquad E3)$$

and substituting E3) to the underline terms in E2), we can find that the sum of the two underline terms in E2) goes to zero. Thus, we have

$$A(k) = \underbrace{-\bar{\rho}\{u\} \cdot \left\{u \cdot \nabla_h u + \frac{u(\nabla_h \cdot u)}{2}\right\} - \frac{1}{2}\bar{\rho}\{u\} \cdot \left\{w\frac{\partial u}{\partial z}\right\} + \frac{1}{2}\bar{\rho}\left\{\frac{\partial u}{\partial z}\right\} \cdot \{wu\}}_{T(k)}$$

$$\underbrace{-\frac{1}{2}\frac{\partial(\bar{\rho}\{u\} \cdot \{wu\})}{\partial z}}_{divergence\ of\ vertical\ energy\ flux} \qquad\qquad E4)$$

Under double periodic boundary condition, the sum of T(k) term in (E4) over all the wavenumbers is zero. The proof is as follows. According to Equation (D5),

$$\sum_k T(k) = \sum_k \left[-\bar{\rho}\{u\} \cdot \left\{u \cdot \nabla_h u + \frac{u(\nabla_h \cdot u)}{2}\right\} - \frac{1}{2}\bar{\rho}\{u\} \cdot \left\{w\frac{\partial u}{\partial z}\right\} + \frac{1}{2}\bar{\rho}\left\{\frac{\partial u}{\partial z}\right\} \cdot \{wu\}\right]$$

$$= -\bar{\rho}\sum_{i,j}\left[u \cdot \left(u \cdot \nabla_h u + \frac{u(\nabla_h \cdot u)}{2}\right)\right] - \frac{1}{2}\bar{\rho}\sum_{i,j}\left[u \cdot \left(w\frac{\partial u}{\partial z}\right) - \frac{\partial u}{\partial z} \cdot (wu)\right]$$

$$= -\bar{\rho}\sum_{i,j}\left[u \cdot \left(u \cdot \nabla_h u + \frac{u(\nabla_h \cdot u)}{2}\right)\right]$$

$$= -\frac{\bar{\rho}}{L^2}\int_s \nabla \cdot \left(\frac{1}{2}u(u \cdot u)\right)ds = -\frac{\bar{\rho}}{L^2}\int_l \frac{1}{2}u(u \cdot u)u \cdot n\,dl \qquad\qquad E5)$$

where s represents the horizontal domain, l represents the lateral boundaries of s, and n denotes the unit vector pointing along the outward normal to l. A double periodic lateral boundary condition give a zero result to the integration along the boundary.

For the pressure term, it is easier to prove the decomposion in Equation (3-9) under the Fourier transform framework. Under Fourier transformation, the pressure term is written as:

$$P(k) = -\bar{\rho}\widetilde{u}^* \cdot \mathcal{F}\left(C_p\theta_v\nabla_h\pi'\right) + c.c$$

$\widetilde{u}$ and $\mathcal{F}(\mathbf{u})$ here represents the spectral coefficients of Fourier transform, * or c.c denotes complex conjugate.

$$P(k) = -\bar{\rho}\widetilde{u}^* \cdot \mathcal{F}\left(C_p\theta_v\nabla_h\pi'\right) + c.c$$

$$\sim - \bar{\rho} C_p \bar{\theta} \tilde{\boldsymbol{u}}^* \cdot \mathcal{F}(\boldsymbol{\nabla}_h \pi') + c.c$$

$$= -\bar{\rho} C_p \bar{\theta} \tilde{\boldsymbol{u}}^* \cdot \mathcal{F}(i\boldsymbol{k}\pi') + c.c$$

$$= \bar{\rho} C_p \bar{\theta} (\tilde{\boldsymbol{u}} \cdot i\boldsymbol{k})^* \tilde{\pi}' + c.c$$

$$= \bar{\rho} C_p \bar{\theta} (\mathcal{F}(\boldsymbol{\nabla}_h \cdot \boldsymbol{u}))^* \tilde{\pi}' + c.c \qquad\qquad E6)$$

Using the improved anelastic approximation (simply using E3 will give similar results, we use this improved anelastic approximation to be as accurate as we can), Equation 7 of Durran (1989),

$$\boldsymbol{\nabla}_h \cdot \boldsymbol{u} + \frac{1}{\bar{\rho}\bar{\theta}} \frac{\partial}{\partial z} (\bar{\rho}\bar{\theta}w) = \frac{H}{C_p \bar{\rho}\bar{\theta}\bar{\pi}}, \qquad E7)$$

we have

$$P(k) \sim \bar{\rho} C_p \bar{\theta} \left(\frac{H}{C_p \bar{\rho}\bar{\theta}\bar{\pi}} - \frac{1}{\bar{\rho}\bar{\theta}} \frac{\partial}{\partial z} (\bar{\rho}\bar{\theta}w) \right)^* \tilde{\pi}' + c.c$$

$$= \frac{\tilde{H}^* \tilde{\pi}'}{\bar{\pi}} - C_p \frac{\partial}{\partial z} (\bar{\rho}\bar{\theta}\tilde{w}^* \tilde{\pi}') + C_p \bar{\rho}\bar{\theta}\tilde{w}^* \frac{\partial \tilde{\pi}'}{\partial z} + c.c$$

$$\sim \underbrace{C_p \frac{\partial}{\partial z} (\bar{\rho}\bar{\theta}\{w\} \cdot \{\pi'\})}_{\text{divergence of vertical energy fluxes}} + \underbrace{C_p \bar{\rho}\bar{\theta}\{w\} \cdot \left\{ \frac{\partial \pi'}{\partial z} \right\}}_{B(k)}, \qquad E8)$$

When using the discrete cosine transform method, the complex conjugate will disappear. We also neglect the direct diabatic heating term when showing the results, since it is several orders of magnitude smaller than the other two terms.

Bibliography

Balsamo, G., Viterbo, P., Beljaars, A., van den Hurk, B., Hirschi, M., Betts, A. K. and Scipal, K. (2009). A revised hydrology for the ECMWF model: Verification from field site to terrestrial water storage and impact in the Integrated Forecast System. J. Hydrometeorol., 10, 623–643.

Balsamo, G., Pappenberger, F., Dutra, E., Viterbo, P. and van den Hurk, B. (2011). A revised land hydrology in the ecmwf model: a step towards daily water flux prediction in a fully-closed water cycle. Hydrological Processes, 25(7), 1046–1054, doi:10.1002/hyp.7808.

Bauer, P., A. Thorpe, and G. Brunet, 2015: The quiet revolution of numerical weather prediction. *Nature*, **525**, 47–55

Bei, N., and F. Zhang, 2007: Impacts of Initial Condition Errors on Mesoscale Predictability of Heavy Precipitation along the Mei-Yu Front of China. *Quart J. R. Meteo. Soc.*, **133**, 83-99.

Bei, N., and F. Zhang, 2014: Mesoscale Predictability of Moist Baroclinic Waves: Variable and Scale Dependent Error Growth. *Adv. Atmos. Sci.*, 995-1008.

Beljaars, A. C. M., Brown, A. R. and Wood, N. (2004). A new parametrization of turbulent orographic form drag. Q. J. R. Meteorol. Soc., 130, 1327–1347.

Bierdel, L., C. Snyder, S.-H. Park and W. C. Skamarock, 2016: Accuracy of rotational and divergent kinetic energy spectra diagnosed from flight-track winds. *J. Atmos. Sci.*, **73** (8), 3273–3286.

Bretherton, C. S., and M. F. Khairoutdinov, 2015: Convective self-aggregation feedbacks in near-global cloud-resolving simulations of an aquaplanet. *J. Adv. Model. Earth Syst.*, **7**, 1765–1787.

Callies, J, R. Ferrari, and O. Buhler, 2014: Transition from geostrophic turbulence to inertia–gravity waves in the atmospheric energy spectrum. *Proc. Natl. Acad. Sci.*, **111**, 17033-17038.

Chang, E.K.M., and I. Orlanski, 1993: On the Dynamics of a Storm Track. *J. Atmos. Sci.*, **50**, 999-1015.

Chang, E. K. M., S. Lee, and K. L. Swanson, 2002: Storm track dynamics. *J. Climate*, **15**, 2163–2183.

Charney, G. J. (1948), On the scale of atmospheric motions, *Geofysiske Publikasjoners*, **17**(2), 1–17.

Charney, J. G., 1971: Geostrophic turbulence. *J. Atmos. Sci.*, **28,** 1087–1095.

Chen, L., B. K. Tan, N. G. Kvamstø, and O. M. Johannessen, 2014: Wintertime cyclone/anticyclone activity over China and its relation to upper tropospheric jets. *Tellus* A, **66**, 21889

Cho, J. Y. N., R. E. Newell, and J. D. Barrick, 1999: Horizontal wavenumber spectra of winds, temperature, and trace gases during the Pacific Exploratory Missions: 2. Gravity waves, quasi-two-dimensional turbulence, and vortical modes. *J. Geophys. Res.*, **104**, 16297–16308.

Davis, C. A., and K. A. Emanuel, 1991: Potential vorticity diagnosis of cyclogenesis. *Mon. Wea. Rev.*, **119**, 1929–1952.

Davis, C. A., and M. L. Weisman, 1994: Balanced dynamics of mesoscale vortices produced in simulated convective systems. *J. Atmos. Sci.,***51,**2005–2030.

Denis, B., J. Côté, and R. Laprise, 2002: Spectral decomposition of two-dimensional atmospheric fields on limited-area domains using the Discrete Cosine Transform (DCT). *Mon. Wea. Rev*, **130**, 1812–1829.

Durran, D. R., 1989: Improving the Anelastic Approximation. *J. Atmos. Sci.*, 46, 1453–1461.

Durran, D., and Mark Gingrich, 2014: Atmospheric Predictability: Why Butterflies Are Not of Practical Importance. *J. Atmos. Sci.*, **71**, 2476–2488.doi: http://dx.doi.org/10.1175/JAS-D-14-0007.1

Durran, D. R. and J. A. Weyn, 2016: Thunderstorms don't get butterflies. *Bull. Amer. Meteor. Soc.*, **97**, 237-243.

Durran, D. R., P. A. Reinecke, and J. D. Doyle, 2013: Large-scale errors and mesoscale predictability in Pacific Northwest snowstorms. *J. Atmos. Sci.*, **70**, 1470–1487

Hamilton, K., Y. O. Takahashi, and W. Ohfuchi, 2008: The mesoscale spectrum of atmospheric motions investigated in a very fine resolution global general circulation model. *J. Geophys. Res.*, **113**, D18110.

Hohenegger, C., and C. Schär (2007), Predictability and error growth dynamics in cloud resolving models, *J. Atmos. Sci.*, **64**, 4467-4478, doi:10.1175/2007JAS2143.1.

Hong, S.-Y., and H.-L. Pan, 1996: Nonlocal boundary layer vertical diffusion in a Medium-Range Forecast Model. *Mon. Wea. Rev.*, **124**, 2322–2339.

Iacono, M., Delamere, J., Mlawer, E., Shephard, M., Clough, S. and Collins, W. (2008). Radiative forcing by long-lived greenhouse gases: Calculations with the AER radiative transfer models. J. *Geophys. Res.*, **113D**, 13103.

Isaksen, L. M. B., R. Buizza, M. F., Haseler, J., Leutbecher, M. and Raynaud, L. (2010). Ensemble of data assimilations at ECMWF. *Technical Report 636*, ECMWF, Reading, UK.

Klemp, J. B., J. Dudhia, and A. D. Hassiotis, 2008: An Upper Gravity-Wave Absorbing Layer for NWP Applications. *Mon. Wea. Rev.*, **136**, 3987–4004.

Koshyk, J. N., K. Hamilton, and J. D. Mahlman, 1999: Simulation of k−5/3 mesoscale spectral regime in the GFDL SKYHI general circulation model. *Geophys. Res. Lett.,* **26**, 843–846.

Köhler, M., Ahlgrimm, M. and Beljaars, A. (2011). Unified treatment of dry convective and stratocumulus-topped boundary layers in the ECMWF model. Q. J. R. Meteorol. Soc., 137, 43–57.

Lamberson, W. S., R. D. Torn, L. F. Bosart, and L. Magnusson, 2016: Diagnosis of the source and evolution of medium-range forecast errors for extratropical cyclone Joachim, *Wea. Forecast.*, **31**, 1197–1214.

Langland, R. H., M. A. Shapiro, and R. Gelaro, 2002: Initial condition sensitivity and error growth in forecasts of the 25 January 2000 East Coast snowstorm. *Mon. Wea. Rev.*, **130**, 957–974.

Lillo SP, Parsons DB. 2016. Investigating the dynamics of error growth in ecmwf medium range forecast busts. *Quarterly Journal of the Royal Meteorological Society:* n/a–n/adoi:10.1002/qj.2938.

Lilly, D. K., 1983: Stratified turbulence and the mesoscale variability of the atmosphere. *J. Atmos. Sci.*, **40**, 749–761.

Lin, Y.-L., R. D. Farley, and H. D. Orville, 1983: Bulk parameterization of the snow field in a cloud model. *J. Climate Appl. Meteor.*, **22**, 1065–1092.

Lindborg, E., 2006: The energy cascade in a strongly stratified fluid. *J. Fluid Mech.*, **550**, 207–242.

Lindborg, E., 2015: A Helmholtz decomposition of structure functions and spectra calculated from aircraft data. *J. Fluid Mech.*, **762**, R4, doi:10.1017/jfm.2014.685.

Lorenz, E. N., 1963: Deterministic nonperiodic flow. *J. Atmos. Sci.*, **20**, 130–141, doi:https://doi.org/10.1175/1520-0469(1963)020<0130:DNF>2.0.CO;2.

Lorenz, E. N., 1969: Atmospheric predictability as revealed by naturally occurring analogues. *J. Atmos. Sci.*, **26**, 636–646.

Lorenz, E. N., 1982: Atmospheric predictability experiments with a large numerical model. *Tellus, 34,* 505-513.

Lorenz, E. N., 1996: Predictability—A problem partly solved. *Proc. Seminar on Predictability,* Reading, United Kingdom, ECMWF, 1–18.

Magnusson, L. 2017: Diagnostic methods for understanding the origin of forecast errors. Q.J.R. Meteorol. Soc. *Accepted Author Manuscript.* doi:10.1002/qj.3072

Majumdar, S. J., 2016: A review of targeted observations. *Bull. Amer. Meteor. Soc.*, **97**, 2287–2303.

Mapes, B.E., S. Tulich, T. Nasuno, and M. Satoh, 2008: Predictability aspects of global aqua-planet simulations with explicit convection. *J. Meteor. Soc. Japan*, **86**A, 175-185.

Markowski, P. and Richardson, Y. (2010). *Mesoscale Meteorology in Midlatitudes*. John Wiley & Sons, Ltd.

Melhauser, C, and F, Zhang, 2012: Practical and Intrinsic Predictability of Severe and Convective Weather at the Mesoscales. *J. Atmos. Sci.*, **69**, 3350–3371.

Mlawer, E. J., Taubman, S. J., Brown, P. D., Iacono, M. J. and Clough, S. A. (1997). Radiative transfer for inhomogeneous atmospheres: RRTM, a validated correlated-k model for the longwave. *J. Geophys. Res.*, **102D**, 16663–16682.

Morrison, H., G. Thompson, and V. Tatarskii, 2009: Impact of cloud microphysics on the development of trailing stratiform precipitation in a simulated squall line: Comparison of one- and two-moment schemes. *Mon. Wea. Rev*., **137**, 991–1007.

Morss, R. E., C. Snyder, and R. Rotunno, 2009: Spectra, spatial scales, and predictability in a quasigeostrophic model. *J. Atmos. Sci.*, **66**, 3115–3130.

Munsell, E. B., and F. Zhang, 2014: Prediction and uncertainty of Hurricane Sandy (2012) explored through a real-time cloud-permitting ensemble analysis and forecast system. *J. Adv. Model. Earth Sci*., **6**, 1–20.

Nastrom, G. D., and K. S. Gage, 1985: A climatology of atmospheric wavenumber spectra of wind and temperature observed by commercial aircraft. *J. Atmos. Sci.*, **42**, 950–960.

Orr, A., Bechtold, P., Scinocca, J. F., Ern, M. and Janiskova, M. (2010). Improved middle atnosphere climate and forecasts in the ECMWF model through a non-orographic gravity wave drag parametrization. J. Climate, 23, 5905–5926.

Palmer, T. N., A. Döring, and G. Seregin, 2014: The real butterfly effect. *Nonlinearity*, **27** (2014), R123-R141. doi:10.1088/0951-7715/27/9/R123.

Palmer, T. (2017), The primacy of doubt: Evolution of numerical weather prediction from determinism to probability, *J. Adv. Model. Earth Syst.*, **9**, doi:10.1002/2017MS000999.

Peng, J., L. Zhang, Y. Luo, and Y. Zhang, 2014: Mesoscale energy spectra of the mei-yu front system. Part I: Kinetic energy spectra. *J. Atmos. Sci.*, **71**, 37–55, doi:10.1175/JAS-D-13-085.1.

Plougonven, R., and Chris Snyder, 2007: Inertia–Gravity Waves Spontaneously Generated by Jets and Fronts. Part I: Different Baroclinic Life Cycles. *J. Atmos. Sci.*, **64**, 2502–2520.

Rodwell, M. J., et al. (2013), Characteristics of occasional poor medium-range weather forecasts for Europe, *Bull. Am. Meteorol. Soc*., **94**, 1393–1405, doi:10.1175/BAMS-D-12-00099.1.

Rotunno, R, and C. Snyder, 2008: A Generalization of Lorenz's Model for the Predictability of Flows with Many Scales of Motion. *J. Atmos. Sci.*, **65**, 1063–1076.

Selz, T and G. C. Craig, 2015a: Upscale Error Growth in a High-Resolution Simulation of a Summertime Weather Event over Europe. *Mon. Wea. Rev*., **143**, 813–827.

Selz, T., and G. C. Craig, 2015b: Simulation of upscale error growth with a stochastic convection scheme, *Geophys. Res. Lett*., **42**, doi:10.1002/2015GL063525.

Simmons, A. J., and B. J. Hoskins, 1978: The life cycles of some nonlinear baroclinic waves. *J. Atmos. Sci.*, **35**, 414–432.

Skamarock, W. C., M. L. Weisman and J. B. Klemp, 1994: Three-Dimensional evolution of simulated long-lived squall lines. *J. Atmos. Sci*., **51**, 2563-2584.

Skamarock, W. C., 2004: Evaluating mesoscale NWP models using kinetic energy spectra. *Mon. Wea. Rev.*, **132**, 3019–3032.

Stensrud, D. J., 1996: Effects of persistent, midlatitude mesoscale regions of convection on the large-scale environment during the warm season. *J. Atmos. Sci.*, **53,** 3503–3527.

Skamarock, W. C., and Coauthors, 2008: A description of the Advanced Research WRF version 3. NCAR Tech. Note NCAR/TN–475+STR, 113 pp.

Skamarock, W. C., S.-H. Park, J. B. Klemp, and C. Snyder, 2014: Atmospheric kinetic energy spectra from global high-resolution nonhydrostatic simulations. *J. Atmos. Sci.*, **71**, 4369-4381.

Sun, Y., and F. Zhang, 2016: Intrinsic versus practical limits of atmospheric predictability and the significance of the butterfly effect. *J. Atmos. Sci.*, **73**, 1419-1438.

Sun, Y. Q., R. Rotunno, and F. Zhang, 2017: Contributions of moist convection and internal gravity waves to building the atmospheric −5/3 kinetic energy spectra. *J. Atmos. Sci.*, **74**, 185–201,

Tan, Z., F. Zhang, R. Rotunno, and C. Snyder, 2004: Mesoscale predictability of moist baroclinic waves: Experiments with parameterized convection. *J. Atmos. Sci.*, **61**, 1794–1804; Corrigendum, 65, 1479.

Tao, D., and F. Zhang (2014), Effect of environmental shear, sea-surface temperature, and ambient moisture on the formation and predictability of tropical cyclones: An ensemble-mean perspective. *J. Adv. Model. Earth Syst.*, **6**, 384–404.

Tao, D., and F. Zhang, 2015: Effects of Vertical Wind Shear on the Predictability of Tropical Cyclones: Practical versus Intrinsic Limit. *J. Adv. Model. Earth Syst.*, **7,** 1534-1553.

Taraphdar, S., P. Mukhopadhyay, R. L. Lueng, F. Zhang, S. Abhilash, and B. N. Goswami, 2014: The Role of Moist Processes in the Intrinsic Predictability of Indian Ocean Cyclones. *J. Geophys. Res. Atmos.*, **119**, 8032–8048

Thorncroft, C. D., Hoskins, B. J. and McIntyre, M. E. (1993), Two paradigms of baroclinic-wave life-cycle behaviour. *Q.J.R. Meteorol. Soc.*, **119**: 17–55.

Tiedtke, M. (1989). A comprehensive mass flux scheme for cumulus parameterization in large-scale models. Mon. Wea. Rev., 117, 1779–1800.

Tiedtke, M. (1993), Representation of clouds in large-scale models, *Mon. Weather Rev.,* **121**, 3040–3061.

Tribbia, J., and D. Baumhefner, 2004: Scale interactions and atmospheric predictability: An updated perspective. *Mon. Wea. Rev.*, **132**, 703–713.

Tulloch, R., and K. S. Smith, 2006: A theory for the atmospheric energy spectrum: Depth-limited temperature anomalies at the tropopause. *Proc. Natl. Acad. Sci.* USA, **103**, 14690–14694.

Vallis, GK, 2006: *Atmospheric and Oceanic Fluid Dynamics* (Cambridge Univ Press, Cambridge, UK).

VanZandt, T. E., 1982: A universal spectrum of buoyancy waves in the atmosphere. *Geophys. Res. Lett.*, **9**, 575–578.

Waite, M. L., and C. Snyder, 2009: The mesoscale kinetic energy spectrum of a baroclinic life cycle. *J. Atmos. Sci. ,* **66***,* 883–901.

Waite, M. L., and Chris Snyder, 2013: Mesoscale Energy Spectra of Moist Baroclinic Waves. *J. Atmos. Sci.*, **70**, 1242–1256.

Wei, J., and F. Zhang, 2014: Mesoscale gravity waves in moist baroclinic jet-front systems. *J. Atmos. Sci.*, **71**, 929~952. doi: http://dx.doi.org/10.1175/JAS-D-13-0171.1

Wei, J. and F. Zhang, 2015: Tracking gravity waves in moist baroclinic waves. *J. Adv. in Modeling Earth Systems*, **7**, 67-91.

Wei, J., F. Zhang, and J. H. Richter, 2016: Toward improving nonorographic gravity wave parameterizations: An analysis of gravity wave spectral characteristics in moist baroclinic jet-front systems. *J. Atmos. Sci.*, **73**, 3133–3155.

Weisman, M. L. and J. B. Klemp. 1982. The dependence of numerically simulated convective storms on vertical wind shear and buoyancy. *Mon. Wea. Rev*. **110**, 504–520.

Yuter, S. E., and R. A. Houze, 1995: Three-dimensional kinematic and microphysical evolution of Florida cumulonimbus. Part II: Frequency distributions of vertical velocity, reflectivity, and differential reflectivity. *Mon. Wea. Rev.*, **123**, 1941–1963

Zhang, F., C. Snyder, and R. Rotunno, 2002: Mesoscale predictability of the "surprise" snowstorm of 24-25 January 2000. *Mon. Wea. Rev.*, **130**, 1617-1632

Zhang, F., C. Snyder, and R. Rotunno, 2003: Effects of moist convection on mesoscale predictability. *J. Atmos. Sci,*, **60**, 1173-1185.

Zhang, F., 2004: Generation of Mesoscale Gravity Waves in Upper-Tropospheric Jet–Front Systems. *J. Atmos. Sci.,* **61**, 440–457.

Zhang, F., A. M. Odins, and J. W. Nielsen-Gammon, 2006: Mesoscale predictability of an extreme warm-season precipitation event. *Wea. Forecasting*, **21**, 149-166.

Zhang, F., N. Bei, R. Rotunno, C. Snyder, and C. C. Epifanio, 2007: Mesoscale Predictability of Moist Baroclinic Waves: Convection-Permitting Experiments and Multistage Error Growth Dynamics. *J. Atmos. Sci.*, **64**, 3579–3594.

Zhang, F., and J. A. Sippel, 2009: Effects of moist convection on hurricane predictability. *J. Atmos. Sci.*, **66**, 1944-1961.

Zhang, F., and D. Tao, 2013: Effects of vertical wind shear on the predictability of tropical cyclones. *J. Atmos. Sci.*, **70**, 975–983.

Zhang, Y. J., F. Zhang, Z. Meng, D. J. Stensrud 2015: Predictability of the 20 May 2013 Tornadic Thunderstorm Event in Oklahoma: Sensitivity to Synoptic Timing and Topographical Forcing. *Mon. Wea. Rev.,* **143,** 2973-2997.

Zhang, Y. J., F. Zhang, Z. Meng, D. J. Stensrud 2016: Intrinsic Predictability of the 20 May 2013 Tornadic Thunderstorm Event in Oklahoma at Storm Scales. *Mon. Wea. Rev.,* **144***,* 1273-1298.

Zhu, H, A. J. Thorpe. 2006. Predictability of extra-tropical cyclones: the influence of initial condition and model uncertainties. *J. Atmos. Sci.* **61**,1483 – 1497.

VITA

Y. Qiang Sun

Department of Meteorology, The Pennsylvania State University
624 Walker Building, University Park, PA, 16802
Email: yus140@psu.edu Phone: 814-777-2667

EDUCATION

M.S.   in Meteorology,   Peking University, 2012
B. S.   in Atmospheric Science,   Peking University, 2009

RESEARCH AND TEACHING EXPERIENCE

2012-present: Research Assistant**,** Department of Meteorology, Pennsylvania State University
2015/05-08   Visiting Graduate Research Assistant, National Center for Atmospheric Research
2012, 2016   Teaching Assistant, Department of Meteorology, Pennsylvania State University
2009-2012   Teaching Assistant, Peking University

SELECTED PUBLICATIONS

Sun Y. Qiang, F. Zhang, 2017: *Error growth dynamics and predictability of mid-latitude weather systems revealed from an extremely high-resolution global ensemble*. In preparation.

Sun, Y. Qiang, R. Rotunno, and F. Zhang, 2017: Contributions of moist convection and internal gravity waves to building the atmospheric "-5/3" kinetic energy spectra, *Journal of the Atmospheric Sciences*, **74**, 185-201

Sun, Y. Qiang, and F. Zhang, 2016: Intrinsic versus practical limits of atmospheric predictability and the significance of the butterfly effect. *Journal of the Atmospheric Sciences,* **73**, 1419-1438

Sun, Y. **Qiang**, Y. Jiang, B. Tan and F. Zhang, 2013: The Governing Dynamics of the Secondary Eyewall Formation of Typhoon Sinlaku (2008). *Journal of the Atmospheric Sciences*, **70**, 3818-3837.